Supersonic Axial & Radial Rotor Design for ORC applications

Using Method of Characteristics

Pulkit Aggarwal

Technische Universiteit Delft

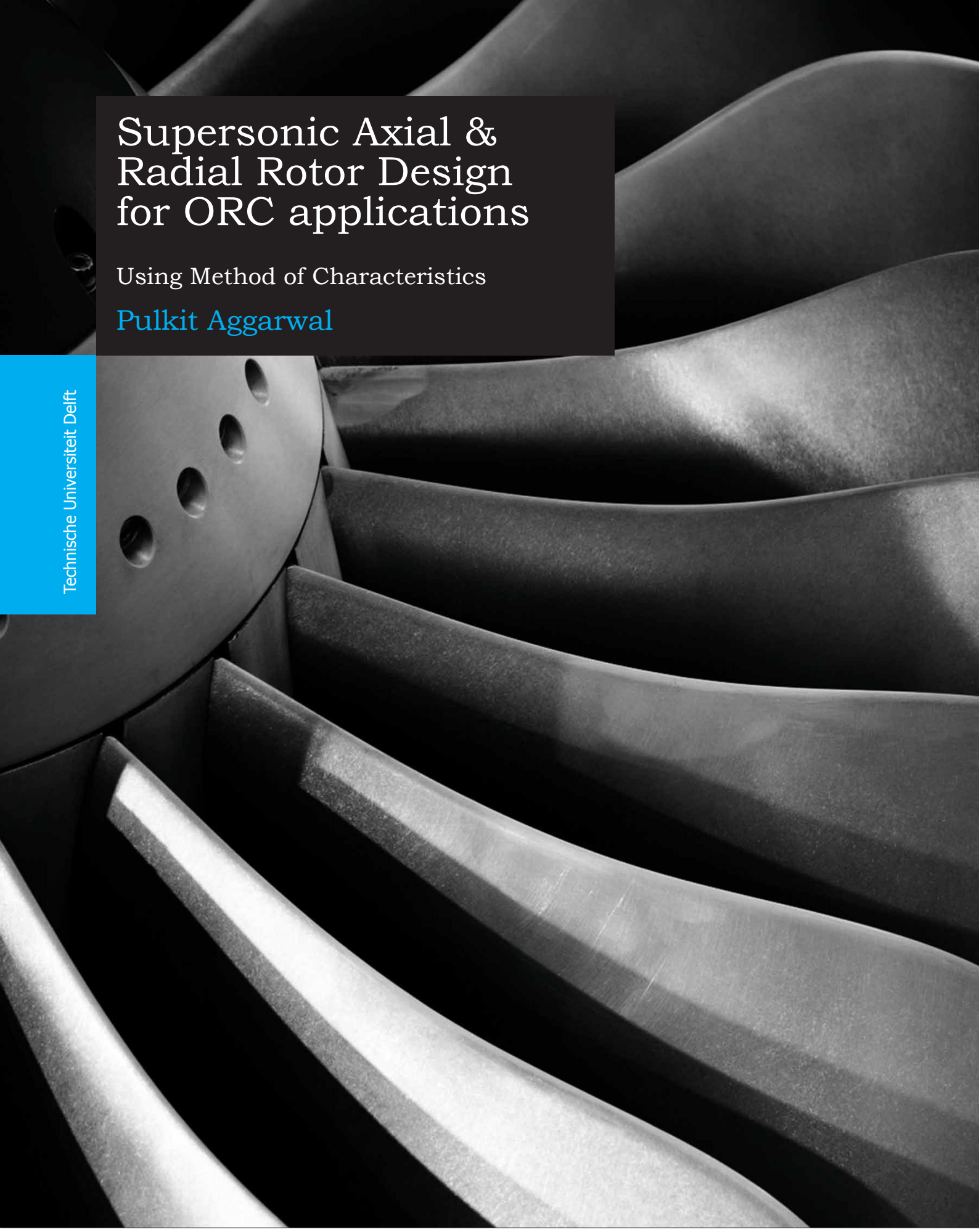

TU Delft Delft University of Technology

Challenge the future

Supersonic Axial & Radial Rotor Design for ORC applications

Using Method of Characteristics

by

Pulkit Aggarwal

in partial fulfillment of the requirements for the degree of

Master of Science
in Mechanical Engineering

at the Delft University of Technology,
to be defended publicly on Friday November 30, 2018 at 02:30 PM.

Supervisor:	Prof. dr. ir. Rene Pecnik,	TU Delft
	Ir. Gustavo J. Otero,	TU Delft
	Ir. Nitish Anand,	TU Delft
Thesis committee:	Prof. dr. ir. Sikke Klein,	TU Delft
	Dr. ir. Matteo Pini,	TU Delft

TU Delft Delft University of Technology

Abstract

The growing environmental concerns has put a lot of political & ethical pressure on the conventional industrial practices. The research community is ever so eager to investigate new technologies that can offer an efficient and environmentally sound solution to the issues sparked by the polluting industrial processes. One of the potential solution is an Organic Rankine Cycle (ORC) which is proven to be an effective technology to efficiently extract energy from low-temperature sources. The ORC is basically a Rankine cycle but employs a high molecular weight organic fluid as the energy carrier. The peculiar non-classical gas dynamics behaviour of these fluids during dry expansion close to the vapour saturation line (in the dense gas region) poses certain challenges on the turbine design. Furthermore, the low speed of sound in organic fluids and high expansion ratio required in an ORC turbine leads to highly supersonic flows in the turbine. Such high speed flows within a turbine stage are susceptible to high shock losses, if necessary corrective steps are not taken during early design phase.

This has sparked a wave of interest in the scientific community to come up with an efficient supersonic ORC turbine design guidelines. The design of a supersonic turbine rotor is crucial to ensure efficient performance of the turbine. In the mid-20^{th} century, a supersonic impulse rotor design methodology for axial turbines was proposed that boasts shock-free turning of supersonic flows using the vortex-flow theory. This procedure relies on Method of Characteristics (MOC) to solve hyperbolic governing PDEs. The method got enriched later with the capability to account for dense gas effects on the rotor geometry which is essential for ORC applications.

However, there are no such design guidelines available in the literature to generate a radial rotor blade especially for supersonic flows. The conventional 1D preliminary design methods, generally available for radial rotor blades, are not very reliable in supersonic flow regime. This calls for a novel design philosophy for supersonic radial rotors that accounts for supersonic flow phenomenon early in the design phase to ensure efficient turbine performance. The objective of this thesis is to put forth a design methodology for supersonic radial rotors that acknowledges the flow equations in the design procedure. The proposed design ideology is to extend the supersonic axial rotor design procedure by including the fictitious forces' effects in the governing equations to generate a radial rotor using MOC. These pseudo forces (Centrifugal & Coriolis) are experienced by the flow in the radial runner if seen from the rotor's rotating frame of reference. Furthermore, the dense gas effects are also included in the design using the properties from CoolProp library. A design tool is developed in PYTHON that implements the aforementioned ideology in the design procedure.

This thesis takes the first step towards developing a fully functional design methodology for supersonic radial rotors. Therefore, a simple case of a constant force's influence on the rotor geometry is studied in this work and compared with the CFD simulations in both perfect & dense gas region. Future research will focus on understanding the complex behaviour of organic fluids in the presence of an external force and modify the design procedure accordingly.

Contents

List of Figures

List of Tables

Acknowledgements

First and foremost, I would like to express my heartfelt gratitude to my parents who made it possible for me to realize my dreams. Their unshaken support has been nothing less than a blessing for me throughout my time away from home.

I am extremely grateful to my supervisor, Dr. ir. Rene Pecnik for giving me the opportunity to pursue this research topic. His constructive feedback kept me on the right track throughout my thesis period. Our discussions taught me how to think critically and pose fundamental questions to get a deeper understanding.

This thesis would not have its current shape and depth without the immense support and encouragement from my daily supervisor, Ir. Gustavo J. Otero. I would like to express my honest gratitude to him for his patience to guide me all the way through this project. His insights helped me tremendously to develop the algorithms. Working with him, has taught me how to become a better researcher.

I would also like to thank Ir. Nitish Anand for sharing his knowledge and devoting his time on the subject. His valuable inputs helped me push the boundaries of this research.

I also express my gratitude to Ir. Stephan Smit for always being there to have crucial discussions and ask the right questions. It allowed me to approach the problem from a better perspective.

Last but certainly not the least, a cheerful shout-out to my friends who made my time here in the Netherlands memorable. I am extremely thankful for their motivation in the time of need and helping me push through the hard times.

Pulkit Aggarwal
Delft University of Technology,
November 2018

Nomenclature

$(X^*_{lo} - Y^*_{lo})$ Non-dimensional coordinate system for lower transition arc normalized with r^* $[-]$

$(x^*_{lo} - y^*_{lo})$ Non-dimensional coordinates of lower transition arc $[-]$

$(X^*_{up} - Y^*_{up})$ Non-dimensional coordinate system for upper transition arc normalized with r^* $[-]$

$(x^*_{up} - y^*_{up})$ Non-dimensional coordinates of upper transition arc $[-]$

$\alpha_{lo,in}$ Flow turning induced in the lower/pressure side circular arc at the blade's inlet $[deg]$

$\alpha_{lo,out}$ Flow turning induced in the lower/pressure side circular arc at the blade's outlet $[deg]$

$\alpha_{up,in}$ Flow turning induced in the upper/suction side circular arc at the blade's inlet $[deg]$

$\alpha_{up,out}$ Flow turning induced in the upper/suction side circular arc at the blade's outlet $[deg]$

$\bar{m}_{k,in}$ Slope of k^{th} segment of lower transition arc at blade's inlet $[-]$

β_{in} Inlet relative flow angle $[deg]$

β_{out} Outlet relative flow angle $[deg]$

$\dot{m}$ Mass flow rate $[kg/s]$

Γ Fundamental derivative of gas dynamics $[-]$

γ Specific heat capacity ratio $[-]$

λ Slope of characteristic line $[-]$

$_{k,in}$ Slope of Mach lines at k^{th} segment of lower transition arc at blade's inlet $[-]$

$\mathbf{F_B}$ Body force per unit mass vector $[m/s^2]$

$\mathbf{F_{Bx}}, \mathbf{F_{By}}, \mathbf{F_{Bz}}$ Body force per unit mass components in x, y & z direction $[m/s^2]$

$\mathcal{X}^*_{lo}, \mathcal{Y}^*_{lo}$ Non-dimensional coordinates of lower transition arc in $(X^* - Y^*)$ coordinate system $[-]$

$\mu_{k,in}$ Mach angle at k^{th} segment of lower transition arc at blade's inlet $[deg]$

∇ Nabla operator $[-]$

ν Prandtl-Meyer angle $[deg]$

ν_{in} Prandtl-Meyer angle at the blade's inlet $[deg]$

ν_{lo} Prandtl-Meyer angle at the lower arc/pressure side $[deg]$

ν_{out} Prandtl-Meyer angle at the blade's outlet $[deg]$

ν_{up} Prandtl-Meyer angle at the upper arc/suction side $[deg]$

ω Vorticity $[m/s]$

Φ Velocity potential function $[-]$

Φ_x, Φ_y Partial derivative of the potential function with respect to x & y $[-]$

$\phi_{k,in}$ Flow angle at k^{th} segment of lower transition arc at blade's inlet $[deg]$

Φ_{xx}, Φ_{yy} Double partial derivative of the potential function with respect to x & y $[-]$

ρ fluid density $[kg/m^3]$

τ Compressibility $[Pa^{-1}]$

$\vec{V}$ Velocity vector $[m/s]$

ξ Specific volume $[m^3/kg]$

a Speed of sound $[m/s]$

A_{in} Blade inlet flow passage area $[m^2]$

A_{out} Blade outlet flow passage area $[m^2]$

ch^* Non-dimensional blade chord, normalized with r^* $[-]$

CR Blade contraction ratio $[-]$

$F_{c,i}$ Centrifugal forces per unit mass at the inner radius of rotor $[m/s^2]$

$F_{c,o}$ Centrifugal forces per unit mass at the outer radius of rotor $[m/s^2]$

G Blade pitch $[m]$

H Blade height $[m]$

j Number of straight line segments along upper transition arc $[-]$

k Number of straight line segments along lower transition arc $[-]$

M Mach number $[-]$

M^* Critical velocity ratio $[-]$

M_{in}^* Critical velocity ratio at the blade's inlet $[-]$

M_{lo}^* Critical velocity ratio at the lower arc/pressure side $[-]$

M_{out}^* Critical velocity ratio at the blade's outlet $[-]$

M_{up}^* Critical velocity ratio at the upper arc/suction side $[-]$

M_{in} Inlet relative Mach number $[-]$

M_{out} Outlet relative Mach number $[-]$

N Rotational speed $[RPM]$

P Static Pressure $[Pa]$

P_o Total pressure $[Pa]$

$P_{o,r}$ Reduced total pressure $[-]$

R Gas constant $[J/kg.K]$

R Radius of curvature of a streamline $[m]$

R^* Dimensionless radius of curvature of a streamline $[-]$

r^* Radius of curvature of a sonic velocity streamline $[m]$

R_{lo}^* Non-dimensional radius of curvature for lower transition arc normalized with r^* $[-]$

R_{up}^* Non-dimensional radius of curvature for upper transition arc normalized with r^* $[-]$

s Specific entropy $[J/kg.K]$

T Static Temperature $[K]$

t Time $[s]$

T_o Total temperature $[Pa]$

$T_{o,r}$ Reduced total temperature $[-]$

u, v, w Velocity components in x, y & z direction $[m/s]$

u_x, u_y Partial derivatives of u & v with respect to x & y $[m/s]$

V Velocity magnitude $[m/s]$

$x^*_{j,in}, y^*_{j,in}$ Non-dimensional coordinates of j^{th} segment of major-compression characteristic at blade's inlet $[-]$

$x^*_{k,in}, y^*_{k,in}$ Non-dimensional coordinates of k^{th} segment of major-expansion characteristic at blade's inlet $[-]$

Z Compressibility factor $[-]$

1

Introduction

A succinct introduction of Organic Rankine Cycles and the importance of a fluid expansion device in the cycle is established. The unique behaviour of the organic fluids during expansion is discussed. A brief motivation of the current work is presented and a thesis outline concludes this chapter.

1.1. Organic Rankine Cycle

The Organic Rankine Cycle (ORC) has garnered a lot of attention from the scientific community in recent years. Due to its great potential to assist in improving the overall process efficiency in various industries, while keeping in check the worldwide goal of curbing industrial emissions heating up our planet. The unique capability of ORC to extract thermal energy from low-grade heat sources is the reason behind its popularity in the field. The most promising applications of this technology are waste heat recovery from primary engines or industrial processes, cogeneration, biomass, concentrated solar power and geothermal plants. ORC is also known for its flexibility in terms of capacity & working temperatures.

The thermodynamics of an ORC is similar to a Rankine steam cycle however, the ORC employs an organic fluid instead of water/steam as the working fluid. A layout of a generic ORC is shown in the figure 1.1(a) along with a T-S diagram (figure 1.1(b)) illustrating the positions of various processes. The liquid working fluid is compressed in the pump $(1-2)$ and pumped to the evaporator to gain thermal energy and undergo a phase change $(2-3)$. Before evaporation, the organic fluid enters a recuperator for pre-heating and exploit the heat from the turbine's exhaust. The fluid in the evaporator can be superheated or gain only the latent heat to reach the saturated vapour line. The enthalpy drop in the turbine is converted into mechanical energy which is later converted into electrical energy by an electrical generator coupled with the turbine $(3-4)$. Finally, the expanded fluid is cooled off in the condenser $(4-1)$ after giving away heat to the liquid fluid in the recuperator and the thermodynamic cycle is closed.

The characteristic feature of ORC is the usage of a higher molecular weight organic fluid as the energy carrier. These organic fluids are low boiling fluids in comparison with water, which permits its usage for lower temperature heat sources typically between $80^o - 300^oC$. A study by Chen et al [5] summarizes various organic fluids available for energy conversion and the impact of their physical properties on cycle performance. The availability of many potential candidates for the working fluid allows for an additional degree of freedom in designing of an efficient thermodynamic cycle. This aspect gives ORC its flexibility to be tailor made for a specific application [6]. These features also give ORC an edge over the traditional steam Rankine cycle as, for the same power output, the low specific heat of water would lead to smaller mass flows and higher enthalpy drops. This ultimately demands for more expansion stages and smaller flow passages thereby complicating the design. On the other hand, the high specific heat capacity of organic fluids produce higher mass flows and lower enthalpy drops [7]. This allows for supercritical cycle configurations even at low temperatures. Moreover, some of these complex fluids have intrinsic lubrication properties which reduce the frictional losses in

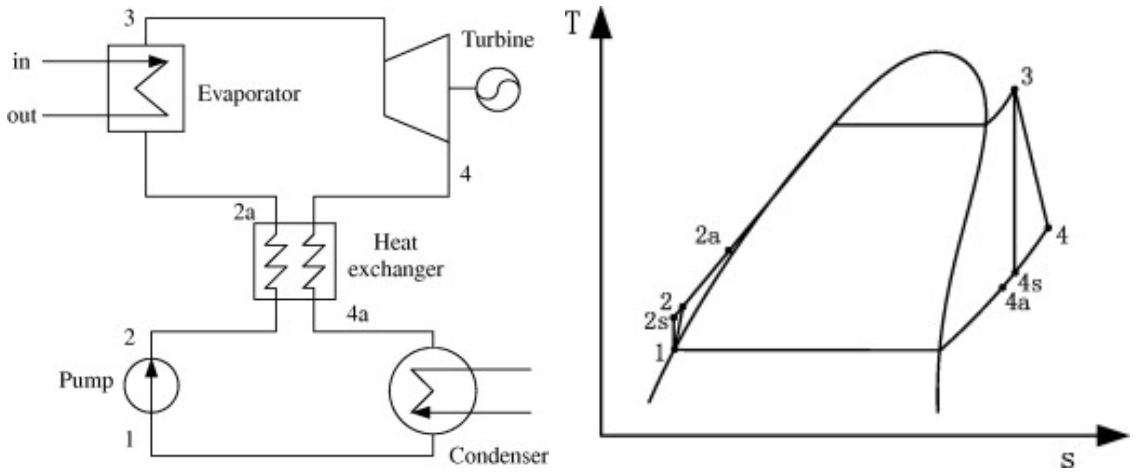

(a) Organic Rankine Cycle layout (b) Temperature-Entropy curve

Figure 1.1: Typical Organic Rankine Cycle thermodynamic process [Adapted from [1]]

the expander. The water lacks this property, therefore the steam expanders require other lubricants, making a challenging design and overall expansion efficiency is largely affected by blow-by losses [6]. Other benefits of organic fluids are their low critical pressure & temperature, low latent heat, high density in gaseous phase, high thermal conductivity and stability [1].

The choice of a working fluid is of utmost importance for an efficient cycle and an appreciable performance [8]. The fluid also affects the size of system components, design of the expander, system stability and environmental concerns. The ORC working fluids are divided in three broad categories depending on the slope of vapour saturation lines in the T-S diagram, a *wet* fluid with negative slope, an *isentropic* fluid with nearly infinite slope and a *dry* fluid with a positive slope [9]. The dry type organic fluids are considered better for most ORC applications as they eliminate the need to use a superheater because the vapour expansion takes place in the superheated vapour region [5]. Therefore, the saturated liquid cannot form to damage the low pressure stages. One common feature of most ORC organic fluids is their complex thermodynamic behaviour and departure from perfect gas laws. The expansion of such fluids in the region close to the vapour saturation curve exhibits non-classical fluid dynamics behaviour especially in transonic & supersonic regimes. This calls for a better understanding of the gas dynamics in this region.

1.1.1. Dense Gas Region

The high molecular complexity (higher number of active degrees of freedom) and strange fluid dynamics behaviour as observed in [10], suggests that a proper understanding of the peculiar behaviour of the ORC fluids is paramount when designing an ORC expander. These high molecular weight fluids operate in thermodynamic states closer to the saturation curve and the critical point, this is the so-called Dense-gas region where the real gas effects are dominant and the ideal gas laws are no longer valid.

The fluid behaviour in this region can be quantified by a parameter indicating the influence of high density gas phase on thermodynamic properties and the capability of forming the type of shock waves (compression or expansion) in arbitrary fluids. In 1971, Thompson found that the fluids can be organized according to the laws governing their thermodynamic properties based on the sign of this parameter to which he referred to as the *fundamental derivative of gas dynamics* (Γ) [10]

$$\Gamma = \frac{a^4}{2\xi^3}\left(\frac{\partial^2 \xi}{\partial P^2}\right)_s = 1 + \frac{\rho}{a}\left(\frac{\partial a}{\partial \rho}\right)_s, \tag{1.1}$$

where speed of sound, a = $\sqrt{-\xi^2\left(\frac{\partial P}{\partial \xi}\right)_s}$, P is the pressure, ρ is the density, ξ is the specific volume and s is the specific entropy. The fundamental derivative in equation 1.1, measures the rate of change of local speed of sound and provides the behavioral information about the thermodynamic properties. The value of Γ indicates the presence of local dense gas phenomenon. In the flow domain, if $\Gamma > 1$,

the gas behaves like an ideal gas i.e., the sound speed decreases during isentropic expansion, whereas it increases during isentropic compression and only compression shock waves are physically allowed. So, this case of classical behaviour has a constant value of $\Gamma = \frac{(\gamma+1)}{2} > 1$.

On the other hand , if $0 < \Gamma < 1$, the converse behaviour can be observed i.e., a rise in speed of sound through isentropic expansion, a drop through isentropic compression but in this case too, only compression shocks are allowed. However, the relative shock losses are lower in the dense gas regime. As mentioned by Bethe in his work [11], this feature is better understood by expanding the entropy change across a discontinuity as a series

$$\Delta s = -\left(\frac{\partial^2 P}{\partial \xi^2}\right)_s \frac{(\Delta\xi)^3}{12T} + \mathcal{O}((\Delta\xi)^4), \tag{1.2}$$

where $\Delta\xi$ is the specific volume variation across the discontinuity. The second derivative of pressure with respect to the specific volume variation at constant entropy shows the type of shock waves depending on its sign. If $\left(\frac{\partial^2 P}{\partial \xi^2}\right)_s > 0$, the shocks are of compressive type and if $\left(\frac{\partial^2 P}{\partial \xi^2}\right)_s < 0$, the expansive shocks are possible [11] & [12]. The positive values of $\left(\frac{\partial^2 P}{\partial \xi^2}\right)_s$ exist in the regions of vapour phase of fluids having $\Gamma > 0$. In the equation (1.2), only negative values of $\Delta\xi$ are allowed for positive values of $\left(\frac{\partial^2 P}{\partial \xi^2}\right)_s$ i.e., the compressive shock waves, to satisfy the second law of thermodynamics ($\Delta s > 0$). This behaviour is typically seen in dilute gas conditions, a region far from the critical point where the ideal gas law is valid. To observe the behaviour of fluids in proximity to the critical point (Dense gas), lets rewrite the equation (1.2) in terms of Γ using equation 1.1,

$$\Delta s = -\left(\frac{a^2}{6\xi^3 T}\right)\Gamma(\Delta\xi)^3 + \mathcal{O}((\Delta\xi)^4). \tag{1.3}$$

The above equation shows that for dilute gas conditions, where $\Gamma > 1$, the entropy variation is third degree order stable whereas, in the dense gas region ($\Gamma < 1$), the entropy variation is $\mathcal{O}(\Delta\xi)^4$. Therefore, close to the critical point the shock waves are one order less dissipative than in the ideal gas region, which is beneficial for the turbomachinery used in ORC systems as they tend to operate in the dense gas region.

The final region in the vapour phase of some fluids exists where $\Gamma < 0$, where the classical results of Gas dynamics are inverted [10]. These fluids show extremely non-linear behaviour close to the critical point & the saturation curve. These fluids are known as Beth-Zeldovich Thompson (BZT) gases named after the respective ground-breaking work of three scientists. In this region, the compression shock are not possible but the expansion shocks are theoretically expected. However, at present there is a significant lack of physical evidence of expansion shock waves in BZT gases. This phenomenon has been theoretically predicted for some organic fluids (such as siloxanes)[13] but this region would not be discussed further in the present work.

The ideal gas law is based on the assumptions that the intermolecular attractions between gas molecules are negligible and the gas molecules do not occupy a considerable volume themselves. These assumptions work fine at certain conditions such as low pressure and high temperatures. However, at high pressure and/or low temperature the actual behaviour of gases start deviating from the ideal gas. For such non-ideal conditions complex equations of states (EOS) are used to capture the real gas behaviour. In this work, the thermophysical data for the fluid properties close to the saturation curve is obtained from high accuracy CoolProp library [14]. This library is based on cubic EOS such as Peng-Robinson (PR) and Soave-Redlich-Kwong (SRK) [14]. The presence of real gas effects is described using the compressibility factor (Z), whose value is 1 for ideal gas and is less than zero in case of real gas.

1.2. ORC Expanders

An expander plays a crucial role in the designing of an efficient thermodynamic cycle as the work output comes from this component. There are two categories of expanders, depending on the operating conditions & the system size namely; turboexpanders & volumetric expanders. The turboexpanders

work on the dynamic action of a rotating rotor whereas, the volumetric expanders rely on the periodic change in the volume of the expansion chamber [15]. For small & medium sized ORC applications, the volumetric expanders (eg, screw, scroll, piston etc) have been extremely popular due to their low cost, mechanical simplicity & ease of installation. They ensure low flow rates whilst having lower rotational speeds, thus eliminating the need of a high speed generator or a gear box. However, they suffer from lower expansion efficiencies, leakage and lubrication losses [16] making them inefficient for high temperature and power applications. The turbomachines fit the profile better when it comes to high temperature, high pressure ratio and efficient expansion of fluids. However, the constraints posed by ORC operating conditions, like dense gas dynamics, compact size and high rotational velocities, make it essential to look for efficient design procedures. As mentioned earlier, in ORC the expanding organic vapours will be close to the critical point, where the molecular complexity of the gas dynamics become significant. The classical gas dynamics and simple gas relations will be grossly inappropriate in the cases of ORC [17]. Therefore, careful consideration of the peculiar dense-gas dynamics is required in early stages of designing an expansion device. Furthermore, low sound speed of the organic fluids along with high pressure ratios lead to supersonic flows, which can induce strong shock losses during the expansion process. The conventional turbines designed for subsonic flows result in extremely low aerodynamic performance of below 30% when subjected to high expansion ratios and thereby supersonic inlet flows [18].

The supersonic turbines have got the interest of the scientific community since the 1950s because of high specific power, reduction in the number of stages and hence lighter turbines with lower manufacturing & maintenance costs [19]. The low-reaction or impulse architecture is well-known, for steam turbines, to have the same benefits in one or two stages.

The design philosophy using Method of Characteristics (MOC) for supersonic axial impulse rotor was proposed in 1952 by Boxer et al [4] to turn the supersonic flows of perfect gases through large angles without shocks. In 1966, Colclough et al investigated the performance of supersonic axial impulse blades experimentally for perfect gases [20]. The effects of dense gases were included in the design of supersonic nozzles using Van der Waals equation of state in 1995 [21]. The design methodology was enhanced by including complex equations of state along with MOC to study the dense gas dynamics on the supersonic nozzles by Guardone et al [22]. In 2015, Bufi et al employed complex EOS in the MOC procedure to properly consider the dense gas effects on the design of supersonic axial rotor for the first time [23]. The axial turbines offer flexibility in terms of high efficiency over a range of rotational speeds while being able to accommodate multiple stages. However, the radial turbines are capable of even higher work output whilst having higher efficiencies over single-stage expansion [24]. The radial architecture offers other benefits over axial turbines such as better capability of dealing with large enthalpy drop within a single stage while having low peripheral speeds, higher efficiencies at off-design conditions, higher dynamic stability and better sealing structure [8]. Furthermore, the CFD simulations [25] suggests higher efficiencies in case of radial-inflow turbines compared to micro-axial turbines at pressure ratios higher than 3.0.

In literature, the majority of radial turbine designs are based on mean-line parametric analysis for preliminary design and 1D loss analysis followed by optimization using CFD simulations to maximize the performance. For instance, a design procedure to design a micro radial ORC turbine uses a mean-line model for preliminary design and 3D CFD simulations to improve the design [26]. In such procedures, the design parameters are adjusted iteratively until the desired results are obtained. This procedure lacks in certain aspects as it does not assure an optimum combination of the design parameters to achieve maximum turbine performance [27]. In addition such methods are extremely dependent on designer's experience to ensure the method's proper application. Moreover, the comparison of the efficiencies predicted by the 1D mean-line models with 3D CFD simulations may raise doubts about the accuracy of the mean-line models [25]. Therefore, a new design methodology is required that can generate radial turbine rotors by properly considering the flow equations and complexity of the organic fluids.

1.3. Motivation & Outline

The objective of this thesis is to introduce a novel design philosophy for supersonic radial turbine rotors for ORC applications. To the author's knowledge, no literature could be found that solves the governing

flow equations at the initial design phase of a supersonic radial rotor. The existing methods rely on optimizing 1D mean-line designs which are accurate only to a certain degree for subsonic & transonic flows. Especially in supersonic flow regime, due to the added complexity of the shock phenomenon, significant deviations can be found in 1D preliminary design methods and the CFD calculations [28].

This thesis attempts to design a supersonic radial rotor by taking into consideration the supersonic flow equations in the design procedure by implementing a mathematical model to solve hyperbolic PDEs. It extends the existing 2D design methodology of a supersonic axial impulse rotor which implements the Method of Characteristics. The proposed design procedure is developed and compared with inviscid CFD simulations for both perfect gas & real gas in the dense gas region. The deliverable of this project is a supersonic rotor design tool that can generate both axial & radial rotor blades in supersonic regime taking into account the real gas effects.

This thesis is divided into 4 chapters, starting from the basic concepts to the proposed design philosophy, each one building up on the previous one:

Chapter 2: Theoretical Framework presents a brief overview on the compressible flow. The governing equations used in the thesis work are derived and discussed mathematically. The method of characteristics to solve supersonic flow equations is introduced and elaborated.

Chapter 3: Supersonic Axial Rotor Blade Design starts by elaborating the conventional methodology to generate a supersonic axial rotor for perfect gas. The limitation of this method is discussed which is followed by the proposed solution to the limitation. The new procedure is implemented to generate the supersonic axial geometry and compared with the previous method. The procedure to add the capability to consider dense gas effects of organic fluids in the design of axial rotors is also discussed.

Chapter 4: Supersonic Radial Rotor Blade Design presents the new methodology by adding the body forces in the governing equations. The new equations are derived to be further used in MOC to generate a portion of the blade which is designed including the body force's influence. The real gas effects are also included in the process.

Chapter 5: Results & Discussions contains the resulting blades which are compared with steady inviscid CFD simulations to validate the design procedure. Different test case blades with and with out body force are simulated, including the perfect gas & real gas effects.

Chapter 6: Conclusions & Recommendations concludes this thesis work and puts forth future perspectives to take on this research work.

2

Theoretical Framework

This chapter briefly lays out the basics of compressible flows which is followed by the governing equations used in the design methodology of supersonic rotors. The nature of these governing partial differential equations of supersonic flow is discussed. Furthermore, the method of characteristics is elaborated and implemented for a basic PDE to explain the underlying procedure.

2.1. Compressible Flows

From the 18^{th} century to the early 20^{th} century, most of the fluid dynamics problems involved the flow of liquids or low-speed flow of gases. In both of these cases the fluid density can be assumed as constant. Hence, the flow problem can be described quite accurately with the incompressible flow equations. However, with the advent of De Laval's convergent-divergent nozzle and supersonic flights later on, the density was observed to vary by high orders of magnitude [29]. Consequently, in such cases of high speed flows, the assumption of constant density throughout the flow field can no longer be justified. This marked the departure from the conventional methods to study flows (incompressible) to compressible fluid flows.

As the name suggests, in the description of compressible fluid flows the role of varying density throughout the flow field is also taken into account. The density change $(d\rho)$ of the fluid is represented in terms of compressibility (τ) and the change in pressure (dp) by the following expression;

$$\tau = \frac{1}{\rho}\frac{d\rho}{dp}. \tag{2.1}$$

A fluid in motion is always accompanied by the presence of pressure changes in one way or another, it can be initiated or maintained by difference in pressure. In particular, the high-speed flows are characterized by large pressure gradients. In case of liquid flows, the compressibility (τ) values are lower therefore, a relatively higher change in pressure due to the flow in equation (2.1), results in high flow velocities without much variation in density. Hence, such flows can safely be assumed as incompressible (constant ρ). In contrary, the τ values for gaseous flows are higher which results in substantial variations in density with large flow pressure gradients. This variable density is also accompanied by high velocities in high-speed flow of gases. Such flows are known as compressible flows [29].

A way to characterize the flow velocities is in the form of Mach number (M). It is a ratio of the flow velocity and the local speed of sound. The sound speed is defined as the speed at which the acoustic waves propagate through a fluid medium. It is also known as the sonic speed (a) and is generally expressed as

$$a^2 = \left(\frac{\partial P}{\partial \rho}\right)_s. \tag{2.2}$$

The various values of Mach number give rise to different flow regimes as illustrated in figures 2.1(a),2.1(b) & 2.1(c). These figures show the pressure waves generated by an airplane in a ho-

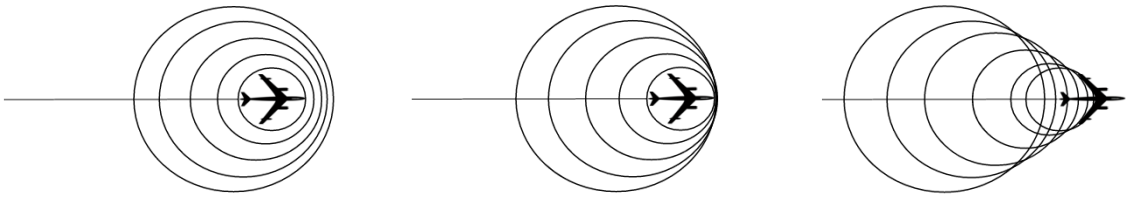

(a) Subsonic velocity ($M < 1$) (b) Sonic velocity ($M = 1$) (c) Supersonic velocity ($M > 1$)

Figure 2.1: Different flow regimes shown by the pressure waves generated by an object moving at different velocities [2]

mogeneous fluid. These pressure waves propagate at the sound speed in all directions. When the airplane is stationary, these waves travel in concentric circles without interacting with each other. In figure 2.1(a), the aircraft's velocity is lower than the sound speed so, $M < 1$ and the flow is known as *subsonic*. In this case, the pressure waves travel with an offset with respect to each other due to the motion of the aircraft which leads to local fluid compression in the downstream direction. In case the aircraft's velocity is equal to the speed of sound in the fluid, then the flow is called *sonic* ($M = 1$). The pressure waves in sonic condition interact with each other as they coalesce at one point (figure 2.1(b)) and give rise to complicated flow phenomenon [2]. However, when the Mach number is in the range $0.8 \leq M \leq 1.2$, the flow field is defined as *transonic*. The *supersonic* flow is characterized by higher velocities than the sound speed i.e., $M > 1$ in figure 2.1(c). In this case, the pressure waves generated at later time can interact with the previously generated waves, which further compresses the fluid and give rise to an even stronger pressure wave called a Mach wave. This wave forms a conical wave front known as a Mach cone. Lastly, for the values $M > 5$, the flow enters the so-called *hypersonic* regime. For the purposes of this thesis, we will stick to the supersonic flow regime.

It has been observed in the cases of Mach number lower than 0.3, the pressure change remains small enough to govern a smaller density change, even with high compressibility values of gases. Thereby, making the assumption of incompressibility valid for low-speed gaseous flows. However, in the present work, the Mach number is greater than 1 so the effects of density variations will play a major role.

2.2. Governing Equations

The flow field in an axial rotor blade is considered to be two-dimensional, steady, compressible, irrotational & supersonic. The governing equations of such a flow field are the *Gas dynamics* equation, the *irrotationality* condition and the *speed of sound* equation [30]. The Gas dynamics equation is derived in the following section along with the effect of external body forces as this aspect is used later to design a supersonic rotor for radial turbines. Let us take a look at these equations closely one by one.

2.2.1. Gas Dynamics Equation

The Gas Dynamics equation is derived from the *continuity* equation, *Euler's momentum* equation and *speed of sound* equation. The derivation is performed in *Gas Dynamics* by *Zucrow & Hoffman*[30] for negligible body force assumption. However, in the following discussion the derivation is undertaken including the body forces' contribution.

Continuity Equation: The non-conservative form of the continuity equation is expressed as

$$\frac{D\rho}{Dt} + \rho\nabla \cdot \vec{V} = 0. \tag{2.3}$$

Euler's momentum equation: The Euler's equation for 2D inviscid flow of a compressible fluid with external body forces in non-conservative form is given by

$$\rho \frac{D\vec{V}}{Dt} = -\nabla P + \rho \mathbf{F_B}, \tag{2.4}$$

where $\vec{V}$ is the velocity vector $[u\ v\ w]$ with its respective components in x, y & z directions, P is the pressure and $\mathbf{F_B}$ is the body force vector $[F_{Bx}\ F_{By}\ F_{Bz}]$ with its components in the respective directions.

Now expanding the material derivative term in the momentum equation and assuming 2D steady state condition $\left(\frac{\partial \vec{V}}{\partial t} = 0\right)$, we get the Euler's momentum equation in x-direction & y-direction as

$$\rho\left(\vec{V} \cdot \nabla u\right) = -\frac{\partial P}{\partial x} + \rho F_{Bx}, \tag{2.5a}$$

$$\rho\left(\vec{V} \cdot \nabla v\right) = -\frac{\partial P}{\partial y} + \rho F_{By}. \tag{2.5b}$$

Using the vector identity $\{\vec{V} \times (\nabla \times \vec{V}) = \nabla\left(|\vec{V}|^2/2\right) - \vec{V} \cdot \nabla\vec{V}\}$ [30], in the equation above gives the following expression,

$$\rho\left[\nabla\frac{|\vec{V}|^2}{2} - \vec{V} \times (\nabla \times \vec{V})\right] = -\nabla P + \rho \mathbf{F_B}. \tag{2.6}$$

The flow field is assumed to be irrotational. The irrotationality condition states the absence of vorticity $(\omega = 0)$ in the flow, which means that the curl of the velocity field is zero $(\nabla \times \vec{V} = 0)$. Substituting this condition into the equation (2.6) yields a reduced form of Euler momentum equation,

$$\rho\left(\nabla\frac{|\vec{V}|^2}{2}\right) + \nabla P - \rho \mathbf{F_B} = 0. \tag{2.7}$$

In the end, performing a scalar product of $\vec{V}$ with the equation (2.7) to generate,

$$\rho(\vec{V} \cdot \nabla)\left(\frac{|\vec{V}|^2}{2}\right) + (\vec{V} \cdot \nabla)P - \rho\vec{V} \cdot \mathbf{F_B} = 0. \tag{2.8}$$

For an isentropic flow, the partial derivatives in the speed of sound equation (2.2) can be expressed as total derivatives along a streamline. Writing those total derivatives as material derivatives to obtain,

$$\frac{DP}{Dt} - a^2\frac{D\rho}{Dt} = 0. \tag{2.9}$$

In the cases of isentropic flows, the equation (2.9) can be used in place of the energy equation, thus simplifying the governing equations by removing the enthalpy derivatives. It is also employed to eliminate the density derivatives from the continuity equation (2.3), thereby yielding an alternative form of continuity equation given as,

$$\frac{DP}{Dt} + \rho a^2 \nabla \cdot \vec{V} = 0. \tag{2.10}$$

Expanding the material derivative in the expression above to eliminate the time derivative as the flow is assumed to be steady $\left(\frac{\partial P}{\partial t} = 0\right)$, the remaining equation becomes,

$$(\vec{V} \cdot \nabla)P + \rho a^2 \nabla \cdot \vec{V} = 0. \tag{2.11}$$

Combining equations (2.8) & (2.11) to eliminate ∇P yields the desired *Gas Dynamics* equation with body forces expressed in its general form as,

$$(\vec{V} \cdot \nabla)\left(\frac{|\vec{V}|^2}{2}\right) - a^2 \nabla \cdot \vec{V} - \vec{V} \cdot \mathbf{F_B} = 0. \tag{2.12}$$

On comparing equation (2.12) with the gas dynamics equation derived in [30], the presence of extra term (body forces) can be noticed. Expanding the gas dynamics equation with body forces in 2D Cartesian coordinates gives

$$(u^2 - a^2)u_x + (v^2 - a^2)v_y + uv(u_y + v_x) - uF_{Bx} - vF_{By} = 0, \tag{2.13}$$

where u_x, v_y, u_y & v_x are the partial derivatives of u & v with respect to x & y. We know that 2D irrotationality condition ($\omega = 0$) requires,

$$u_y - v_x = 0. \tag{2.14}$$

Integrating this condition with the expanded expression (2.13) gives the gas dynamics equation for 2D steady irrotational flow of a compressible fluid with external body forces as following:

$$(u^2 - a^2)u_x + (v^2 - a^2)v_y + 2uvu_y - uF_{Bx} - vF_{By} = 0. \tag{2.15}$$

The Gas dynamics equation (2.15) can also be represented for the case of no external body force contribution by simply putting the body force components equal to zero, thus expressing 2D steady irrotational compressible flow as derived in [30],

$$(u^2 - a^2)u_x + (v^2 - a^2)v_y + 2uvu_y = 0. \tag{2.16}$$

2.2.2. Nature of *Gas Dynamics* Equation

In this section, the classification of the gas dynamics equation is discussed. First, the 2D gas dynamics equation (2.15) is written in terms of the velocity potential function [$\Phi(x, y)$] by substituting the flow velocities in terms of the potential function as, $u = \partial\Phi/\partial x$ & $v = \partial\Phi/\partial y$, to obtain a second-order PDE given by

$$\left(\Phi_x^2 - a^2\right)\Phi_{xx} + \left(\Phi_y^2 - a^2\right)\Phi_{yy} + 2\Phi_x\Phi_y\Phi_{xy} - \Phi_x F_{Bx} - \Phi_y F_{By} = 0. \tag{2.17}$$

This is the potential equation for a steady 2D irrotational flow, where $\Phi_{xx} = \frac{\partial^2\Phi}{\partial x^2}$ & $\Phi_{xy} = \frac{\partial^2\Phi}{\partial xy}$. It is a non-homogeneous PDE, linear in terms of the second derivatives and can be related to the general form of second-order PDE as,

$$Au_{xx} + Bu_{xy} + Cu_{yy} + Du_x + Eu_y + Fu = 0, \tag{2.18}$$

where $u = u(x, y)$. The general partial differential equation can be classified into 3 distinct categories depending on the determinant $(B^2 - 4AC)$ being positive, negative & zero. If the criteria $(B^2 - 4AC)$ is positive, then the equation is hyperbolic; if it is negative, then the equation is elliptic and if it is zero, the equation is parabolic.

To get a convenient form of equation (2.17), it is divided by $-a^2$ to get the following expression:

$$\left(1 - \frac{u^2}{a^2}\right)\Phi_{xx} - \frac{2uv}{a^2}\Phi_x\Phi_y + \left(1 - \frac{v^2}{a^2}\right)\Phi_{yy} + \frac{F_{Bx}}{a^2}\Phi_x + \frac{F_{By}}{a^2}\Phi_y = 0. \tag{2.19}$$

For the above equation the classification criteria $(B^2 - 4AC)$ is given as

$$B^2 - 4AC = \frac{4u^2v^2}{a^2} - 4\left(1 - \frac{u^2}{a^2}\right)\left(1 - \frac{v^2}{a^2}\right), \tag{2.20}$$

$$= \frac{V^2}{a^2} - 1, \tag{2.21}$$

$$= M^2 - 1. \tag{2.22}$$

Therefore, seeing the dependence of classification criteria on Mach number it can be observed that

- For subsonic flow ($M < 1$), $(B^2 - 4AC) < 0$ suggesting that equation (2.17) is elliptic

- For sonic flow ($M = 1$), $(B^2 - 4AC) = 1$ suggesting that equation (2.17) is parabolic
- For supersonic flow ($M > 1$), $(B^2 - 4AC) > 0$ suggesting that equation (2.17) is hyperbolic

It should be noted that the presence of body forces in equation (2.17) does not affect the classification criteria as the coefficients of second-order derivatives are used in determining the determinant. Since the flow field under consideration is supersonic, the hyperbolic nature of the governing PDEs is confirmed. Furthermore, it also verifies the applicability of the Method of Characteristics on this equation for supersonic flows as described in the section below, the MOC is valid only for hyperbolic PDEs.

2.3. Method of Characteristics

This section gives a brief theoretical insight on the procedure used to solve quasi-linear hyperbolic partial differential equations (PDEs), known as the Method of Characteristics (MOC). The quasi-linear partial differential equations of first-order are the ones that can be non-linear in their dependent variables but are linear in their first partial derivatives.

The governing equations of inviscid compressible supersonic flow are hyperbolic PDEs as established in the previous section. In the case of subsonic flow, the governing PDEs are elliptic in nature which entails the dependence of flow properties/solutions on the upstream and downstream boundary conditions. Whereas for supersonic flows, the flow properties at each point in the flow field depend on the properties in a finite region of upstream flow field, while being independent of the downstream conditions. Thus, a marching-type numerical method needs to be implemented to get the solutions of such flow fields. The most accurate marching-type method to solve quasi-linear hyperbolic PDEs is the Method of Characteristics [30].

The MOC involves manipulating the given governing PDE into two equations known as the *characteristic* & *compatibility* equations. The characteristic equation represents the slope of the line along which the disturbances propagate. Lets understand the term 'characteristics' from a physical and mathematical point of view as properly elaborated in the book *Gas Dynamics by Zucrow & Hoffman* [30]:

1. The characteristic (short for characteristic curve) is physically defined as the path of propagation of physical disturbances across which the physical properties encounter steep gradients. For instance, in supersonic flow fields, the discontinuities propagate along the Mach lines hence, these lines are the characteristics of the supersonic flow field.

2. From mathematical perspective, a characteristic is a curve across which a physical property remains continuous but its derivative may or may not be discontinuous. In addition, along a characteristic curve a governing partial differential equation can be manipulated to obtain a total differential equation.

This total differential equation is a reduced representation of the governing partial differential equation and is known as the compatibility equation, valid only along the characteristic curve. The compatibility equations are solved along two intersecting characteristics to obtain the values of two variables at a point in the flow field defining the flow properties.

Due to the supersonic flow in the divergent section of the nozzle and hyperbolic nature of the governing equations in that section, MOC is widely used to design the diverging section of a convergent-divergent nozzle (De Laval nozzle) as illustrated in the figure 2.2.

The implementation procedure of the Method of Characteristics can be understood better with a conceptual diagram shown in the figure 2.3. As mentioned before, the solutions to hyperbolic equations solely depend on the upstream conditions, so the solution has to be initiated through an initial value line (IV_o) represented by the line AE in the figure. Along this line the values are known at points $A - E$. The solutions propagate from the initial line along the characteristic curves further into the domain. The colored background in the image represents the domain of dependence of point $'I'$, which is the region bounded by the outermost characteristics (AI & EI) and the initial value line. The solution points depending on points A & E lie in this region. The red (C+) & blue (C-) colored lines in the figure are the characteristic lines with positive and negative slopes respectively, passing through each point in the

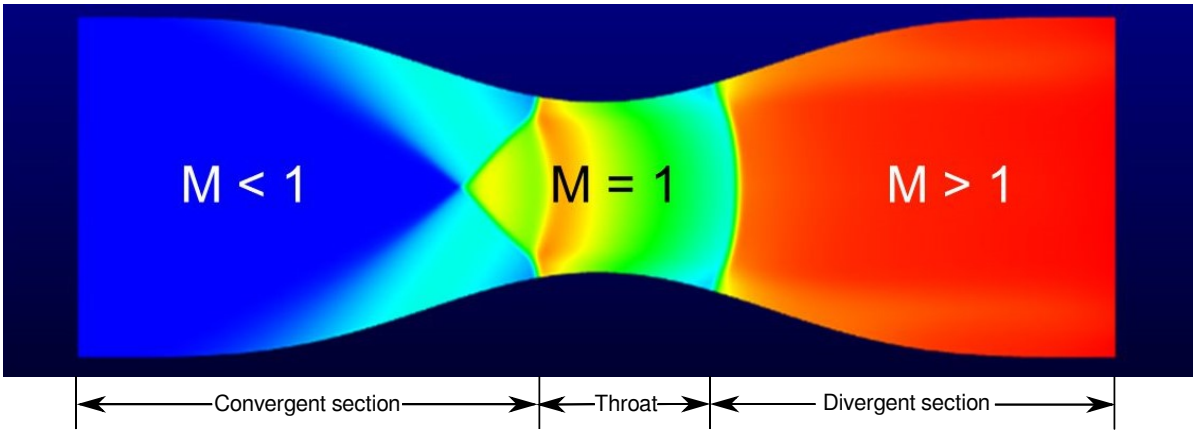

Figure 2.2: De Laval nozzle [3] depicting the Mach number variations in its sections. The supersonic flow in its divergent section allows MOC to be used for designing this section

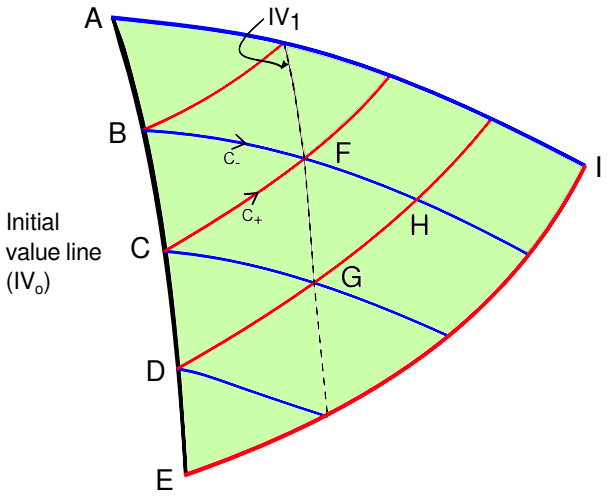

Figure 2.3: Method of Characteristics solution

supersonic (hyperbolic) flow field. These lines always travel in the downstream direction. The positive characteristic from point $'C'$ intersects with the negative characteristic from the neighbouring point $'B'$ in the flow field which generates a new solution point 'F' in the downstream direction. The compatibility equations are solved along the respective characteristics to obtain the flow properties at that point of intersection. Due to the marching nature of this method, the solution points thus obtained act as the initial value line (IV_1) for the set of points further downstream. In this manner, the flow properties are obtained in the entire flow domain.

Let us get a deeper insight on the general features of the MOC by deriving the characteristic & compatibility equations for a first-order partial differential equation of a function $f(x, y)$ [30]. The procedure to obtain the characteristic and compatibility equations is illustrated in the flow chart 2.4.

$$a\frac{\partial f}{\partial x} + b\frac{\partial f}{\partial y} + c = 0, \tag{2.23}$$

where the coefficients a & b and the non-homogeneous term c can be the functions of x, y & f. The function $f(x, y)$ is restricted to be a continuous function. Assuming the characteristic for the equation above is defined by slope λ, given by

$$\lambda(x, y, f) = \frac{dy}{dx} = \frac{b}{a}. \tag{2.24}$$

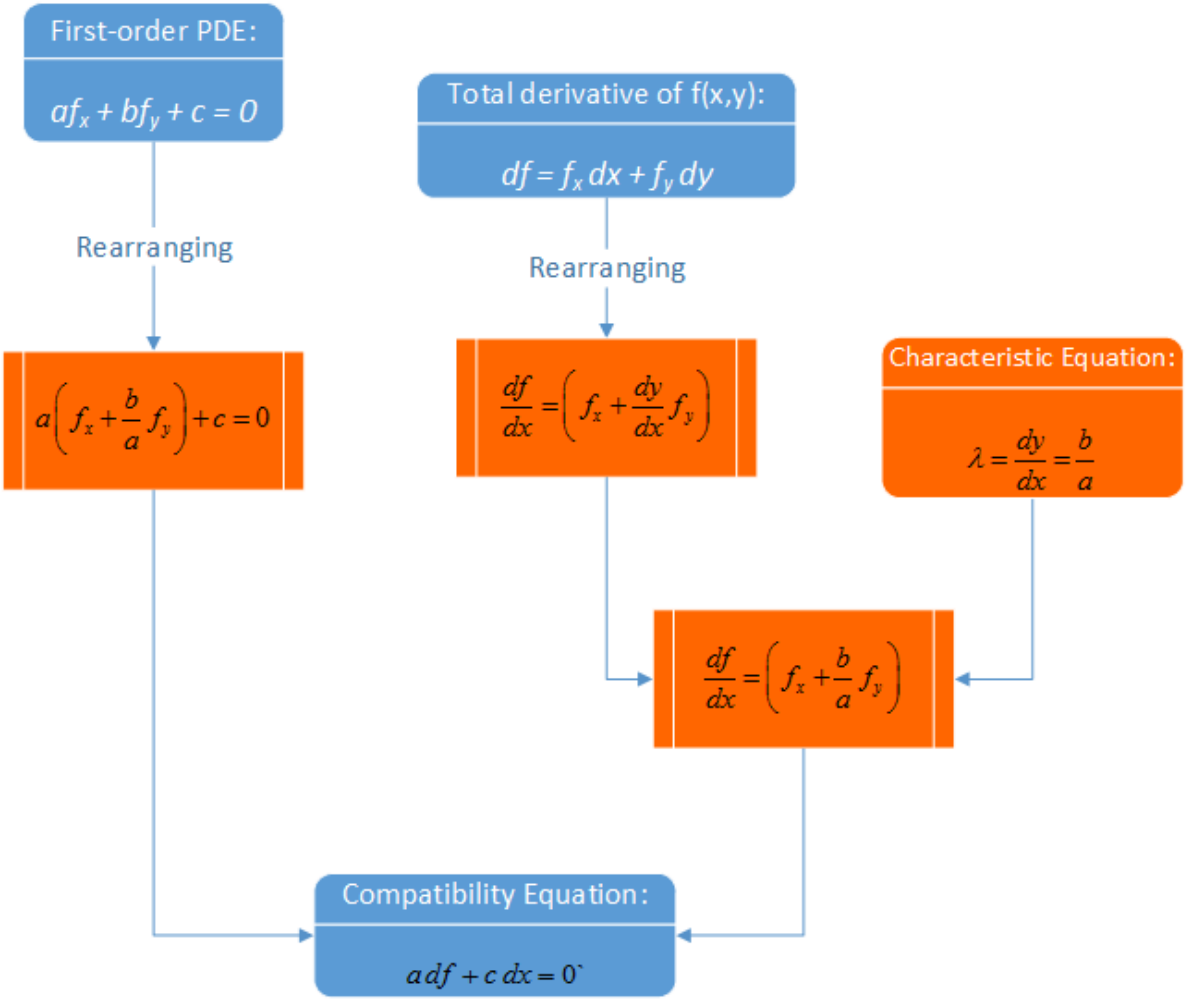

Figure 2.4: MOC flowchart to get characteristic & compatibility equations

3

Supersonic Axial Rotor Blade Design

This chapter introduces the conventional design methodology to generate supersonic axial rotors for perfect gas. The short coming of this process is discussed in terms of its inability to account for additional effects on the rotor geometry. The potential solution is proposed and implemented to modify the design philosophy for perfect gases. In the end, the non-ideal effects of dense gases are also incorporated in both design methodologies to generate supersonic axial rotor blades in the dense gas region.

The pioneering design methodology to obtain 2D supersonic impulse compressor or turbine blade geometries for perfect gases was proposed by Boxer et al (NACA) in 1952 [4] and translated in a computer program in 1965 by Goldman et al (NASA) [31]. In supersonic rotor vanes, the flow turning is achieved by the vortex-type velocity distribution in the concentric circular arc section. Such velocity distribution is attained by the transition arcs by continuously changing the supersonic flow direction as elaborated in the next section. In this method, the design of transition arcs depend on the Prandtl-Meyer angles. A design tool based on this methodology, developed as a part of this thesis, is called the *"Boxer tool"*.

This design procedure of the transition arcs is not flexible to take into account the external effects, for instance, the body forces. As elaborated in the next chapter, the radial rotor blade is expected to be generated by incorporating the external forces in the transition arcs' design. In this chapter, the supersonic axial rotor design technique is modified by eliminating the use of Prandtl-Meyer angles to define the flow turnings in the transition arcs. This is achieved by applying MOC on the compatibility equation directly, thus giving a more generic supersonic rotor design methodology. The governing equations for this procedure are derived and explained later in this chapter, followed by implementing it to obtain the transition arcs of the axial rotor. A design tool based on this methodology is also developed and is referred to as the *"COMOC tool"*, compatibility equations solved using MOC procedure.

The design procedure valid for perfect gases cannot be used to yield an efficient blade geometry for the typical operating conditions of an ORC turbine. As these are fairly close to the working fluid's vapour-liquid saturation curve and for some cycles can be supercritical. In that region, strong dense gas effects render the conventional supersonic blade geometry highly inefficient as the ideal gas laws are no longer a valid definition of the thermophysical relations. Therefore, a novel design approach, proposed by Bufi et al [23], is employed to both Boxer & COMOC tool to properly consider the dense gas effects in geometry determination. After adding the dense gas considerations in the Boxer tool, its name is modified to *"Boxer-Bufi tool"*, whereas the COMOC tool's name remain the same. The complex behaviour of organic working fluids is taken into account by generalizing the MOC procedure for gases governed by complex equation of states.

3.1. Supersonic Axial Rotor Design using Prandtl-Meyer Function

The design methodology to generate supersonic impulse axial rotor geometry introduced by *Goldman*[32] & Boxer et al.[4] is applicable only for perfect gases. This design philosophy, presented in

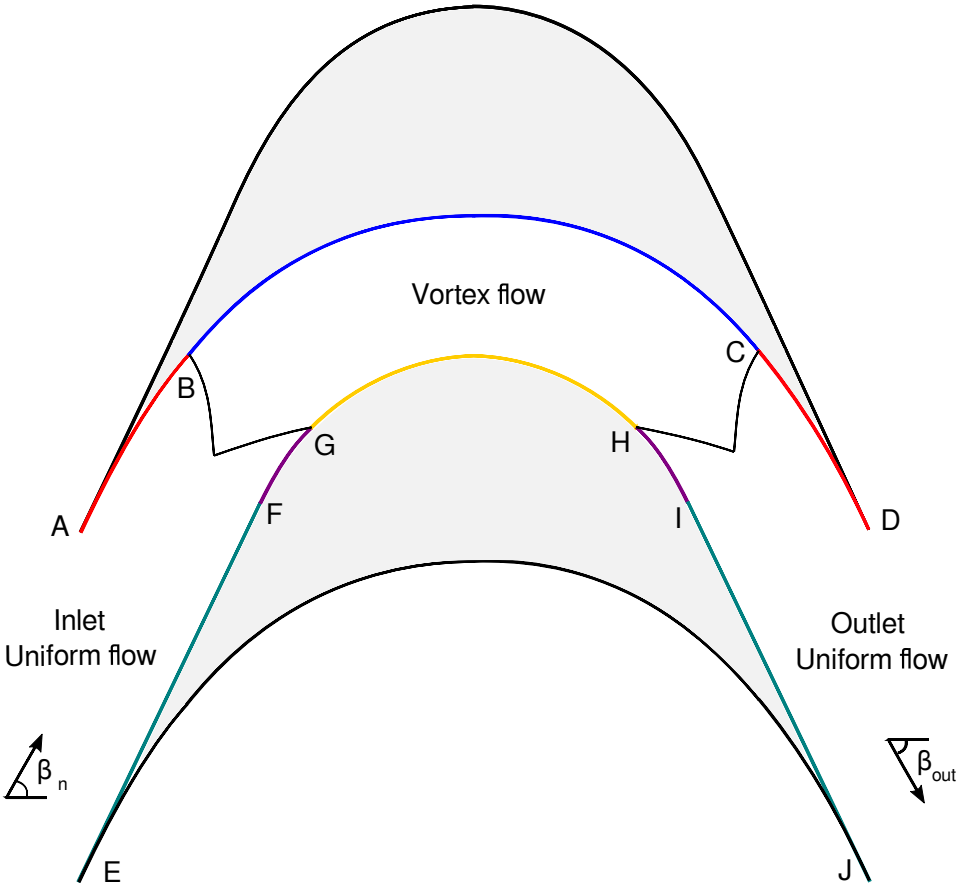

Figure 3.1: Supersonic axial rotor blade sections, where AB is Inlet lower transition arc, BC is Lower circular arc, CD is Outlet lower transition arc, FG is Inlet upper transition arc, GH is Upper circular arc, HI is Outlet upper transition arc, EF is Inlet straight line & IJ is Outlet straight line.

this section, establishes the intrinsic role played by the *Prandtl-Meyer angles* in the procedure which limits its application only to the perfect gases as these angles can only be defined using perfect gas laws.

The methodology in [4] & [32] revolve around the idea of obtaining shock-free supersonic flow passage between two concentric circles that can turn a supersonic fluid flow through large angles without giving rise to local shocks. To achieve this, the blade design has been divided in three sections: the inlet transition arc to gradually transform the inlet supersonic uniform flow into the vortex-type flow, the concentric circular arc section to maintain the vortex-flow while turning the flow, and the outlet transition arc to transit the vortex flow back to uniform flow conditions at the blade exit as illustrated in the figure 3.1.

3.1.1. Circular Arc Section

To begin-with the supersonic rotor design, let us first look at the flow in the circular arc flow passage which is composed of two concentric circular arcs. One of these arcs forms the pressure side of the top blade, hereinafter called as the lower circular arc and the other one forms the suction side of the bottom blade, hereinafter known as the upper circular arc. The beneficial aspect of this design choice is that the supersonic flow between two concentric circles follows the free-vortex flow. In this kind of flow, the streamlines are concentric to each other and the flow velocity varies inversely with respect to the distance from the circular arcs' centre. Figure 3.2 shows the characteristic line network between two concentric circles having a supersonic vortex flow. The characteristic lines formed in such supersonic vortex flow are reflected off the top & bottom circular surface in this manner. The same network is observed in the blade's circular arc section as shown in figure 3.3.

The main reason to choose vortex-type velocity distribution for the supersonic rotor blade design is

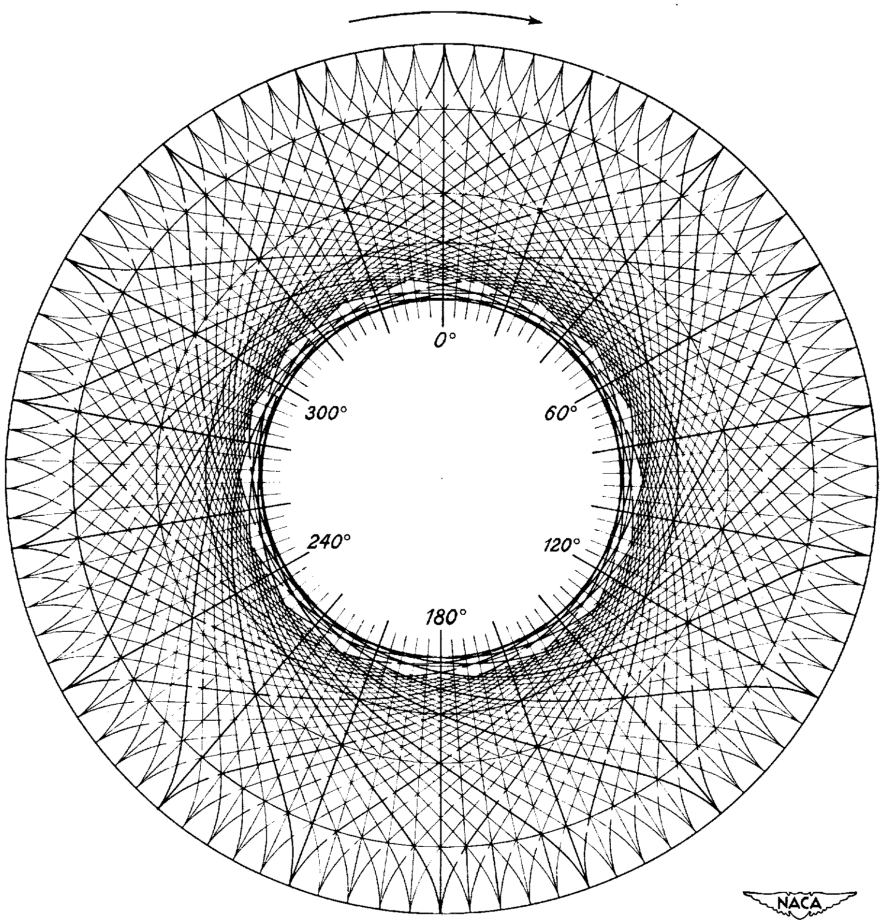

Figure 3.2: Characteristic line network between two concentric circles harbouring supersonic vortex flow [4]

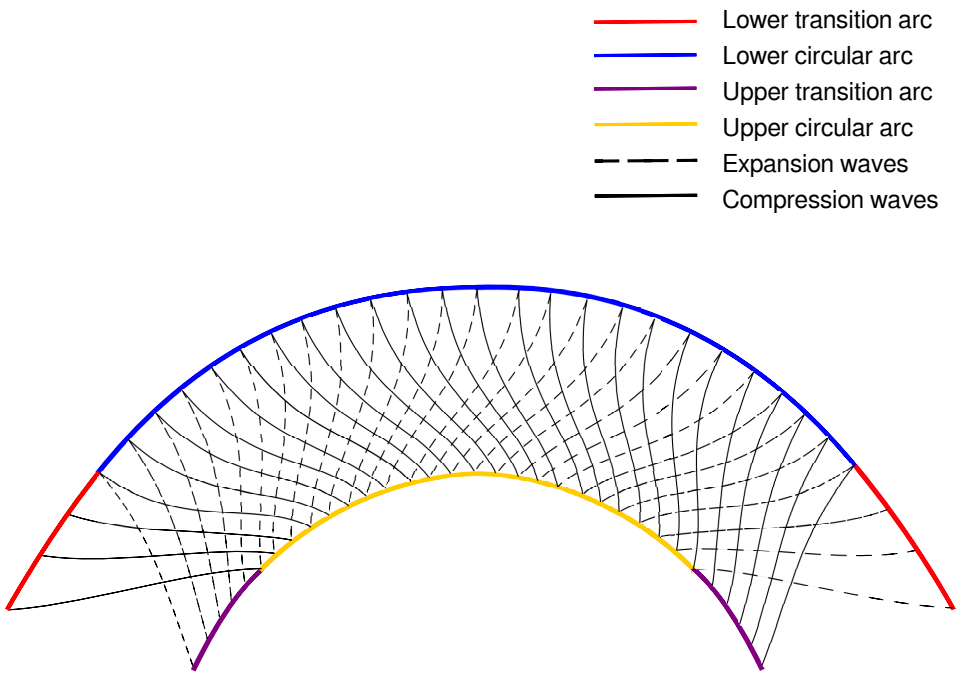

Figure 3.3: Compression & expansion waves in vortex flow in circular arc section

that, for a given peak surface pressure, the maximum loading in a concentric passage can be achieved by a uniform upper & lower surface pressure, which is attainable by the vortex flow [4]. This is done by a user-defined Mach number (static pressure) along the upper & lower section of the concentric supersonic vortex flow passage. Furthermore, if the flow entering the circular section is uniform and irrotational with no stagnation enthalpy & entropy gradient in the stream-normal direction, then the vortex flow will also remain irrotational. This flow is characterized by a constant velocity along any streamline given by the general vortex equation,

$$V.R = constant, \tag{3.1}$$

where V is the constant velocity magnitude along the streamline and R is the radius of curvature of that streamline following an isentropic transformation. The equation above is normalized by the critical velocity $(V_{critical})$ and the corresponding radius of the sonic velocity streamline (r^*), which gives an important dimensionless relation between critical velocity ratio (M^*) & dimensionless radius of the vortex flow field (R^*),

$$\frac{V}{V_{critical}} \cdot \frac{R}{r^*} = \frac{constant}{V_{critical} \cdot r^*}. \tag{3.2}$$

The critical velocity is the speed of sound at a point in the flow field for which the Mach number is 1 [4]. At $V = V_{critical}$ & $R = r^*$, the *constant* term in the equation above is $(V_{critical}.r^*)$, therefore we get

$$M^* \cdot R^* = 1. \tag{3.3}$$

The critical velocity ratio is also expressed in terms of the Mach number and the specific heat capacity ratio (γ) for a perfect gas [4], given by

$$M^* = \sqrt{\frac{M^2(\gamma-1)/2}{1+M^2(\gamma-1)/2}}. \tag{3.4}$$

In order to restrict the flow to the supersonic realm, the Mach number in equation (3.4) must be greater than 1. Hence, the values of R^* are restricted between 1 & $\sqrt{\frac{\gamma-1}{\gamma+1}}$.

Another benefit of using the circular arc section is the reduced labour to design the entire blade shape. The major design challenge is only to generate the inlet section of the blade such that it can perform a smooth transition of incoming supersonic uniform flow into the desired vortex flow as it enters the concentric circular arc section and conversely back to the uniform flow at the blade's outlet. In other words, the lower transition arc progressively reduces the inlet Mach number (M_{in}) to the targeted pressure/lower side Mach number (M_{lo}) and upper transition arc raises it to the suction/upper side Mach number (M_{up}). The transition arcs constitute a series of straight line segments that change the direction of incoming uniform parallel flow and intersects with the straight characteristic/Mach lines at every flow turning.

In isentropic turning of supersonic flows, the desired flow deviation to achieve the required Mach number is evaluated through *Prandtl-Meyer angle* $[\nu(M^*,\gamma)]$, expressed in equation below valid for a perfect gas. This angle represents the amount of turning required to reach the desired Mach number from Mach number 1 and is represented as

$$\nu = \frac{\pi}{4}\left(\sqrt{\frac{\gamma+1}{\gamma-1}}-1\right)+\frac{1}{2}\left\{\sqrt{\frac{\gamma+1}{\gamma-1}}\sin^{-1}[(\gamma-1)M^{*2}-\gamma]+\sin^{-1}\left(\frac{\gamma+1}{M^{*2}}-\gamma\right)\right\}, \tag{3.5}$$

where M^* is the critical velocity ratio given by equation (3.4). Therefore, for any desired Mach number, a corresponding critical velocity ratio exists and consequently a Prandtl-Meyer angle in case of a perfect gas. Now the flow turnings desired by the transition arcs can be analytically expressed in terms of Prandtl-Meyer functions as the targeted Mach number on the lower circular arc (M_{lo}) has a Prandtl-Meyer angle (ν_{lo}) & similarly, along the upper circular arc (ν_{up}).

For the supersonic rotor design, the relative parameters are considered to be in the rotor's reference frame. Therefore, considering a user-defined inlet relative Mach number with its corresponding Prandtl-Meyer angle (ν_{in}), the flow turning required to be achieved by inlet & outlet lower transition arc can be given by $[\nu_{in}(M^*_{in})-\nu_{lo}(M^*_{lo})]$ & $[\nu_{out}(M^*_{out})-\nu_{lo}(M^*_{lo})]$ respectively. Similarly the turning by the inlet & outlet upper transition arc would be $[\nu_{up}(M^*_{up})-\nu_{in}(M^*_{in})]$ & $[\nu_{up}(M^*_{up})-\nu_{out}(M^*_{out})]$ respectively. The amount of turning introduced by the inlet & outlet transition arcs cannot exceed the inlet (β_{in}) & outlet (β_{out}) relative flow angles, respectively.

As we know from the vortex-flow theory, the circular arcs are designed to maintain their corresponding Mach numbers throughout the concentric circular region. It can be seen that once the Mach numbers at the lower & upper circular arcs are defined, the critical velocity ratios M^*_{lo} & M^*_{up} are fixed too using equation (3.4). This leads to the determination of the values of R^*_{lo} & R^*_{up} with the expression (3.3). This gives the initial point of the lower & upper circular arc in non-dimensional axes defined as $X^* = x/r^*$ & $Y^* = y/r^*$, where r^* is the radius of curvature of the sonic streamline. In addition, the flow turning (α) induced in both upper & lower circular arc section at the blade's inlet & outlet are determined by considering the inlet & outlet relative flow angles

$$\alpha_{lo,in} = \beta_{in} - (\nu_{in} - \nu_{lo}), \tag{3.6a}$$
$$\alpha_{lo,out} = \beta_{out} + (\nu_{out} - \nu_{lo}), \tag{3.6b}$$
$$\alpha_{up,in} = \beta_{in} - (\nu_{up} - \nu_{in}), \tag{3.6c}$$
$$\alpha_{up,out} = \beta_{out} + (\nu_{up} - \nu_{out}), \tag{3.6d}$$

where all the angles measured in the counter-clockwise direction are considered positive. β_{in} is user-defined. However, β_{out} can be calculated as it is dependent on M_{in}, M_{out} & β_{in} as per the following consideration.

In an axial turbomachine, for an impulse-type (symmetric) blade section, the pitch (G) is constant and assuming a constant blade height (H) throughout the blade passage, the flow passage area ratio inlet to outlet is determined according to the equation

$$\frac{A_{in}}{A_{out}} = \frac{G.H.\cos\beta_{in}}{G.H.\cos\beta_{out}} = \frac{\cos\beta_{in}}{\cos\beta_{out}}. \tag{3.7}$$

For adiabatic conditions, the outlet static properties in a blade channel are evaluated by applying the compressible flow equations at any cross-sectional area (A_n) in the rotor passage using the mass conservation principle [33],

$$\frac{\dot{m}}{A_n} = \sqrt{\frac{\gamma}{RT_o}} \frac{P_o M}{\left(1 + \frac{\gamma-1}{2} M^2\right)^{\frac{(\gamma+1)}{2(\gamma-1)}}}, \tag{3.8}$$

where P_o & T_o are total pressure & temperature respectively. Considering negligible pressure loss and assuming constant flow properties, the mass flow rate $(\dot{m})$ per unit area across the rotor passage gives a new expression for the inlet to outlet area ratio by combining equations (3.7) & (3.8), which can be rearranged to yield β_{out} in terms of M_{in}, M_{out} & β_{in}, expressed as

$$\beta_{out} = -\cos^{-1}\left[\left\{\frac{M_{in}}{M_{out}}\left(\frac{1 + \frac{(\gamma-1)}{2} M_{out}^2}{1 + \frac{(\gamma-1)}{2} M_{in}^2}\right)^{\frac{(\gamma+1)}{2(\gamma-1)}}\right\} \cos\beta_{in}\right]. \tag{3.9}$$

With the user selected outlet Mach number (M_{out}), β_{out} can be determined and hence, all the flow turnings in the circular section are available using the equations (3.6). The entire concentric circular arc section can be easily calculated as the starting & ending points of the circular arcs are available.

3.1.2. Transition Arcs

In the case of symmetric (impulse) blades, $\nu_{in} = \nu_{out}$, the inlet & outlet transition arcs are equivalent so only one of them needs to be calculated. However, for asymmetric (reaction) blades, $\nu_{in} \neq \nu_{out}$, the two transition arcs are not identical as one is larger (with larger ν) than the other causing more flow turning in comparison to the other one. For the sake of simplicity, let us take a look at the design procedure of lower transition arc at the inlet in non-dimensional axes defined as $X_{lo}^* = X_{lo}/r^*$ & $Y_{lo}^* = Y_{lo}/r^*$. The lower transition arcs' design is initiated from the starting point of the lower circular arc section i.e., $(x_{lo}^*, y_{lo}^*) = (0, R_{lo}^*)$.

The arc coordinates are generated sequentially in a marching manner by intersecting the straight-line transition arc segments with the straight characteristic/Mach lines responsible for the gradual change in flow direction and thereby in the local Mach number. These Mach lines cross the major vortex-expansion characteristic which is generated at the starting point of upper/suction transition arc and intersects with the initial point $(0, R_{lo}^*)$ of the lower transition arc as illustrated in the figure 3.4. The arc wall segments are parallel to the local flow direction (ϕ_k) , thus these segments are determined using the flow angle at every transition arc coordinate. As mentioned in [4], the velocity direction (ϕ) can be expressed as a function of dimensionless radius (R^*) along the characteristic line given by

$$\phi = \pm\frac{1}{2} f(R^*) + const, \tag{3.10}$$

where

$$f(R^*) = \sqrt{\frac{\gamma+1}{\gamma-1}} \sin^{-1}\left(\frac{\gamma-1}{R^{*2}} - \gamma\right) + \sin^{-1}\left[(\gamma+1)R^{*2} - \gamma\right]. \tag{3.11}$$

The plus-minus sign in the equation (3.10) denotes two families of characteristic lines namely the expansion lines (positive) and the compression lines (negative). Applying the boundary condition at $x_{lo}^* = 0$ & $y_{lo}^* = R_{lo}^*$, the equation for major vortex-expansion characteristic line is obtained,

$$\phi = \frac{1}{2}\left[f(R^*) - f(R_{lo}^*)\right]. \tag{3.12}$$

The flow field is discretized into smaller sections by the characteristic lines, wherein the flow properties are assumed to be constant. However, these properties undergo a slight change across the characteristic lines. In these small flow field regions, the flow direction at each point along the characteristic line is considered to be parallel to the flow direction within the adjacent flow region. The transition arc

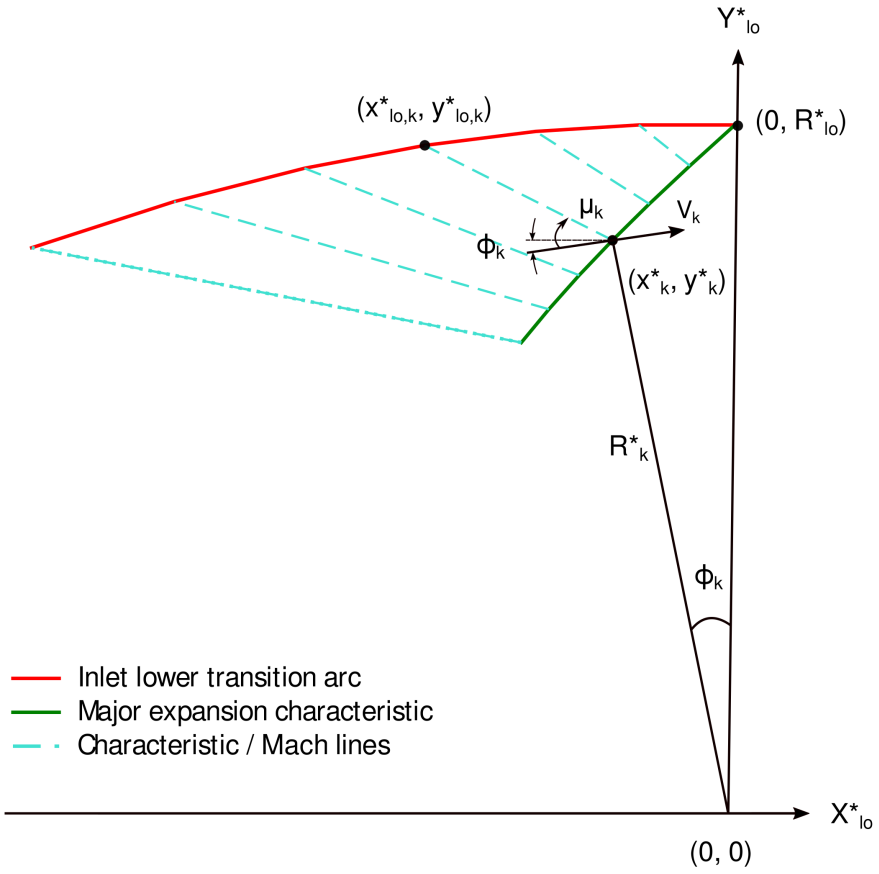

Figure 3.4: Lower transition arc

is also discretized in k number of segments responsible for the incremental flow turning by $\Delta\nu$. Hence, the flow direction ($\phi_{k,in}$) within any flow segment is expressed as

$$\phi_{k,in} = \nu_{in} - \nu_{lo} - (k-1)\Delta\nu, \tag{3.13}$$

where k is an integer in the range 1 < k < $\left[\frac{(\nu_{in}-\nu_{lo})}{\Delta\nu} + 1\right]$ with the flow direction varying from 0 at $k = \left[\frac{(\nu_{in}-\nu_{lo})}{\Delta\nu} + 1\right]$ to $(\nu_{in} - \nu_{lo})$ at $k = 1$. Substituting (3.13) into equation (3.12) and replacing $f(R^*_{lo})$ using equations (3.3) & (3.11) leads to the expression (3.14) which relates dimensionless radius (R^*) with the ($\Delta\nu$):

$$f(R^*_{k,in}) = 2\nu_{in} - 2(k-1)\Delta\nu - \frac{\pi}{2}\left(\sqrt{\frac{\gamma+1}{\gamma-1}} - 1\right). \tag{3.14}$$

The value of $R^*_{k,in}$ can be determined by simultaneous solution of equations (3.11) & (3.14) using an iterative procedure. As the value of k declines, $R^*_{k,in}$ also decreases and at $k = \left[\frac{(\nu_{in}-\nu_{lo})}{\Delta\nu} + 1\right]$, $R^*_{k,in} = R^*_{lo}$. With all the values of $R^*_{k,in}$ & $\phi_{k,in}$ determined for all segments, the coordinates x^* & y^* along the major expansion characteristic are calculated using

$$x^*_{k,in} = -R^*_{k,in}\sin(\phi_{k,in}), \tag{3.15}$$

$$y^*_{k,in} = R^*_{k,in}\cos(\phi_{k,in}). \tag{3.16}$$

These coordinates also lie on the straight characteristic lines between the major expansion characteristic & the lower transition arc. These characteristic lines are basically the Mach lines if we look closely in

the illustration 3.4. Two lines emanating from these coordinates form a Mach cone wherein the Mach lines are inclined on the velocity direction by Mach angle (μ), which is expressed as

$$\mu_{k,in} = -\sin^{-1}\left(\frac{1}{M_{k,in}}\right) \tag{3.17}$$

Now the equation describing these Mach lines can be determined once their slopes are established. It can be easily seen that these lines make an angle of ($\phi_k + \mu_k$) with respect to X^*_{lo} axis. Therefore, the slope of the Mach lines ($m_{k,in}$) can be found at mean Mach angle and the mean flow angle using

$$m_{k,in} = \tan\left\{\frac{(\phi_{k,in} + \phi_{k+1,in})}{2} + \frac{(\mu_{k,in} + \mu_{k+1,in})}{2}\right\}, \tag{3.18}$$

where μ is the Mach angle expressed in terms of critical radius (R^*) using equations (3.3) & (3.4), a new relation for μ is generated:

$$\mu_{k,in} = -\sin^{-1}\left\{\sqrt{\left(\frac{\gamma+1}{2}\right)R^{*2}_{k,in} - \left(\frac{\gamma-1}{2}\right)}\right\}. \tag{3.19}$$

Consequently, the Mach line can be described by a simple straight line equation

$$y^* = m_{k,in}(x^* - x^*_{k,in}) + y^*_{k,in}, \tag{3.20}$$

where $x^*_{k,in}$ & $y^*_{k,in}$ are the coordinates along the major expansion characteristic line.

On the other hand, the straight transition arc segments can be evaluated easily as they are parallel to the velocity direction (ϕ_k), thus the slope of these wall segments ($\bar{m}_{k,in}$) is given by

$$\bar{m}_{k,in} = \tan(\phi_{k+1,in}). \tag{3.21}$$

Subsequently, the equation of straight line transition arc segments is represented by

$$y^* = \bar{m}_{k,in}\left[x^* - (x^*_{lo})_{k+1,in}\right] + (y^*_{lo})_{k+1,in}, \tag{3.22}$$

where x^*_{lo} & y^*_{lo} are the lower transition arc coordinates. As mentioned earlier, the starting point of the transition arc is known at $(0, R^*_{lo})$, where $k = \left[\frac{(\nu_{in}-\nu_{lo})}{\Delta\nu} + 1\right]$. The rest of the points are computed by intersecting the Mach lines with wall segments starting at $k = \frac{(\nu_{in}-\nu_{lo})}{\Delta\nu}$ and gradually decreasing k until $k = 1$.

In the end, the resulting coordinates are rotated by angle $\alpha_{lo,in}$ described in equation (3.6) to accommodate the circular arc section in $X^* - Y^*$ coordinate system and get the final lower transition arc coordinates ($\mathcal{X}^*_{lo}, \mathcal{Y}^*_{lo}$) for the blade design as described by

$$(\mathcal{X}^*_{lo})_{k,in} = (x^*_{lo})_{k,in}\cos(\alpha_{lo,in}) - (y^*_{lo})_{k,in}\sin(\alpha_{lo,in}), \tag{3.23}$$

$$(\mathcal{Y}^*_{lo})_{k,in} = (x^*_{lo})_{k,in}\sin(\alpha_{lo,in}) - (y^*_{lo})_{k,in}\cos(\alpha_{lo,in}). \tag{3.24}$$

The procedure to get the upper transition arc is analogous to the lower arc. Similar to the lower transition arc, the upper transition arc also has inlet & outlet sections, only one of which should be calculated for ease. All of the equations involved in the calculation procedure are similar to the lower transition arc and hence not repeated here. The only difference is in the range of number of arc segments represented here by j, $\left(1 < j < \frac{\nu_{up}-\nu_{in}}{\Delta\nu}\right)$ and the use of major vortex-compression characteristic line. The figure 3.5 shows the nomenclature involved in the upper transition arc and figuratively represents the differences from the lower transition arc.

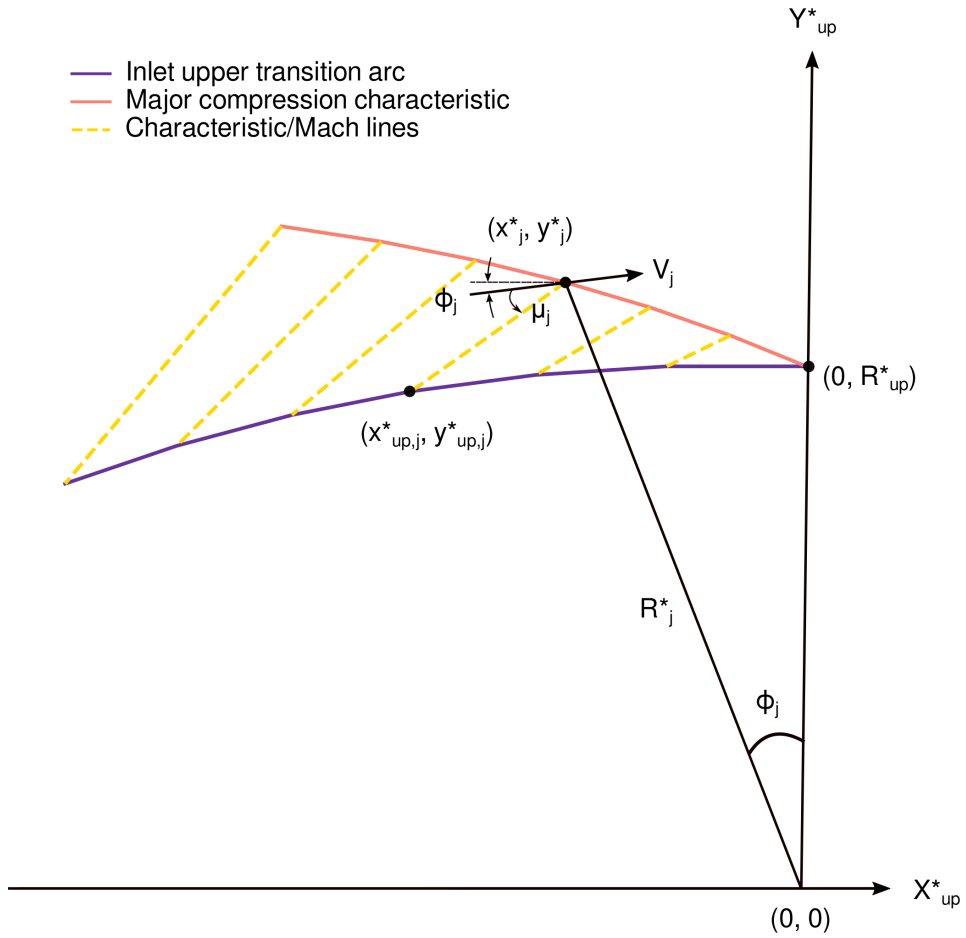

Figure 3.5: Upper transition arc

In the end, the outlet of the blade is designed by simply reversing the procedure to achieve the uniform outlet Mach number (M_{out}). In case of an impulse blade, the resulting blade is symmetric having ($\nu_{in} = \nu_{out}$) & ($\beta_{in} = \beta_{out}$). After generating the coordinates of the entire lower (pressure side) & upper (suction side) arc, the blade spacing/non-dimensional pitch (G^*) can be calculated using the end points of the transition arcs as shown in the figure 3.6. The remainder of the blade is completed with straight line sections parallel to the incoming & outgoing flow at the blade inlet & outlet respectively.

The aforementioned design methodology for perfect gas, is implemented in PYTHON as a part of this thesis work to obtain the 'Boxer tool' for generating supersonic axial rotor geometries for user-defined Mach numbers on the inlet, outlet, lower & upper circular arcs and inlet flow angles. It is also capable of yielding a reaction blade geometry if the Mach number at the outlet is not equal to the inlet one. However, the main focus will be the impulse blade geometry in the rest of the thesis work.

The dependency of this methodology on the Prandtl-Meyer angles to obtain the transition arcs is apparent. Since the Prandtl-Meyer angles cannot incorporate the effects of external forces, their use should be avoided and a new way to account for the forces needs to be devised. This idea is explored in the next section by generating new compatibility equations from the governing equations and solving it with MOC. Using this modified methodology, the supersonic axial rotor blades are designed without considering the body forces in the next section.

3.2. Modified Supersonic Axial Rotor Design Methodology

In this section, the dependence of the axial rotor's design methodology on the Prandtl-Meyer angles is eliminated. First, the procedure to derive the characteristic & compatibility equations, from the governing equations, is described. From the foregoing discussion it is established that the precise

determination of the curvature of transition arcs is of utmost importance to obtain the desired vortex-type velocity distribution. The compatibility equation is solved along the characteristic lines using MOC to generate the transition arc of the supersonic axial rotor blade for perfect gases. Lastly, the process to include the Dense gas effects in the design procedure is elaborated.

3.2.1. Governing Equations

The governing equations for 2D steady inviscid irrotational supersonic flow of compressible fluid with no external body forces had already been derived in 2.2.1. Since we are considering a planar design of the blade geometry, the flow equations namely, the *2D Gas dynamics* equation (2.16) and the *irrotationality* (2.14) relation are repeated hereunder in x-y plane for convenience,

Gas Dynamics Equation

$$(u^2 - a^2)u_x + (v^2 - a^2)v_y + 2uvu_y = 0,$$

Irrotationality condition

$$u_y - v_x = 0,$$

where u & v are the flow velocities in x & y direction respectively, a is the sound speed and the subscripts represent the first-order partial derivatives of the dependent variables in the respective directions.
The hyperbolic nature of Gas dynamics equation (2.16) for supersonic flows has been established in the previous chapter. Thus, the applicability of MOC is justified. Let us derive the required characteristic and compatibility equations corresponding to the two aforementioned governing partial differential equations in the next section.

3.2.2. Characteristic & Compatibility Equations

The method of characteristics solves the hyperbolic PDE by deriving a characteristic equation, which defines the slope of the characteristic curve (Mach wave in supersonic flows). In addition, a compatibility equation valid only along its respective characteristic line is also derived. It should be recalled that, this equation is a reduced total differential version of the governing hyperbolic PDE.

The derivation of characteristic and compatibility equations is explained extensively in *Gas dynamics by Zucrow & Hoffman*[30]. In the current section, the same derivation is briefly explained to solve the gas dynamics equation (2.16) & the irrotationality condition (2.14) simultaneously, ultimately yielding the characteristic equation & the compatibility equation. The procedure to solve equations (2.16) & (2.14) simultaneously, initiates by multiplying these two equations with two unknown parameters σ_1 & σ_2, respectively and adding them to obtain:

$$\sigma_1[2.16] + \sigma_2[2.14] = 0,$$
$$\sigma_1\big[(u^2 - a^2)u_x + (v^2 - a^2)v_y + 2uvu_y\big] + \sigma_2\big[u_y - v_x\big] = 0,$$
$$u_x\big[\sigma_1(u^2 - a^2)\big] + u_y\big[\sigma_1(2uv) + \sigma_2\big] + v_x\big[-\sigma_2\big] + v_y\big[\sigma_1(v^2 - a^2)\big] = 0. \tag{3.25}$$

The dependent variables $u(x, y)$ & $v(x, y)$ in the governing equations are assumed to be continuous functions. Therefore, MOC cannot solve the shock waves as they induce discontinuity in the dependent variables. The variables $u(x, y)$ & $v(x, y)$ can be expressed as total differentials as following:

For $u(x, y)$:

$$du = u_x dx + u_y dy$$
$$\frac{du}{dx} = u_x + \frac{dy}{dx}u_y \tag{3.26}$$

For $v(x, y)$:

$$dv = v_x dx + v_y dy$$
$$\frac{dv}{dx} = v_x + \frac{dy}{dx}v_y, \tag{3.27}$$

where $(dy/dx) = \lambda$ is assumed to be the slope of the characteristic curve. It can be observed in equations (3.26) & (3.27) that the coefficient infront of u_y & v_y is the slope of characteristic. Rearranging the terms in expression (3.25) in the form of total derivative yields

$$\sigma_1(u^2 - a^2)\left[u_x + \frac{\sigma_1(2uv) + \sigma_2}{\sigma_1(u^2 - a^2)}u_y\right] + (-\sigma_2)\left[v_x + \frac{\sigma_1(v^2 - a^2)}{-\sigma_2}v_y\right] = 0. \tag{3.28}$$

The terms inside the square brackets of equation (3.28) are analogous to the total differential of u & v. In accordance with equations (3.26) & (3.27), the characteristics corresponding to equation (3.28) have slopes (λ) equal to the coefficient of u_y & v_y, which gives

$$\lambda = \frac{\sigma_1(2uv) + \sigma_2}{\sigma_1(u^2 - a^2)}, \tag{3.29a}$$

$$\& \ \lambda = \frac{\sigma_1(v^2 - a^2)}{-\sigma_2}. \tag{3.29b}$$

These are the characteristic equations corresponding to equation (3.28). Now introducing equations (3.26), (3.27), & (3.29) in equation (3.28),

$$\sigma_1(u^2 - a^2)du - \sigma_2 dv = 0. \tag{3.30}$$

Equation (3.30) is the compatibility equation corresponding to the governing PDEs (2.16) & (2.14). It can be noted that the derived compatibility equation is a reduced total differential equation which is valid only if the slope of the characteristics is defined by (3.29).

In order to express λ in terms of the flow properties only, the unknown terms (σ_1 & σ_2) must be eliminated, therefore rearranging equations (3.29) in the following two forms:

$$\sigma_1\left[(u^2 - a^2)\lambda - 2uv\right] + \sigma_2(-1) = 0, \tag{3.31a}$$

$$\& \ \sigma_1(v^2 - a^2) + \sigma_2(\lambda) = 0. \tag{3.31b}$$

At first glance, the trivial solutions of σ_1 & σ_2 can be seen, $\sigma_1 = \sigma_2 = 0$. However, to find the non-trivial solution, the coefficients of σ_1 & σ_2 in the equation above must be zero, so rewriting them in matrix form,

$$\begin{bmatrix} \{(u^2 - a^2)\lambda - 2uv\} & -1 \\ (v^2 - a^2) & \lambda \end{bmatrix} = 0. \tag{3.32}$$

Expanding the determinant of matrix (3.32) and equating it to zero yields the following quadratic equation

$$(u^2 - a^2)\lambda^2 - 2uv\lambda + (v^2 - a^2) = 0. \tag{3.33}$$

The roots of this quadratic equation are the required solutions of λ given as

$$\lambda_{\pm} = \pm\left(\frac{dy}{dx}\right) = \frac{uv \pm a^2\sqrt{M^2 - 1}}{u^2 - a^2}. \tag{3.34}$$

Equation (3.34) is the desired *characteristic equation* in terms of the flow properties. It is clear in the equation above that two real roots are possible only for supersonic flows $(M > 1)$. For subsonic flows $(M > 1)$, imaginary solutions exist. This equation can be further simplified by expressing the flow velocities in terms of the magnitude (V), the flow angle (ϕ) and the Mach number in the form of Mach angle (μ) using the following trigonometric relations:

Flow velocities:

$$u = V cos\phi, \tag{3.35a}$$

$$v = V sin\phi \tag{3.35b}$$

Mach angle:

$$\mu = \sin^{-1}\left(\frac{1}{M}\right), \tag{3.36}$$

Flow angle:

$$\phi = \tan^{-1}\left(\frac{v}{u}\right). \tag{3.37}$$

Sunstituting these trigonometric expressions (3.35), (3.36) & (3.37) in the characteristic equation (3.34), the geometric form of the characteristic equation is obtained as,

$$\lambda_{\pm} = \tan(\phi \pm \mu). \tag{3.38}$$

The plus-minus sign represents two characteristic curves having positive (λ_+) & negative (λ_-) slopes originating from a point.

In a similar manner, the unknown terms σ_1 & σ_2 needs to be eliminated from the compatibility equation (3.30) to obtain a governing expression in terms of u & v. This is done by substituting the values of σ_2 from equations (3.31a) & (3.31b) one by one to yield two different forms of compatibility equations given by

$$(u^2 - a^2)du_{\pm} + \left[2uv - (u^2 - a^2)\lambda_{\pm}\right]dv_{\pm} = 0, \tag{3.39a}$$

$$\& \ (u^2 - a^2)du_{\pm} + \frac{(v^2 - a^2)}{\lambda_{\pm}}dv_{\pm} = 0. \tag{3.39b}$$

The equations above are different forms of the single *compatibility equation* valid along each of the characteristic lines. Consequently, the governing PDEs of 2D steady irrotational supersonic flow have been reduced to total differential equations (3.39). These equations are valid only if the slopes of characteristics are expressed by the equation (3.34).

3.3. Implementation of MOC for Transition Arcs

The Prandtl-Meyer function is the geometric representation of the compatibility equations (3.39b) derived in the previous section [30]. In order to avoid the usage of Prandtl-Meyer angles in the determination of transition arcs for supersonic rotor blade, the MOC is implemented directly on the compatibility equation (3.39b). In the following sections, MOC will be applied first for the perfect gas followed by the application for real gases in the dense gas region.

3.3.1. Transition Arc for Perfect Gas

The design methodology used in this section is adapted from the work of Bufi et al [23], where the design procedure of supersonic axial rotor blades for perfect gas flows was extended to dense gas flows. In the present thesis work, same ideology is adapted to eliminate the contribution of Prandtl-Meyer angles in the transition arc design for a perfect gas flow.

The process initiates by defining the inputs in the rotor's relative frame. The user defines the inlet & outlet relative Mach numbers (M_{in} & M_{out}), inlet & outlet relative flow angles (β_{in} & β_{out}), the lower Mach number (M_{lo}) at the lower/pressure circular arc and the upper Mach number (M_{up}) at the upper/suction circular arc. In order to account for the rotational speed of the rotor, the relative flow velocities & angles are supplied instead of absolute parameters. The upper & lower transition arcs are calculated in the unrotated upper & lower coordinate systems ($X^*_{up} - Y^*_{up}$) & ($X^*_{lo} - Y^*_{lo}$) respectively, as illustrated in figure 3.6.

For the sake of brevity, the following discussion is about designing the lower transition arc only, using the new method. The upper transition arc is also designed using the same technique. These arcs are composed of straight line segments designed in the opposite direction of flow, from the circular vortex region till the uniform parallel inlet flow region, to obtain the inlet flow conditions. With the user-defined Mach number on the lower circular arc (M_{lo}), the initial coordinate of the transition arc $(0, R^*_{lo})$ is obtained in the lower coordinate system ($X^*_{lo} - Y^*_{lo}$), using the critical velocity ratio $\left(M^*_{lo}(M_{lo})\right)$ equation (3.4), and the vortex equation $(M^*.R^* = 1)$ mentioned in the previous chapter.

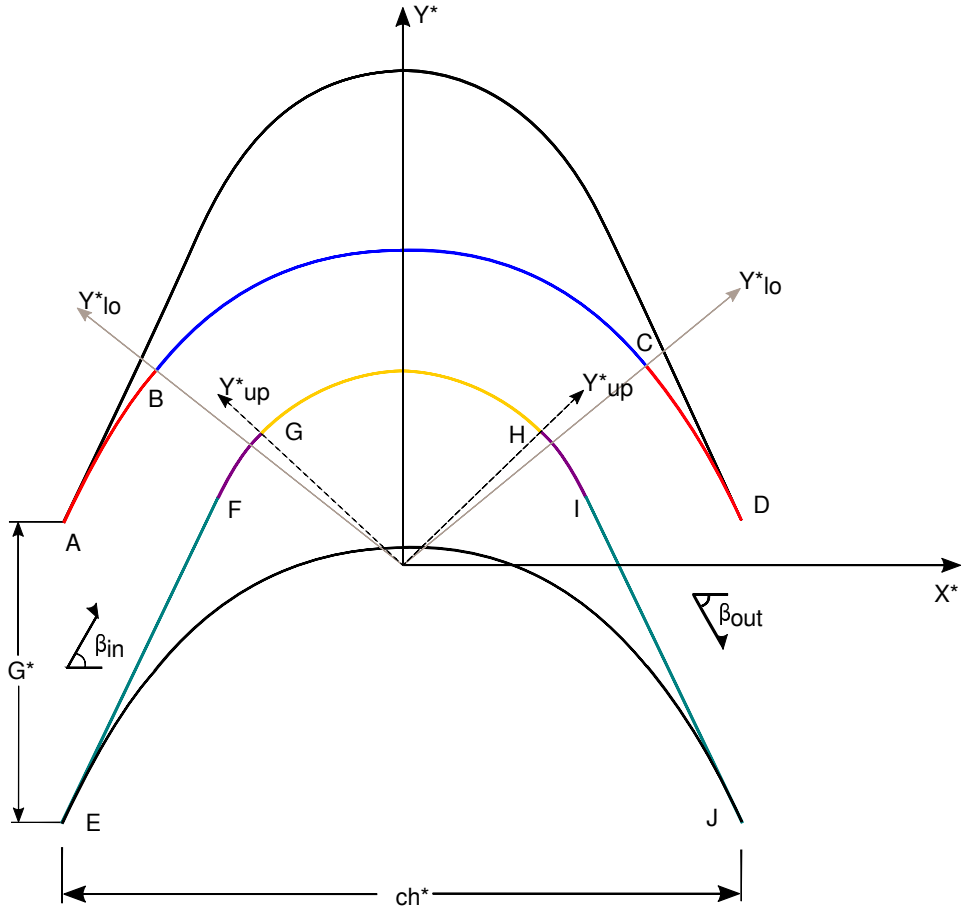

Figure 3.6: Supersonic axial rotor blade with upper & lower coordinate systems (AB is Inlet lower transition arc, BC is Lower circular arc, CD is Outlet lower transition arc, FG is Inlet upper transition arc, GH is Upper circular arc, HI is Outlet upper transition arc, EF is Inlet straight line & IJ is Outlet straight line)

The flow is horizontal at the starting point of the transition arc which gives $\phi_{lo} = 0$. The flow direction at the subsequent arc segment's points $(x^*_{lo,k}, y^*_{lo,k})$ is calculated by adding a small angle $\Delta\phi$ to the previous location. Furthermore, $(0, R^*_{lo})$ is also the starting point of the major vortex expansion characteristic line as shown in figure 3.4. Since the characteristic lines are Mach lines in a supersonic flow, this major vortex-expansion characteristic line makes the Mach angle (μ_{lo}) at the initial point with the velocity vector given by:

$$\mu_{lo} = \sin^{-1}\left(\frac{1}{M_{lo}}\right). \tag{3.40}$$

The next coordinate along the major expansion characteristic is obtained by the intersection of two straight lines with slopes $\tan(\phi_k)$ and $\tan(\mu_{lo})$, respectively. With the coordinate of the new location on the major characteristic line known, the new critical radius (R^*_k) can be easily obtained and the corresponding critical velocity ratio at the new point is evaluated with $M^*_k = 1/R^*_k$. The Mach number at the new point (M_k) is calculated using its analytical relation with the critical velocity ratio expressed by equation (3.4). Similarly, all the coordinates are sequentially evaluated along the major expansion characteristic line until the inlet relative Mach number (M_{in}) is reached within the assigned tolerance. For instance, refer to figure 3.4, the design process starts at coordinate $(0, R^*_{lo})$ at Y^*_{lo} axis. The next coordinate on the major expansion characteristic is calculated in the left direction and M_k is found at this new location. This process is continued from right to left direction until M_{in} is reached on the major expansion characteristic.

The points along the lower transition arc $(x^*_{lo,k}, y^*_{lo,k})$ are calculated by intersecting the straight line segments of the arc with the characteristic lines emanating from the points on the major expansion

$P_{o,r}$	$T_{o,r}$	$R\ [J/kgK]$	γ	Z	M_{lo}	M_{in}	M_{up}	β_{in}
0.05	1.2	90.24	1.04	0.99	2.0	2.5	3.0	65^o

Table 3.1: Blade design parameters for Toluene in diluted gas region (far from the saturation curve & the critical point)

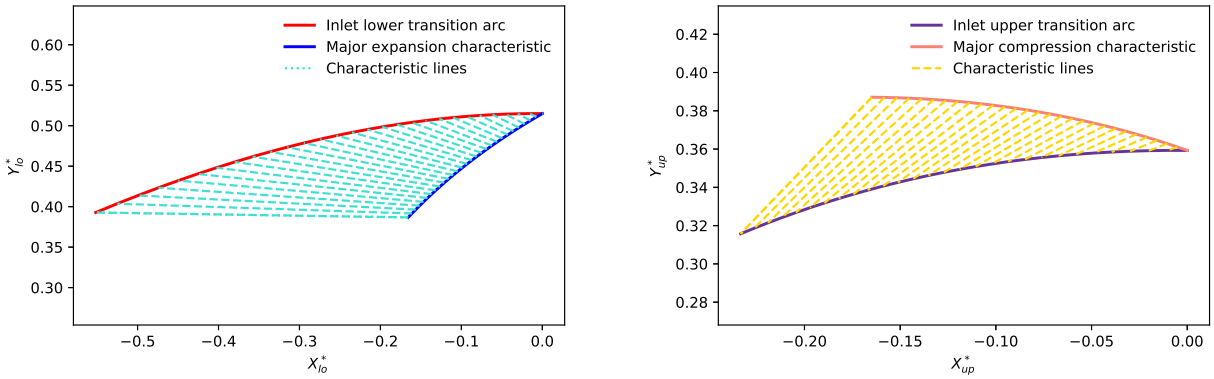

(a) Lower transition arc

(b) Upper transition arc

Figure 3.7: Transition arcs designed for Toluene at ideal operating conditions using the COMOC tool with ideal EOS

characteristic as depicted in figure 3.4. At each point, these characteristic lines along with the corresponding segments of the major-expansion characteristic line are part of the Mach cone. Hence, the characteristic lines are also inclined at Mach angle (μ_k) with the velocity flow direction but with an opposite sign than that of the segments along the major characteristic line. The figure 3.7(a) illustrates the lower transition arc at the blade's inlet in $X^*_{lo} - Y^*_{lo}$ frame, created with the procedure described above for *Toluene* as working fluid using perfect gas EOS as shown in table 3.1.

The total pressure (P_o) and temperature (T_o) represented in table 3.1 are in reduced form $(P_{o,r}, T_{o,r})$ i.e., normalized with the critical pressure and temperature of Toluene, to represent the operating point's proximity to Toluene's upper vapour-liquid saturation curve. $P_{o,r}$ & $T_{o,r}$ are selected such that the operating point is far away from the saturation curve, where ideal gas law is valid. This is confirmed by the value of compressibility factor (Z) being close to 1.

In a similar manner, the same procedure is repeated for the upper transition arc starting from $(0, R^*_{up})$. In this case, major vortex-compression characteristic line is used to obtain the upper transition arc. The segments along this characteristic make the Mach angle (μ_j) of opposite sign than that made by the major expansion characteristic. The rest of the design strategy is analogous to that of the lower transition arc. The illustration of upper transition arc at the rotor's inlet in $X^*_{up} - Y^*_{up}$ reference frame, designed for the same conditions mentioned in the table 3.1, is given in figure 3.7(b).

3.3.2. Transition Arc for Real Gas

In case of a real gas, the ideal gas laws are not applicable due to the complex/non-ideal behaviour of the gases. Therefore, the analytical relations of critical velocity ratio (M^*) (3.4) and the speed of sound $(a = \sqrt{\gamma RT})$ are not valid. This follows the need to circumvent the non-availability of valid analytical relations of M^* & a in the dense gas region. It is done by introducing an iterative procedure coupled with the thermophysical data from the *CoolProp* library [14]. The flow chart illustrating the said iterative procedure is given in figure 3.8. To keep the discussion concise, only lower transition arc is designed in this section.

The iterative procedure begins with the user-defined total pressure & temperature, the desired

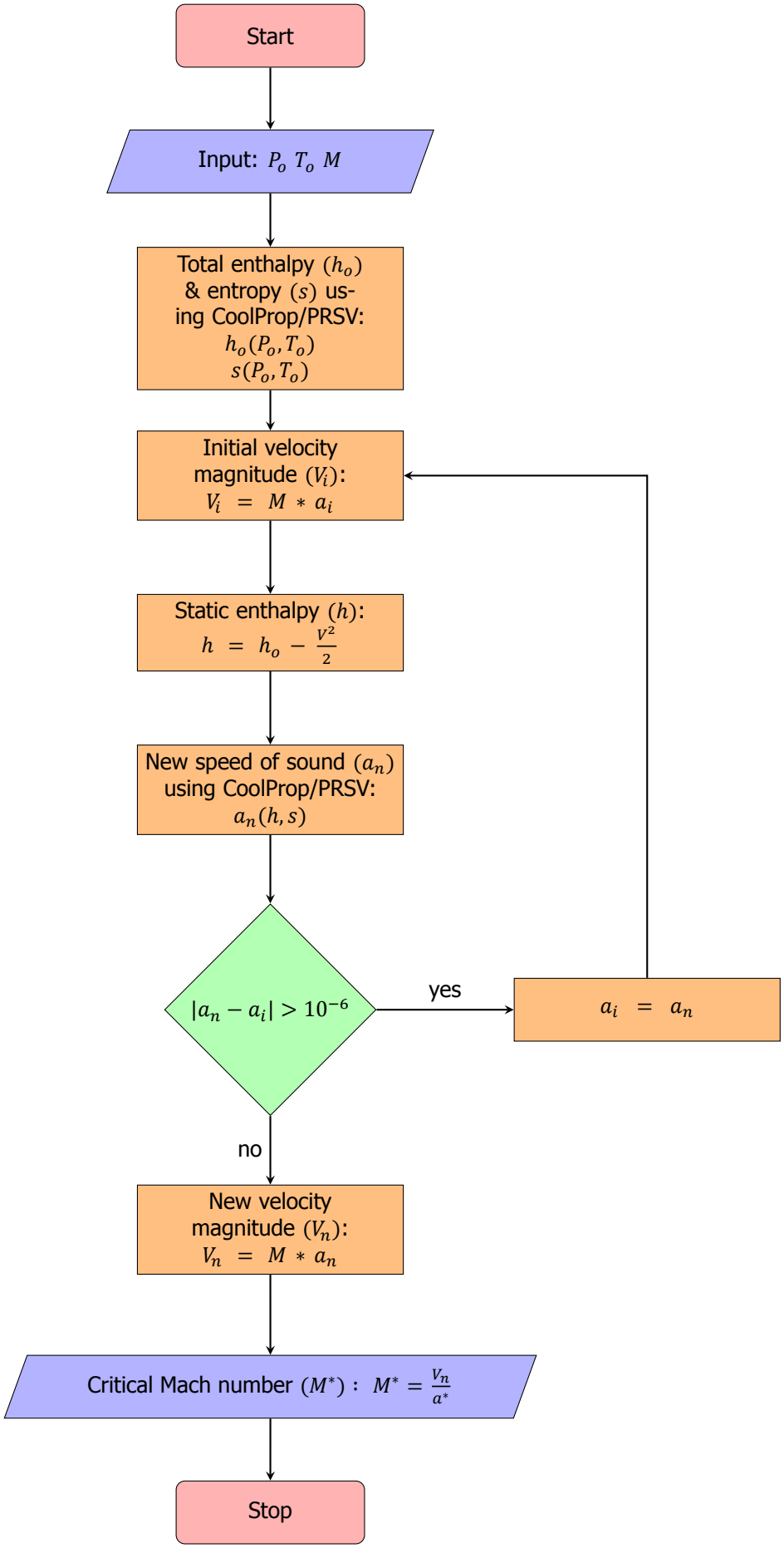

Figure 3.8: Iterative procedure to calculate M^* in Dense gas case

$P_{o,r}$	$T_{0,r}$	Z	M_{lo}	M_{in}	M_{up}	β_{in}
1.05	1.05	0.57	2.0	2.5	3.0	65^o

Table 3.2: Blade design parameters for Toluene as working fluid in dense gas region (close to the saturation curve)

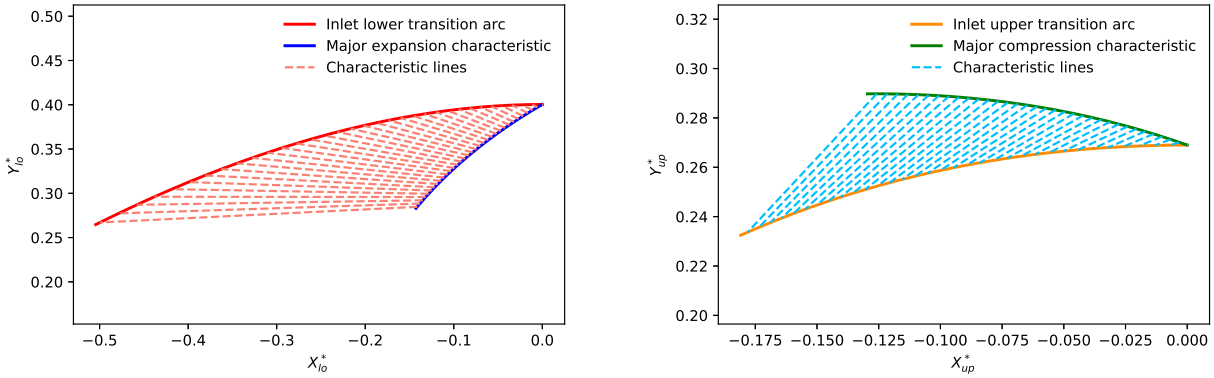

(a) Lower transition arc

(b) Upper transition arc

Figure 3.9: Transition arcs designed for Toluene at operating conditions in dense gas regime using the COMOC tool with real EOS

relative Mach number whose critical velocity ratio is to be determined. An initial guess of sound speed is provided to initialize the iteration. Following the steps in figure 3.8 to generate a new speed of sound (a_n). This procedure is repeated until the new sound speed has converged with in an assigned tolerance limit. The new velocity magnitude thus yielded is later divided by the critical speed of sound (a^*) to give the required critical velocity ratio. The critical speed of sound is defined at sonic Mach number $(M = 1)$ and it is also calculated iteratively in a similar fashion as critical velocity ratio.

With a procedure to define critical velocity ratio for real gases operating in the dense gas regime, critical velocity ratio at the lower circular arc (M^*_{lo}) can be obtained by supplying M_{lo}. The position of the first point on the lower transition arc in the lower reference frame, $X^*_{lo} - Y^*_{lo}$ is $(0, R^*_{lo})$, where $R^*_{lo} = 1/M^*_{lo}$. From this point on, the rest of the procedure to generate the lower transition arc is similar to that of a perfect gas. To keep the discussion concise, the procedure is not repeated here. The only difference is in the calculation of critical velocity ratio (M^*_k) along the major vortex-expansion characteristic. Instead of using the analytical relation, the iterative procedure described in figure 3.8 is implemented all along the design methodology.

The inlet lower & upper transition arcs designed for the real gases working at operating conditions close to their upper saturation curves is shown in figures 3.9(a) & 3.9(b). The operating conditions chosen for this case are mentioned in the table 3.2. Toluene is kept as the working fluid. However, $P_{o,r}$ & $T_{o,r}$ are opted to be in vicinity of Toluene's critical point to incorporate the dense gas effects in transition arcs' geometry.

The compressibility factor (Z) in the the table 3.2 is well below 1 confirming the dominance of non-classical gas behaviour at the chosen operating point. The resulting transition arcs with the proper consideration of real gas effects are given below.

3.4. Blade Generation

The remainder of the blade is generated in a similar manner for both the cases of perfect & dense gases. The resulting inlet upper & lower transition arcs are rotated in $(X^* - Y^*)$ system by angle $\alpha_{up,in}$ & $\alpha_{lo,in}$ respectively. These angles represent the amount of flow turning induced by the upper & lower circular arcs at the inlet. In the section 3.1, these angles are expressed by equations (3.6), however

they depend on Prandtl-Meyer angles and hence, cannot be used in the current case so here these angles are defined as:

$$\alpha_{up,in} = \beta_{in} - \phi_{k,up}, \tag{3.41a}$$

$$\alpha_{lo,in} = \beta_{in} - \phi_{k,lo}, \tag{3.41b}$$

where β_{in} is the inlet relative flow angle, $\phi_{k,up}$ & $\phi_{k,lo}$ are the flow angles at the inlet of upper & lower transition arcs respectively, obtained after the transition arcs are generated. The angles in counter-clockwise direction are considered positive.

After the rotation, the upper & lower circular arcs are added to the geometry making the circular section of the blade geometry. It is followed by the translation of resulting arcs by the non-dimensional pitch (G^*) as shown in figure 3.6. Finally, the straight line sections parallel to the inflow direction are added to close off the blades. The said procedure is implemented in PYTHON to develop 'COMOC tool' to generate supersonic axial rotor blades as a part of this work.

In the case of symmetric rotor blades, we have $M_{in} = M_{out}$ and $\beta_{in} = \beta_{out}$. This means that the geometry generated at the inlet is symmetrical, thereby yielding a complete 2D supersonic impulse rotor blade for axial turbines. The design tool COMOC can also calculate an asymmetric rotor geometry with varying degrees of reaction, if the user defines $M_{in} \neq M_{out}$ and $\beta_{in} \neq \beta_{out}$. However, in the current work the degree of reaction is set to zero to generate only symmetric/impulse supersonic blades. It should be noted that the rotor geometries generated in this thesis work, have sharp leading & trailing edges, which does not have enough mechanical strength. These edges can be rounded off by giving them a blunted edge as detailed out in Bufi et al's work [23]. However, the blunting of the leading edge leads to a standing shock wave that interrupts the flow passage, can make the rotor un-started and disrupts the stator's outlet flow conditions. These aspects are out of the scope of this thesis work.

A comparison between the rotor geometries created for toluene as working fluid using two gas models at different working conditions is conducted in the figure 3.10(a). First the geometry is generated for the operating conditions in the ideal gas region i.e., low pressure and high temperatures and then for the conditions closer to the saturation curve to study the non-ideal effects on the rotor shape. The dense gas operating conditions are mentioned in the table 3.2. The increased channel area can be observed in the case of dense conditions which means a greater inlet-to-throat/exit-to-throat area ratio with respect to the perfect gas case. This behaviour can be explained based on the fundamental derivative of gas dynamics (Γ) in the general equation for quasi-one-dimensional flow[10] expressed as

$$\frac{dM}{dx} = \frac{1 + (\Gamma - 1)M^2}{M^2 - 1} \frac{M}{A} \frac{dA}{dx}. \tag{3.42}$$

For the operating conditions close to the saturation curve, $\Gamma < 1$ for dense gas, then the value of dM/dx in equation (3.42) is smaller if compared with the case of perfect gas, where Γ is a constant and always greater than 1. This leads to the slower transition to the desired Mach number and it is done by further expanding the flow than in the case of perfect gas. Furthermore, in dense gas region, the speed of sound increases with isentropic expansion which makes it harder to reach the target Mach number.

In figure 3.10(b) the rotor blades are generated at perfect gas conditions using the perfect gas algorithm and at diluted conditions using the dense gas algorithm. In this case the two geometries are overlapping each other. This result builds confidence in the dense gas algorithm as it can recreate the perfect gas rotor geometry in the diluted gas region. It should be noted here that the terms diluted gas & perfect gas are used interchangeably. This simply means that for conditions far away from the saturation curve, the ideal gas laws are valid and the gas can be treated as a perfect gas.

The design tool COMOC & the Boxer tool are equipped with the ability to yield a supersonic axial rotor geometry in the dense gas region along with the perfect gas. With the ability to generate blades in the dense gas region, the Boxer tool is now called "Boxer-Bufi tool". In the modified design methodology, the need to use Prandtl-Meyer angles is circumvented. This entails a flexibility in COMOC tool to add external body forces to the governing equations. This privilege is not possible in the Boxer-Bufi tool.

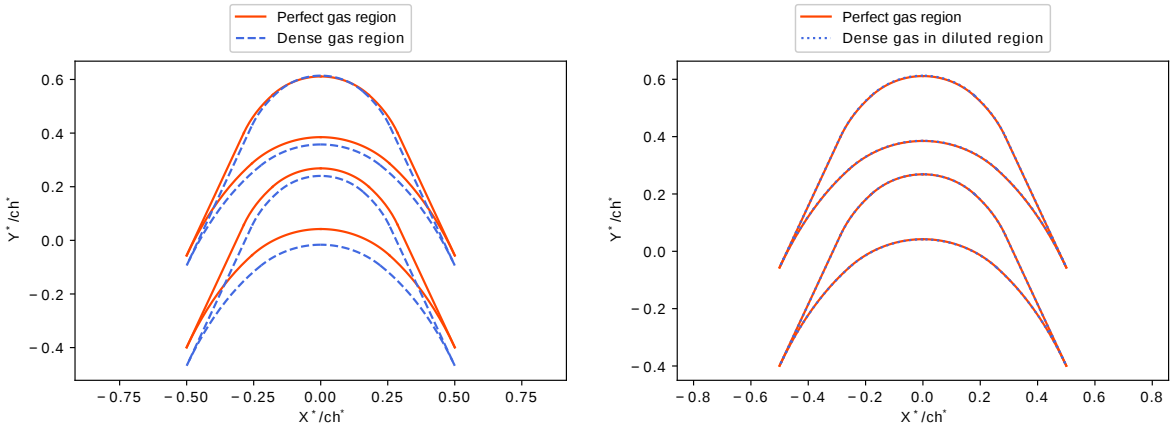

Figure 3.10: Comparison between rotor geometries designed at (a) operating point in perfect gas region and dense gas region (b) the same operating point in perfect gas region using perfect gas & dense gas model

4

Supersonic Radial Rotor Blade Design

The compatibility equation along with the body force is derived in this chapter. The MOC is implemented on this new equation to generate the transition arc considering the body force's effect on its curvature. The arcs are generated for both perfect & dense gas regions. In the end, the whole blade is compared to the blade with no body force, to study the changes inflicted on the geometry.

This chapter introduces a novel design philosophy adopted to generate a supersonic rotor blade for radial turbines. This is a new way to generate a supersonic radial blade as most of the design methods are based on optimization of 1D mean-line methods which are not very efficient especially for supersonic flows. The lack of relevant literature makes this methodology challenging and the consideration of complex non-classical behaviour of organic fluids adds up to the difficulty. Therefore, the final supersonic radial rotor is not generated in this work but a base case is explained and the resulting geometry is analyzed.

As established in the previous chapter, the 2D gas dynamics equation (2.16) is the governing equation used to design supersonic axial blade. This was done in the axial rotor's reference frame where, the fluid flows axially and the radial forces due to the rotation of the rotor are balanced by the pressure gradients in the radial direction (radial equilibrium). However, in case of a radial turbine the fluid flows radially inward or outward. In the rotating reference frame of the radial runner, the fluid flow is affected by the pseudo forces. The idea in this chapter is to build up on the supersonic axial rotor design methodology by including the fictitious forces in the governing equations of 2D steady isentropic supersonic compressible flow. These equations were derived in the section 2.2.1. It is followed by the determination of the new compatibility & characteristic equations which are used to obtain transition arcs for the supersonic radial rotor blade. A simple case of a constant body force acting in the negative x-direction is analyzed in this chapter. Its presence on the transition arc is considered. In the end, the supersonic rotor blade is generated for the operating point in both perfect gas and the dense gas region. The COMOC design tool is further enhanced with the capability to include the body forces in the design procedure of the transition arcs in both thermodynamic regions.

The fictitious forces experienced in any rotating frame of reference are the centrifugal & Coriolis forces. These forces are not present for an observer whose reference frame is not rotating. As shown in the figure 4.1, two different perspectives to observe the motion of the yellow ball are depicted. Referring to the motion of the ball, the deep yellow colored ball marks the initial point and the lighter yellow ball shows the final point. The red ball is stationary in both images. The left side image is seen in the inertial frame of reference, thus only centripetal force is experienced by the red ball and the yellow ball can be seen moving in a straight line in the direction of the imparted velocity. In the non-inertial/rotating frame of reference, the centrifugal force always acts radially away from the center of rotation. Whereas, the Coriolis force acts in the perpendicular direction to the velocity of an object moving in the rotating frame. This can be observed in the rotating frame of reference of the right side image wherein, the red ball experiences the centrifugal force radially away from the center and the path

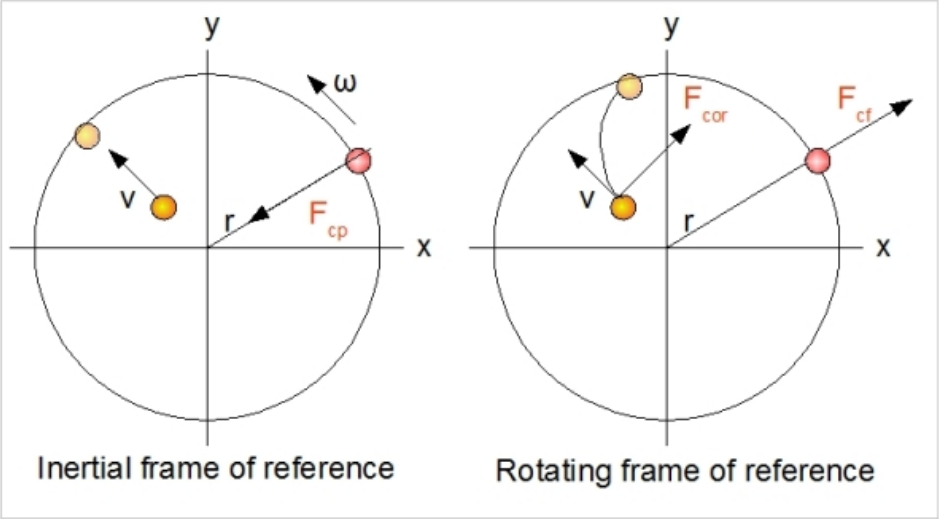

Figure 4.1: Centrifugal & Coriolis force representation in inertial & non-inertial reference frame [34]

of yellow ball appears to be curved because of the Coriolis force acting in the perpendicular direction of its velocity. Although these forces are not really present but due to the change of observational frame, the motion of yellow ball suggests the presence of forces that are responsible for its curved path.

4.1. Design Philosophy

The design ideology explored in this section is to extend the methodology of generating a supersonic axial rotor blade to obtain the rotor geometry for radial turbines. Due to the radial direction of flow and the forces, the radial rotor is envisaged to be generated. If the design calculations are performed in the rotating frame of the rotor and the effect of centrifugal & Coriolis force on the supersonic flow is accounted for in the early stages of the design. This entails the consideration of these pseudo forces in the design of rotor geometry ultimately yielding a rotor shape for radial turbines.

In order to do this, the governing equations must have the body force contribution as derived in the section 2.2.1. This is followed by the application of MOC procedure to obtain a new set of characteristic & compatibility equations, which can be further used to generate the transition arcs of the supersonic radial rotor.

4.1.1. New Characteristic & Compatibility Equations

The governing equations to describe the motion of a steady 2D irrotational supersonic isentropic compressible flow with external body forces is given by the *Gas dynamics* equation with body forces (2.15), which is repeated hereunder in cartesian coordinates for convenience,

$$(u^2 - a^2)u_x + (v^2 - a^2)v_y + 2uvu_y - uF_{Bx} - vF_{By} = 0.$$

The hyperbolic governing equation (2.15) and the irrotationality condition (2.14) are solved simultaneously to obtain the characteristic & compatibility equation in an analogous manner as discussed in the section 3.2.2. To keep the discussion concise the whole derivation procedure is not repeated here.

Since the presence of body forces in the gas dynamics equation is the only difference, the compatibility equation (4.1) yielded after the derivation in this case, has an added contribution of body forces in comparison with the compatibility equation (3.39) derived in the section 3.2.2. The rest of the terms in this equation are similar to those in the compatibility equation without the body force.

$$(u^2 - a^2)du_{\pm} + \frac{(v^2 - a^2)}{\lambda_{\pm}}dv_{\pm} - (uF_{Bx} + vF_{By})dx_{\pm} = 0. \tag{4.1}$$

The characteristic equation obtained in this case is not influenced by the presence of the body forces because during the derivation of characteristic equation in the case of body forces, the terms responsible for the characteristic equation remain the same as in equation (3.28). Hence, the characteristic equation in this case is the same as the equation (3.34) derived in the section 3.2.2, which is repeated here for convenience:

$$\lambda_{\pm} = \pm\left(\frac{dy}{dx}\right) = \frac{uv \pm a^2\sqrt{M^2-1}}{u^2-a^2}.$$

To implement the compatibility equation in the MOC procedure to generate the transition arcs, it needs to be represented in a different form in terms of the velocity magnitude (V), flow angle (ϕ) & Mach angle (μ). Let us first substitute the term $dx_{\pm}$ in equation (4.1) with the definition of the slope of a characteristic line, $\lambda_{\pm} = (dy/dx)_{\pm}$ and rearranging the resulting equation yields

$$\left(\frac{dv}{du}\right)_{\pm} = -\lambda_{\pm}\left(\frac{u^2-a^2}{v^2-a^2}\right) + \left(\frac{uF_{Bx}+vF_{By}}{v^2-a^2}\right)\left(\frac{dy}{du}\right)_{\pm}. \tag{4.2}$$

Substituting the characteristic equation (3.34) into the equation (4.2) to yield yet another form of the compatibility equation expressed as

$$\left(\frac{dv}{du}\right)_{\pm} = \frac{uv \pm a^2\sqrt{M^2-1}}{a^2-v^2} + \left(\frac{uF_{Bx}+vF_{By}}{v^2-a^2}\right)\left(\frac{dy}{du}\right)_{\pm}. \tag{4.3}$$

An alternate form of this compatibility equation in terms of V, ϕ & μ using the trigonometric relations (3.35), (3.36) & (3.37) can be derived. Introducing these relations in the LHS of equation (4.3) yields

$$\begin{aligned}\left(\frac{dv}{du}\right)_{\pm} &= \left(\frac{V\cos\phi d\phi + \sin\phi dV}{-V\sin\phi d\phi + \cos\phi dV}\right)_{\pm} \\ &= \frac{\cos\phi + \sin\phi\left(\frac{dV}{Vd\phi}\right)_{\pm}}{-\sin\phi + \cos\phi\left(\frac{dV}{Vd\phi}\right)_{\pm}} \\ &= \frac{1+\chi_{\pm}\tan\phi}{\chi_{\pm}-\tan\phi},\end{aligned} \tag{4.4}$$

where $\chi_{\pm} = \left(\frac{dV}{Vd\phi}\right)_{\pm}$ for convenience. Now substituting the trigonometric relations (3.35), (3.36) & (3.37) in the first term on the RHS of equation (4.3), gives

$$\begin{aligned}\frac{uv \pm a^2\sqrt{M^2-1}}{a^2-v^2} &= \frac{V^2\sin\phi\cos\phi \pm a^2\sqrt{M^2-1}}{a^2-V^2\sin^2\phi} \\ &= \frac{\sin\phi\cos\phi \pm \left(\frac{1}{M^2}\right)\sqrt{M^2-1}}{\left(\frac{1}{M^2}\right)-V^2\sin^2\phi} \\ &= \frac{\sin\phi\cos\phi \pm \sin\mu\cos\mu}{\sin^2\mu-\sin^2\phi}.\end{aligned}$$

Using the standard trigonometric relations in the equation above and rearranging simplifies this term to

$$\frac{uv \pm a^2\sqrt{M^2-1}}{a^2-v^2} = \pm\cot(\mu \mp \phi). \tag{4.5}$$

Finally, the second term on the RHS of equation (4.3) can be written as

$$\begin{aligned}\left(\frac{uF_{Bx}+vF_{By}}{v^2-a^2}\right)\left(\frac{dy}{du}\right)_{\pm} &= \frac{V(F_{Bx}\cos\phi + F_{By}\sin\phi)dy_{\pm}}{(V^2\sin^2\phi - a^2)(-V\sin\phi d\phi_{\pm} + \cos\phi dV_{\pm})} \\ &= \frac{(F_{Bx}\cos\phi + F_{By}\sin\phi)}{V^2\cos\phi(\sin^2\phi-\sin^2\mu)(\chi_{\pm}-\tan\phi)}\left(\frac{dy}{d\phi}\right)_{\pm}.\end{aligned} \tag{4.6}$$

Putting equations (4.4), (4.5) & (4.6) together yields the whole expression, which is given as

$$\left(\frac{1+\chi_{\pm}\tan\phi}{\chi_{\pm}-\tan\phi}\right)=\pm\cot\left(\mu\mp\phi\right)+\frac{\left(F_{Bx}\cos\phi+F_{By}\sin\phi\right)}{V^2\cos\phi(\sin^2\phi-\sin^2\mu)(\chi_{\pm}-\tan\phi)}\left(\frac{dy}{d\phi}\right)_{\pm}. \tag{4.7}$$

Rearranging the equation above with trigonometric equations finally results in the sought after alternative form of the compatibility equation,

$$\frac{1}{V}\left(\frac{dV}{d\phi}\right)=\pm\tan\mu+\frac{F_{Bx}\cos\phi+F_{By}\sin\phi}{V^2\cos\mu\sin\left(\phi\pm\mu\right)}\left(\frac{dy}{d\phi}\right)_{\pm}. \tag{4.8}$$

The second term on the RHS of the expression (4.8) represents the body forces' contribution. Without this second term in the equation, the governing equation of the Prandtl-Meyer function is obtained, which can be used to derive the Prandtl-Meyer angles. In this section, we will use equation (4.8) to implement MOC in order to generate the transition arcs with body forces.

$$\left(\frac{dV}{d\phi}\right)=\pm V\tan\mu. \tag{4.9}$$

The new trigonometric form of compatibility equation (4.8) is valid only along the characteristic lines defined by the trigonometric form of the characteristic equation (3.38) $\left[\lambda_{\pm}=\tan\left(\phi\pm\mu\right)\right]$. The plus-minus sign in these equations represent the equations valid along two characteristic lines. These equations are implemented in the next section to generate the desired transition arcs with the external forces acting on them.

4.2. Implementation of MOC for Transition Arcs with Body Forces

The procedure to generate the transition arcs with body forces involves the use of compatibility equation (4.8) along with the slope of characteristic line (3.38). The discretized form of the compatibility equation (4.8) is implemented along the characteristic lines. This discretized form is obtained by applying the finite difference method (Euler explicit), replacing the differentials dV, dy & $d\phi$ by the differences ΔV, Δy & $\Delta\phi$ respectively. These differences are between the initial and the next spatial point. However, the other parameters in the equation are calculated at the initial point. The difference $\Delta\phi$ is the step size and is given a small value to get a better approximation. The discretized equation is given by equation (4.10). To keep the discussion concise, only inlet side transition arc's design process is discussed in this section.

$$\Delta V_{\pm}=\pm V\tan\mu(\Delta\phi)_{\pm}+\left(\frac{F_{Bx}\cos\phi+F_{By}\sin\phi}{V\cos\mu\sin\left(\phi\pm\mu\right)}\right)\Delta y_{\pm} \tag{4.10}$$

Assuming a user defined value of $\Delta\phi$ and the body force, the transition arc calculation procedure using the discretized compatibility equation (4.10) is enumerated below (referring to figure 4.2):

1. The design procedure starts from the known coordinate $(0, R^*_{lo})$ on the major-expansion characteristic line. Since the lower Mach number (M_{lo}) is user defined on the lower circular arc, the flow velocity at this point is known.

2. The next coordinate on the major-expansion characteristic line (x^*_2, y^*_2) (assuming $k=2$ for this point) is determined by the intersection of straight line segment of expansion characteristic with slope $[\tan\left(\mu_1-\phi_1\right)]$ & the straight line from the origin $(0,0)$ with slope $[\tan\phi_2]$, where $\mu_1=\mu_{lo}$, $\phi_1=0$ (horizontal flow at $k=0$) & $\phi_2=\Delta\phi$.

3. The velocity (V_2) at this second coordinate is calculated using the discretized equation (4.10) knowing the values of other parameters at the previous location. The new Mach number (M_2) at this location can be now be figured out with this velocity.

4. Similarly the next coordinate (x^*_k, y^*_k) along the major-expansion characteristic is calculated by intersecting the straight line segments of slope $[\tan\left(\mu_{k-1}-\phi_{k-1}\right)]$ with the straight line of slope $[\tan\phi_k]$, where $\phi_k=k.\Delta\phi$. Then the velocity (V_k) & the Mach number (M_k) can be determined at this location.

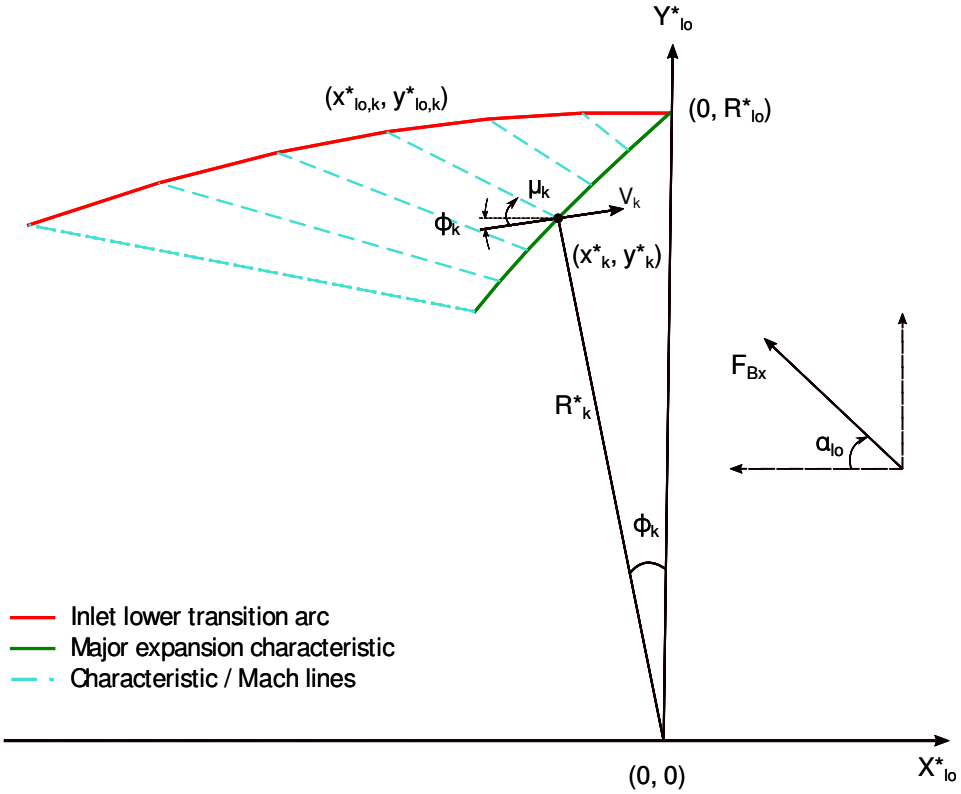

Figure 4.2: Lower transition arc description in the presence of an external body force

$N\ [RPM]$	$R_o\ [mm]$	$R_i\ [mm]$	$F_{c,o}\ [m/s^2]$	$F_{c,i}\ [m/s^2]$
25500	113	90	8.0×10^5	6.4×10^5

Table 4.1: The general dimensions of a radial-inflow runner and the centrifugal forces (N is the rotational speed of the radial-inflow runner in revolutions per minute, $F_{c,o}$ & $F_{c,i}$ are the centrifugal forces per unit mass at the outer (R_o) & inner (R_i) radius of the runner)

5. This process is repeated until the inlet relative Mach number is reached $(M_k = M_{in})$. Finally resulting in the major-expansion characteristic line.

Once the major-expansion characteristic is determined, the lower transition arc is calculated in an analogous manner as done in section 3.2.2. The noteworthy difference in this procedure and the one described in the previous chapter is the determination of flow velocity along the segments of the major-expansion characteristic. This lead to the elimination of the usage of equation (3.3) to determine the critical velocity ratio. Thereby eliminating the dependency of the majority of transition arc calculation on the vortex flow theory. It should be noted that the starting point $(0, R^*_{lo})$ is still calculated using the vortex flow theory.

Before applying this new methodology to generate the transition arcs with the effect of body forces on them. Let us get an estimation of the order of magnitude of the body forces experienced by a supersonic radial rotor blade, let us consider the dimensions of a radial inflow runner as listed out in table 4.1. With these force values, an estimate of large forces experienced by the rotor can be made to design the transition arcs. In the following sections, the transition arcs, designed for different body forces, are investigated for both perfect and real gas.

4.2.1. Transition Arc with Body Forces for Perfect Gas

The influence of an external force per unit mass on the transition arcs' geometry is analyzed and compared. For a radial-inflow turbine, the centrifugal forces in the rotor's reference frame act in the

opposite direction of the fluid flow, although the centrifugal forces increase radially outwards. For the sake of simplicity, a case with a constant body force acting in the negative x-direction is considered to design the inlet upper & lower transition arcs for a radial rotor blade working in perfect gas region. The operating point chosen for designing the arc has the properties mentioned in the table 3.1 and the working fluid is Toluene.

It should be noted here that at the force magnitudes listed in table 4.1, a converged solution from CFD simulations (discussed in next chapter) could not be reached due to such high magnitudes of external body force. Therefore, in the rest of the thesis, a body force value is considered which is one order of magnitude less than the values mentioned in table 4.1.

Assuming a constant force per unit mass of $5 \times 10^4\ m/s^2$ acting in the negative x-direction on the the blade in the non-dimensional coordinate system $(X^* - Y^*)$, while considering the axial component of the fluid flow to be in the positive x-direction. As depicted in figure 4.2 this constant body force should act at the angle α_{lo} on the lower transition arc. Because the non-dimensional coordinate system of the lower transition arc $(X^*_{lo} - Y^*_{lo})$ is later rotated by the angle α_{lo} (equation 3.41) to obtain the final arc in $(X^* - Y^*)$ system. This suggests that the transition arc experiences the force at the angle α_{lo} in $(X^*_{lo} - Y^*_{lo})$, which later becomes horizontal in $(X^* - Y^*)$ after rotating the resulting arc. In the previous chapter, the angle α_{lo} was calculated after generating the transition arc. However, in this case it is required during the calculation of the arc therefore, it is found by an iterative procedure by initializing its value. The sign convention of positive angles in counter-clockwise direction should be kept in mind.

Applying the force per unit mass $F_{Bx} = -5 \times 10^4\ m/s^2$ at the angle α_{lo} in the compatibility equation (4.8) and following the new design method elaborated in the previous section, yields an inlet lower transition arc with the constant force's effects in $(X^*_{lo} - Y^*_{lo})$ system as illustrated in the figure 4.3(a).

To study the effects of body forces, these new transition arcs are plotted with the arcs generated without any body force. The consequence of the body force on the arc's curvature is apparent. Since the lower transition arc is calculated from right to left in the figure 4.2, the presence of a negative force in the compatibility equation (4.8) reduces the velocity attained at different arc segments, thus making it harder for the arc to reach the desired Mach number from M_{lo} to M_{in}. This is compensated by having a longer transition arc and therefore further expanding the flow field as compared with the no body force case.

In a similar manner, the negative force's effects can be observed on the inlet upper transition arc in $(X^*_{up} - Y^*_{up})$ system as shown in figure 4.3(b). The upper transition arc performs a sequential increase in the incoming Mach number to the required at the upper circular arc via a series of expansion fans. The negative force in the compatibility equation (4.8) assists in lowering the Mach number from the upper circular arc to the inlet Mach number during the formation of the upper arc. Hence, a shorter upper transition arc is generated in comparison with the no body force case.

On the other hand, in the case of a radial-outflow turbine, the centrifugal forces act in the direction of flow. This is the case where the axial component of the fluid flow and the centrifugal force both operate in the same direction. The figures 4.4(a) & 4.4(b) illustrates the resulting lower & upper transition arcs with a constant force per unit mass of $F_{Bx} = +5 \times 10^4\ m/s^2$ acting at α_{lo} in $(X^*_{lo} - Y^*_{lo})$ system. These arcs are generated for the same operating conditions listed in the table 3.1. In contrast with the negative force arcs, the lower transition arc is shorter and the upper transition arc here is longer than the arcs without any body force.

4.2.2. Transition Arc with Body Forces for Real Gas

In this section, the similar analysis with the constant force per unit mass is undertaken while also considering the dense gas effects on the transition arc. Both lower & upper transition arcs are generated for Toluene operating at conditions mentioned in table 3.2. Figures 4.5(a) & 4.5(b) show an analogous response of both lower & upper transition arc's curvature in the dense gas region as their perfect gas counter parts. Due to the same reasoning of constant negative force inhibiting the attainment of desired Mach number, even in dense gas region the lower transition arc is longer and the upper transition arc is shorter as compared with no body force arcs operating in the dense gas region.

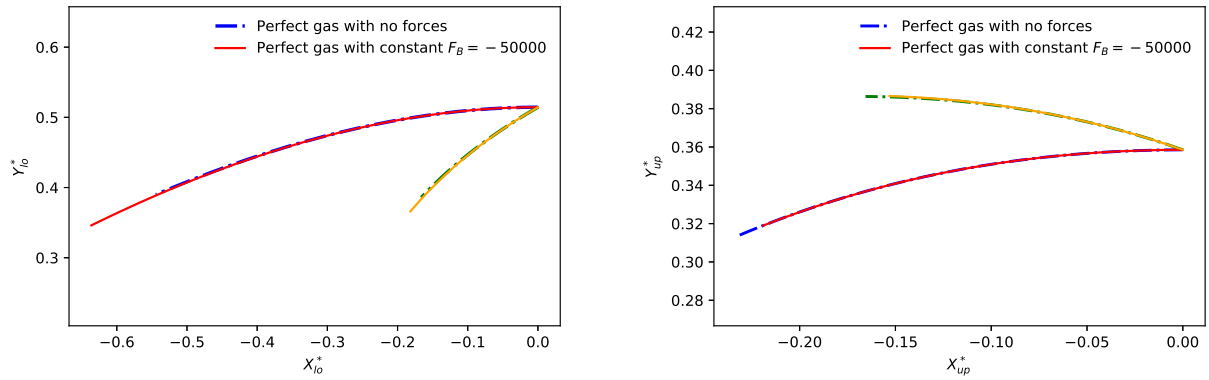

(a) Lower transition arc (b) Upper transition arc

Figure 4.3: Comparison between transition arcs with & without constant force per unit mass in opposite direction of the flow designed in perfect gas conditions (green & yellow lines represent the major-expansion/compression characteristic line for lower & upper transition arcs)

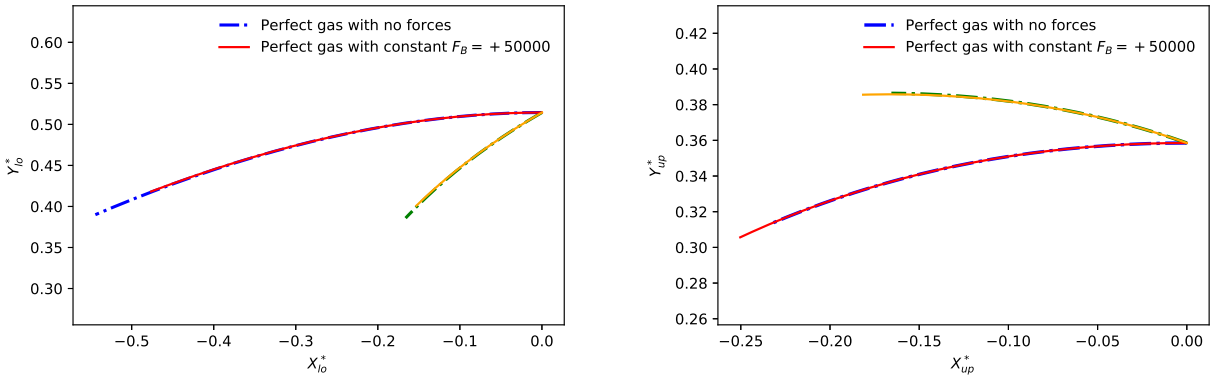

(a) Lower transition arc (b) Upper transition arc

Figure 4.4: Comparison between transition arcs with & without constant force per unit mass in the direction of the flow designed in perfect gas conditions (green & yellow lines represent the major-expansion/compression characteristic line for lower & upper transition arcs)

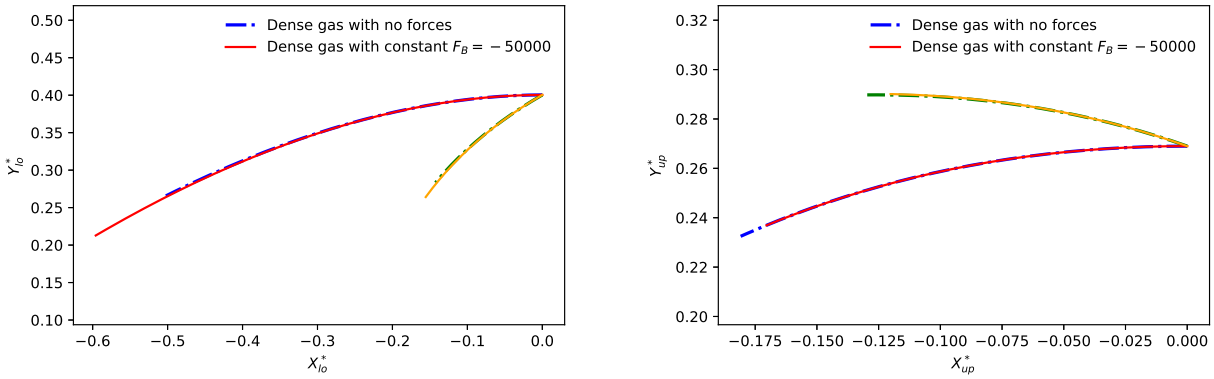

(a) Lower transition arc

(b) Upper transition arc

Figure 4.5: Comparison between transition arcs with & without constant force per unit mass in opposite direction of the flow designed in the dense gas region (green & yellow lines represent the major-expansion/compression characteristic line for lower & upper transition arcs)

4.3. Blade Generation

The lower & upper transition arcs with the influence of body forces on their curvature are now integrated with the rest of the blade geometry. The whole blade is obtained by following the same procedure of rotating the transition arc's coordinate system, adding the circular arc sections and the straight lines as followed in the section 3.4. In case of a constant force, the inlet geometry can be mirrored to yield a similar outlet blade section and obtain a symmetric rotor blade. This can be done only in the constant force case as both at the inlet & outlet sections, the flow field is equally opposed by the constant force.

It should also be recalled that the circular arc section of the supersonic axial rotor blade is designed based on the vortex-flow theory. However, the presence of body forces makes the general vortex equation (3.1) invalid. Thereby, it mandates the revaluation of this theory in the presence of external body forces and establish a new relation defining an irrotational flow with body force's influence on it. Such that the shock-free turning of the supersonic flow field can still be attained. Even after numerous attempts, this aspect of the supersonic radial rotor design could not be explored more in the present thesis work due to time constraints. The author recommends investigating the ways to change the flow passage area between the concentric circular arcs such that the reduction in the Mach number due to the opposing force is counteracted by the expansion and the Mach number at the upper & lower surfaces are maintained to be constant. This will be done at the expense of static pressure. The resulting blade would not be impulse but rather quasi-impulse blade due to equal inlet & outlet Mach numbers but not equal pressures.

For the blades generated in this chapter, the vortex flow theory is assumed to be valid even under the influence of external body forces. Hence, the circular arc sections are added to the radial rotor geometry in a similar manner as done in the section 3.4. The radial rotor geometries presented in this section have the impact of body forces only on the transition arcs. This capability of body force inclusion in the design methodology is added to the COMOC design tool to allow it to generate supersonic rotor geometries with the body force influence on the transition arcs in both perfect & dense gas region

Let us compare the radial rotor blade generated using perfect gas model with and without the effect of forces on the transition arcs. For visualization purposes, the same plot is presented in two different coordinate systems $(X^* - Y^*)$ and $(X^*/ch^* - Y^*/ch^*)$. In the latter system, the non-dimensional system $(X^* - Y^*)$ is normalized with the dimensionless chord (ch^*). In the figure 4.6(a), the absence of external forces on the circular arc section can be observed right away as the two geometries overlap each other in their respective circular arc section. Whereas, due to the transition arcs, the blade with the forces (red solid line) is longer in comparison with the one (blue line) without the forces. Thereby, resulting in a higher inlet-to-throat area ratio in the red rotor, which is desired to reach the Mach number specified

	Blade without force	*Blade with force*
Solidity	2.921	2.807
CR	0.805	0.721

Table 4.2: The blade geometry parameters at the same perfect gas operating point for blades with and without horizontal constant body forces

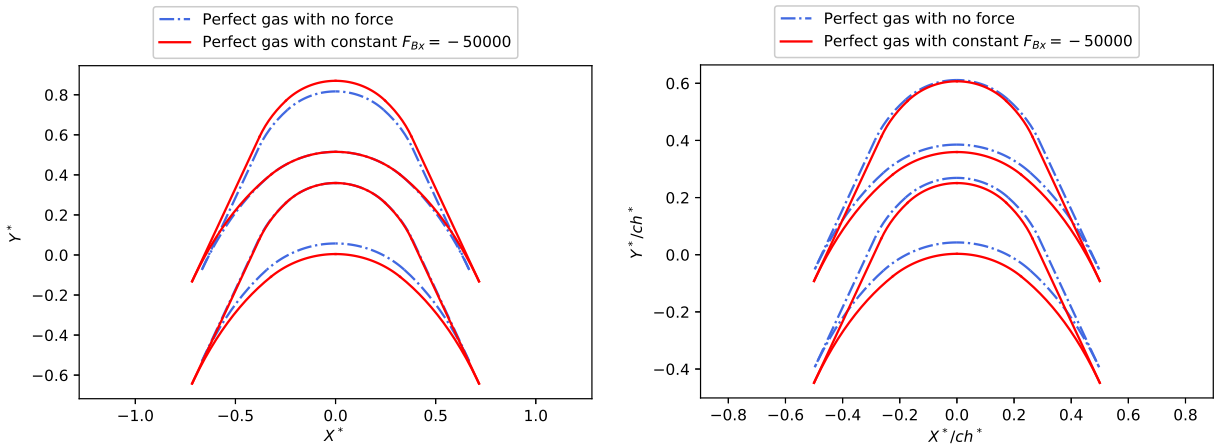

(a) (b)

Figure 4.6: Comparison between the rotor geometries with & without constant force per unit mass in opposite direction of the flow designed in perfect gas region depicted in (a) $(X^* - Y^*)$ and (b) $(X^*/ch^* - Y^*/ch^*)$ coordinate system

in the circular arc section as seen in the figure 4.6(b). The geometrical parameters namely the solidity and contraction ratio are mentioned in the table 4.2. The solidity of a blade is defined as the ratio of the axial chord (ch^*) and the pitch (G^*), where these parameters are normalized with the radius of the sonic streamline (r^*). The contraction ratio (CR) is the throat-to-inlet area ratio. It can be noticed that the presence of forces has reduced the solidity and the contraction ratio of the blade by 3.9% & 10.43%, respectively, justifying the higher inlet-to-throat area ratio. A similar behaviour was observed for the blade geometries designed for operating conditions in the dense gas region.

The influence of the horizontal constant force on the blade geometry, designed for dense gas conditions of table 3.2, can be studied by comparing the geometry with its perfect gas counterpart experiencing the same constant force as shown in the figures 4.7(a) & 4.7(b). The blades can be seen shifted with respect to each other in the figure 4.7(a) due to the different values of critical velocity (M^*) for perfect gas & dense gas case which governs the value of dimensionless radius (R^*) on the Y^* axis. Moreover, the dense gas blade is narrower than the perfect gas blade with a smaller chord, which leads to higher flow turning. In the figure 4.7(b), the typical behaviour of dense gas blade can be noticed due to the higher inlet-to-throat area ratio which is also justified by the smaller contraction ratio as compared with the perfect gas blade as shown in the table 4.3. The dense gas effects on the rotor geometry has led to a decline in solidity by 8.48% and in the contraction ratio by 10%.

	Perfect gas	*Dense gas*
Solidity	2.807	2.569
CR	0.721	0.649

Table 4.3: The blade geometry parameters with horizontal constant body force designed in perfect gas & dense gas region

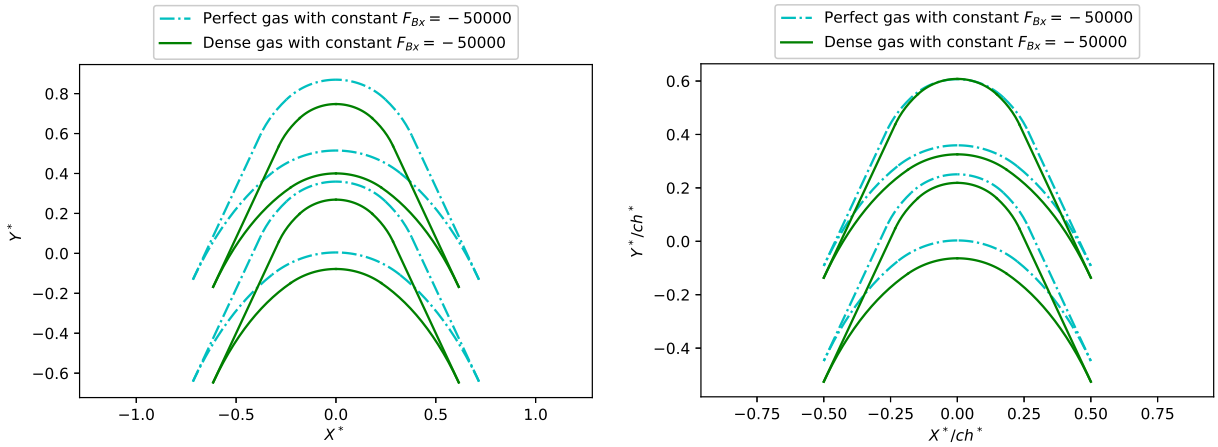

Figure 4.7: Comparison between the rotor geometries with the same constant force per unit mass in opposite direction of the flow designed in perfect gas region and dense gas region depicted in (a) $(X^* - Y^*)$ and (b) $(X^*/ch^* - Y^*/ch^*)$ coordinate system

5

Results & Discussions

This chapter undergoes the validation of the two design tools (Boxer-Bufi & COMOC tool) in both perfect & dense gas region. First the resulting blades from the two tools are compared with each other using the same EOS. This is followed by the validation of these tools using CFD analysis. The inclusion of a constant body force in the blade geometry is also investigated with steady inviscid CFD simulations for both perfect and dense gas region.

The design methodology adopted to generate supersonic rotor blades is based on Method of characteristics (MOC). The design tools developed in this work use MOC to generate transition arcs of the supersonic rotor blades. Although MOC is an accurate method to solve hyperbolic PDEs as established in the previous chapters, it is still an approximation process which mandates the verification of the design tools with relatively higher accuracy tool. In this chapter, the rotor geometries generated so far are validated with CFD analysis performed using a commercial simulation package. Furthermore, the COMOC tool using the modified compatibility equation is compared with the Boxer-Bufi tool, which uses the Prandtl-Meyer function for perfect gases. These tools are also compared with each other in the dense gas region. In the end, the basic case of adding a constant external force in x-direction is analyzed. The first step towards generating supersonic radial rotors is compared with the CFD simulations by subjecting the computational domain to the same constant body force.

5.1. Numerical Setup for CFD

To get a better validation of the rotor design tool, the supersonic flow field around the axial rotor geometry is numerically simulated using the commercial CFD package: SU2 developed at Stanford university in 2012 [35]. It is an open-source compressible & incompressible Euler, Navier-Stokes & RANS solver written in C++. The simulations performed in this chapter are assuming a steady, inviscid & isentropic flow. Therefore, an Euler solver is used to obtain the CFD results and the boundary layer effects are not considered as they are out of scope of this project.

Since the supersonic flows are dealt with in this work, compressible Euler equations are solved. The Finite Volume Method is used in the Euler solver to discretize the PDEs. The Euler implicit time-stepping scheme is used to advance in time due to its inherent stability in comparison with the explicit schemes. The physical time stepping is also used in steady state case to reach a converged solution. The spatial accuracy is kept in check by ensuring second-order accurate solutions which also ensures oscillations free solution across a discontinuity. The convective fluxes are discretized using the upwind scheme (ROE) [36].

An important design aspect of a rotor blade is the Mach number & pressure distribution along its surface. Therefore, these parameters are compared with the CFD results to verify the design tool. All the simulation results obtained are second-order accurate and the conserved variables converged to residuals in 10^{-9} order of magnitude.

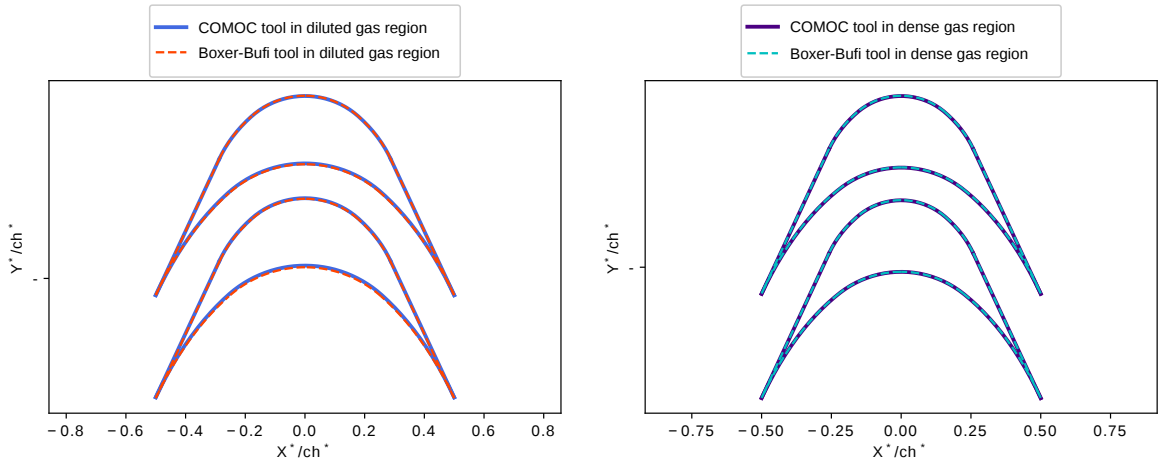

(a) (b)

Figure 5.1: Comparison between the supersonic axial rotor geometries generated by Boxer-Bufi & COMOC design tools in (a) perfect gas region and (b) dense gas region (with relative input parameters: $M_{up} = 2.0$, $M_{in} = 2.5$, $M_{lo} = 3.0$ & $\beta_{in} = 65^o$)

5.2. Supersonic Axial Rotor

The resulting axial rotor blades obtained from the Boxer-Bufi tool and the COMOC tool are illustrated in the figures 5.1(a) & 5.1(b). The rotors in the figure 5.1(a) are designed for Toluene using the perfect gas model in the diluted gas region (table 3.1), where perfect gas laws can be assumed to be valid. The blades from both tools are overlapping each other suggesting a compliance between the tools when used for perfect gases. Similarly, in the figure 5.1(b), the rotor blades yielded by both tools are designed using properties from CoolProp library as the chosen operating point is in the dense gas region of Toluene (table 3.2). In this case as well, both tools can be noticed to be in proper agreement with each other.

5.2.1. CFD Validation of Axial Rotor Tool

The design tool to generate the supersonic axial rotor blades are validated by simulating the flow field around them. First the tool is validated for perfect gas rotors and then for dense gas rotors.

CFD Results for Axial Rotor Designed for Perfect Gas

A 2D unstructured mesh is generated using an in-house mesh generator. The mesh boundaries are named in the figure 5.2. The designed unstructured mesh has 8808 triangular elements. The geometry of the axial rotor is determined by the design tool for the conditions listed out in the table 3.1. For the simulation, the perfect gas model is used as the equation of state (EOS) with Toluene ($\gamma = 1.04$) working in diluted gas region, $P_{o,r} = 0.05$ & $T_{o,r} = 1.3$. The desired flow boundary conditions are prescribed on all boundaries of the domain. Since the desired flow is supersonic ($M_{in} = 2.5$), the static conditions, as indexed in the table 5.1, are specified at the *INFLOW* boundary. Due to inviscid flow consideration, the blade's boundary is considered as a wall and given a slip boundary condition (Euler), which means there is no flow in the direction perpendicular to the wall. In addition, the *OUTFOW* boundary is initialized with a back pressure. Whereas, the top & bottom boundaries of the domain namely, *PERTOP* & *PERBOTTOM*, are defined as periodic boundaries.

Figure 5.3 illustrates the resulting Mach contour plot obtained from the CFD simulations. The Mach distribution along the inflow & outflow of the domain can be noticed to be fairly uniform at the prescribed relative Mach number value. The suction and pressure side of the blade have attained the design Mach numbers as prescribed in the design tool. This can also be observed in the figure 5.4(a) which compares the CFD Mach distribution with the one defined in the tool.

The arcs are described in the same figure, where left side represents the blade's inlet and the right side denotes the outlet. The blade surface Mach number obtained from CFD results and the design

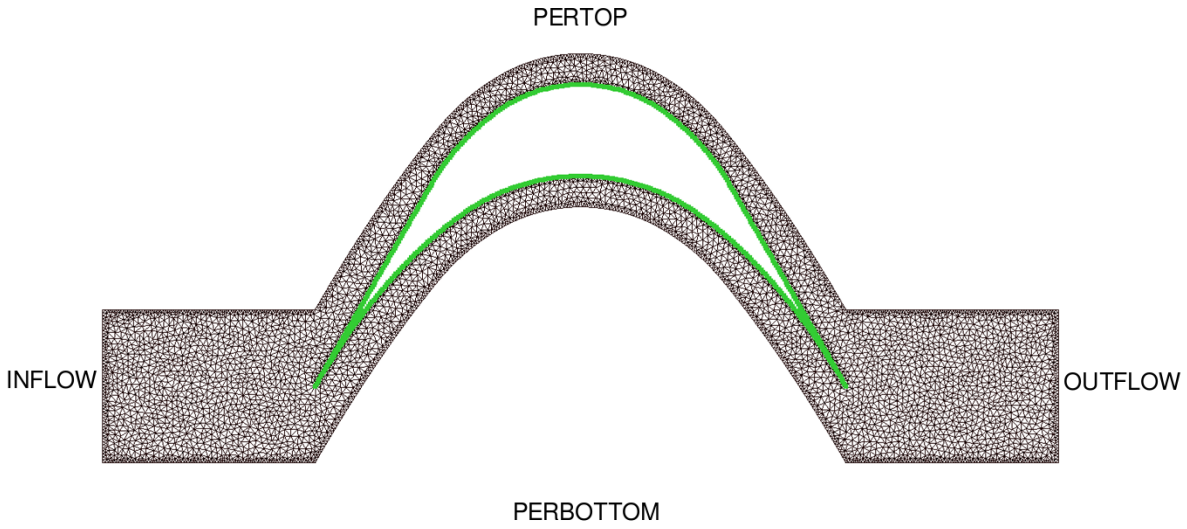

Figure 5.2: Unstructured mesh for axial rotor geometry with boundary names

$P\ [Pa]$	$T\ [K]$	$\rho\ [kg/m^3]$	M_{in}	β_{in}
9571.2	685.3	0.15	2.5	65^o

Table 5.1: Inflow boundary conditions for steady inviscid CFD simulation in the diluted gas region (P & T are static pressure & temperature)

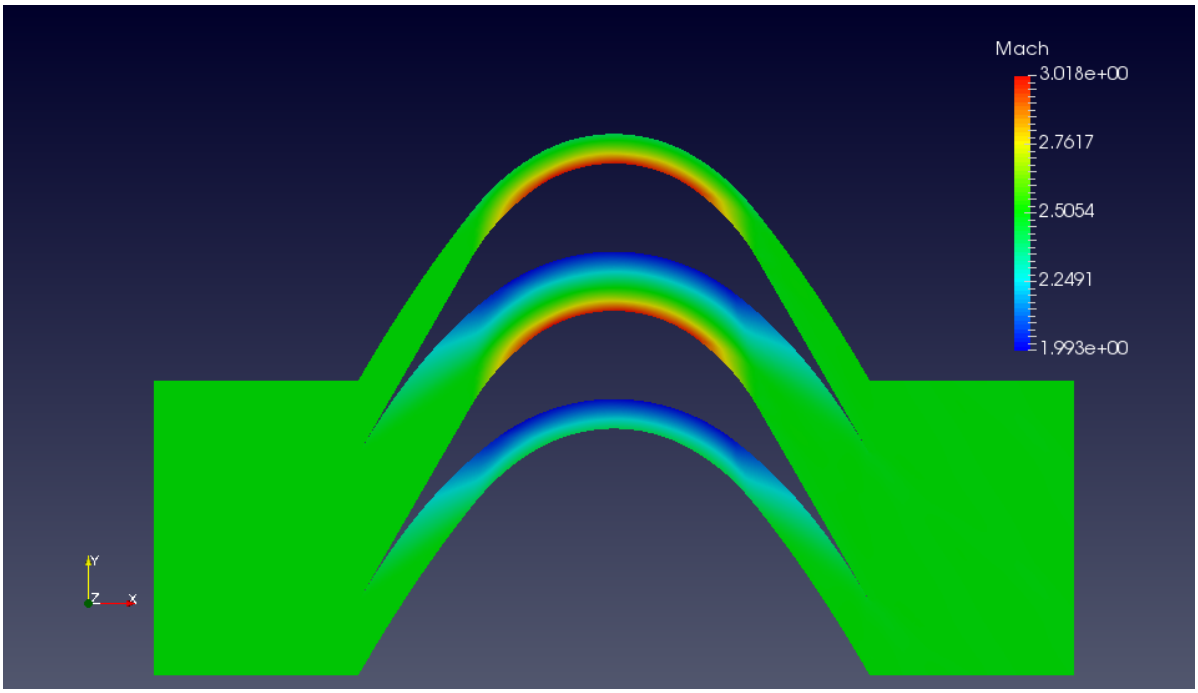

Figure 5.3: Mach contour plot for supersonic axial rotor designed for parameters in table 3.1 for perfect gas with no body force

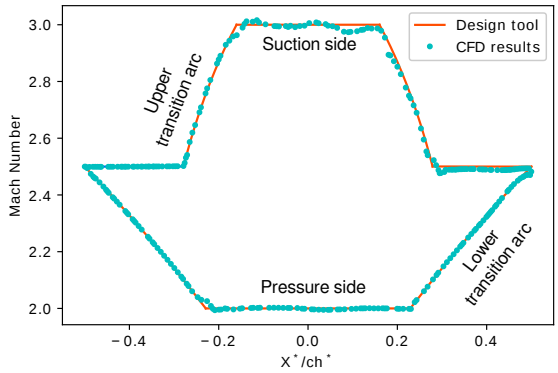

(a) Mach number distribution comparison between design tool & CFD results

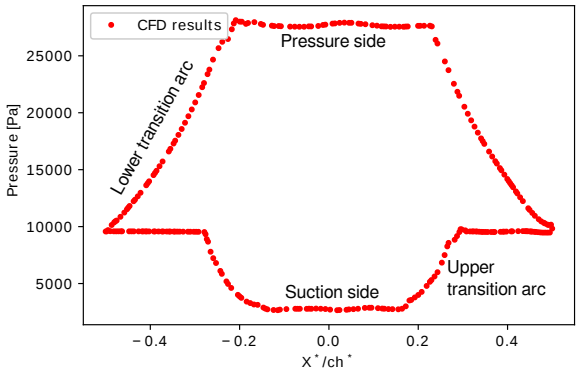

(b) Static pressure distribution by CFD results

Figure 5.4: Mach number & static pressure along the blade surface generated by inviscid CFD simulations for perfect gas with no body force

$P\ [kPa]$	$T\ [K]$	$\rho\ [kg/m^3]$	M_{in}	β_{in}
1.513	506.7	3.39	2.5	65^o

Table 5.2: Inflow boundary conditions for steady inviscid CFD simulation in the dense gas region (P & T are static pressure & temperature)

tool predictions are in good agreement with each other on the entire blade geometry. In addition, the static pressure distribution along the blade generated by the simulations is depicted in the figure 5.4(b). As expected, a constant static pressure is attained by the pressure & suction side circular arc sections. Whereas, the lower & upper transition arcs perform their intended role of gradually increasing & decreasing the pressure to reach the design values at the suction and pressure side respectively. These results validate the design tool's predictions for perfect gas axial rotor geometry.

CFD Results for Axial Rotor Designed for Real Gas

A similar validation procedure is done for the tool with the dense gas by performing a real gas inviscid CFD simulation on the axial rotor blade designed for toluene in the dense gas region. For real gas CFD simulation, Peng-Robinson (PR) gas model is used to capture non-classical behaviour of toluene in the dense gas region. It should be recalled that the design tool uses the thermophysical properties from the CoolProp library to model the dense gas effects. The dense gas rotors obtained using the parameters calculated by the PR EOS and the CoolProp library, were found to be in good agreement with each other. This brings some confidence in using the rotor geometry designed using the CoolProp library and using the same blade to run simulations with the PR gas model.

An unstructured mesh is generated for the rotor geometry having design parameters mentioned in table 3.2. The boundaries are given the same names as described in the figure 5.2. The inflow boundary conditions are chosen to be in highly non-ideal thermodynamic region with relative total reduced pressure ($P_{o,r}$) & temperature ($T_{o,r}$) values of 1.05, which shows the operating point's proximity to toluene's critical point. In this region, the compressibility factor ($Z = 0.57$) is well below 1, suggesting the non-ideal gas behaviour. The prescribed static conditions along with other inflow parameters are listed in the table 5.2. The remaining boundary conditions are kept the same as in the perfect gas case.

The Mach contour plot of the axial rotor operating in the dense gas region is illustrated in the figure 5.5. The design constraints on inlet, lower, & upper Mach numbers are met by inviscid CFD simulations. This can also be observed in the Mach distribution plot 5.6(a). However, there are wiggles on the suction side's circular arc in the CFD results. These wiggles can be explained due to the reflection of pressure/Mach waves in the vortex flow region. The expansion & compression waves generated on

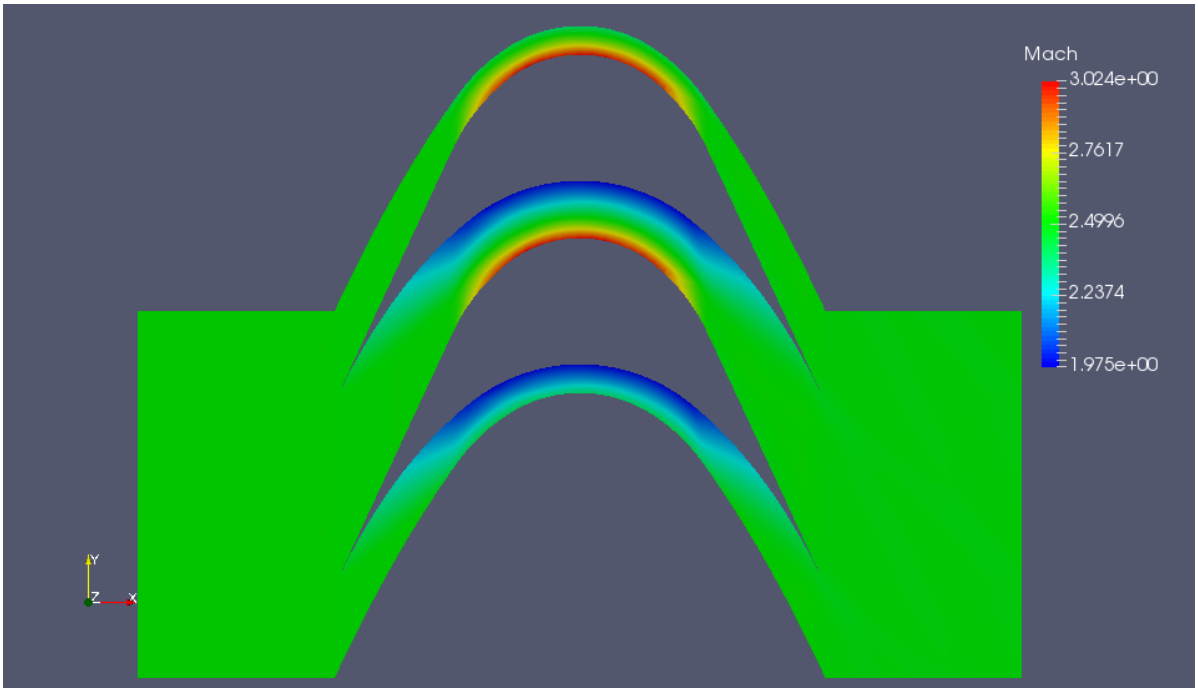

Figure 5.5: Mach contour plot for supersonic axial rotor designed for parameters in table 3.2 in dense gas region with no body force

the upper & lower transition arcs, respectively are reflected in between the concentric circular arcs giving rise to the wiggles on the circular arcs. Moreover, the static pressure distribution 5.6(b) is also fairly uniform in the dense gas case as well. Therefore, it is safe to say that the new design tool works as expected in both perfect & dense gas regions.

5.3. Supersonic Rotor with Body Forces

With the successful validation of COMOC design tool for supersonic axial rotor blade in both perfect & dense gas regions, the addition of constant force per unit mass in the designing of transition arcs of the rotor blades, can now be validated with inviscid CFD results. The external forces can only be added in the modified compatibility equation, therefore the COMOC tool cannot be compared with the Boxer-Bufi tool in this case. Consequently, only CFD validation of the COMOC tool is undertaken in this section.

In order to include the effects of external forces in the computational domain, the body force term in SU2 is used. It is added to the momentum and energy equation in the solver as a source term. A constant body force per unit mass of $5 \times 10^4\ m/s^2$ is applied in the negative x-direction i.e., opposite to the axial flow component. It should be noted that the presence of external body force in the whole domain will affect the flow properties even at the inflow and outflow sections. This leads to variations in the flow parameters at the blade's actual inlet. The axial component of the inflow velocity is constantly opposed by the constant external force leading to a change in the relative flow angle at the blade's inlet, thereby affecting the simulation results. Thus, the domain's inflow conditions need to be adjusted for the effect of external forces on the flow parameters along the length of inflow domain such that the actual blade's inlet get the intended flow parameters for which the blade is designed.

This correction can be taken care by solving the continuity, momentum & energy equation for steady 2D irrotational supersonic isentropic compressible flow for the rectangular inflow domain. However, during this exercise, a potential bug in SU2 was detected in case of negative direction of the body forces in the domain. The desired blade inlet flow could not be achieved even after considering the aforementioned correction on the inflow boundary. To check the applicability of the proposed correction, a CFD simulation of a rectangular domain of size $(0.8 \times 0.2\ m)$ is performed. The domain is subjected to an external body force of $5 \times 10^4\ m/s^2$ in the negative x-direction. The inflow boundary is prescribed with the corrected properties such that the outflow Mach number is 2.5 and the flow angle is 65^o.

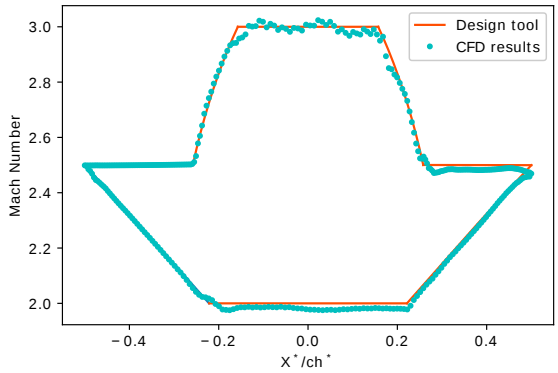

(a) Mach number distribution comparison between design tool & CFD results

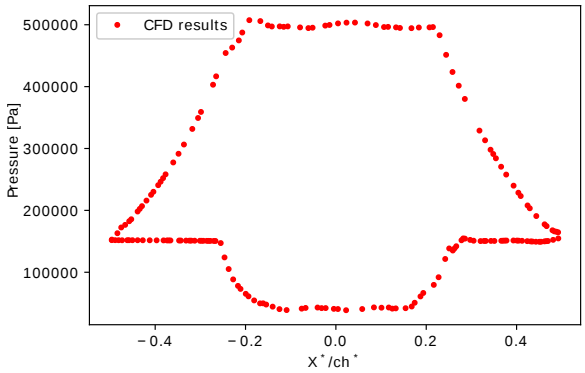

(b) Static pressure distribution by CFD results

Figure 5.6: Mach number & static pressure along the supersonic axial rotor surface obtained from inviscid CFD simulations in the dense gas region with no body force

P_o [bar]	T_0 [K]	Z	M_{lo}	M_{in}	M_{up}	β_{in}
17.08	1125	1.0	2.0	2.5	3.0	65^o

Table 5.3: Design parameters to generate rotor geometry with body force for CFD simulation using air [P_o & T_o are total pressure & temperature]

Figure 5.7 shows the resulting Mach contour plot of the rectangular domain. It can be noticed that the desired outflow Mach number of 2.5 is reached. However, in the presence of the blade in the domain, the desired blade inlet conditions could not be achieved when the body force is applied in the negative direction. On the other hand, for the case of body force applied in the positive x-directon, the correction seemed to be working as expected. Consequently, for the case of negative direction of body force, the inflow boundary condition is shifted right at the blade's inlet to ensure the desired prescription of the flow conditions at the blade's inlet, see the mesh in figure 5.8.

CFD Results for Perfect Gas Rotor with Body Forces

In order to validate the presence of body forces in the rotor design, a base case is simulated first. Furthermore, this case will also provide a reference to compare the simulations done with toluene later in the next section. A supersonic rotor with body force is designed and simulated for air ($\gamma = 1.4$) used as the working fluid in the perfect gas region. The unstructured mesh having 3934 triangular elements is generated for the design parameters in table 5.3 along with body force, $F_{Bx} = -5 \times 10^4\ m/s^2$. The mesh is illustrated in the figure 5.8. As described earlier, the inflow boundary of the domain has been shifted to the blade's actual inlet to ensure the desired blade inlet conditions are prescribed. In this case, the prescribed inflow boundary conditions are listed out in table 5.4. The whole computational domain is also subjected to the same constant body force. The outflow boundary is prescribed with a static pressure of 1 bar and the top & bottom boundaries are periodic.

The resulting Mach number & pressure distributions along the blade geometry are presented in figures 5.9(a) & 5.9(b). Even in the presence of external body force, the Mach number obtained from the simulation seems to be following the desired trend as predicted by the design tool at the inlet side

P [bar]	T [K]	ρ [kg/m^3]	M_{in}	β_{in}
1	500	0.69	2.5	65^o

Table 5.4: Inflow boundary conditions for steady inviscid CFD simulation of a blade with body force designed using air in the perfect gas region [P & T are static pressure & temperature]

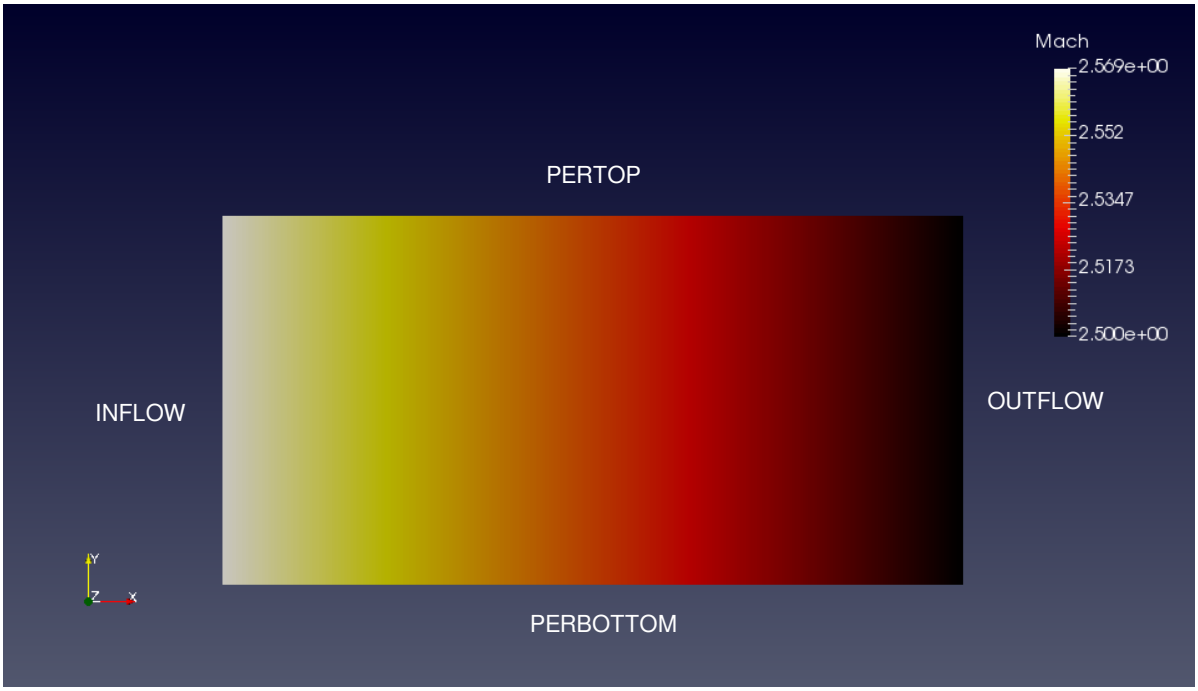

Figure 5.7: Mach contour plot of supersonic rectangular domain to check the applicability of the correction on the inflow boundary to obtain the desired outflow conditions in the presence of a body force

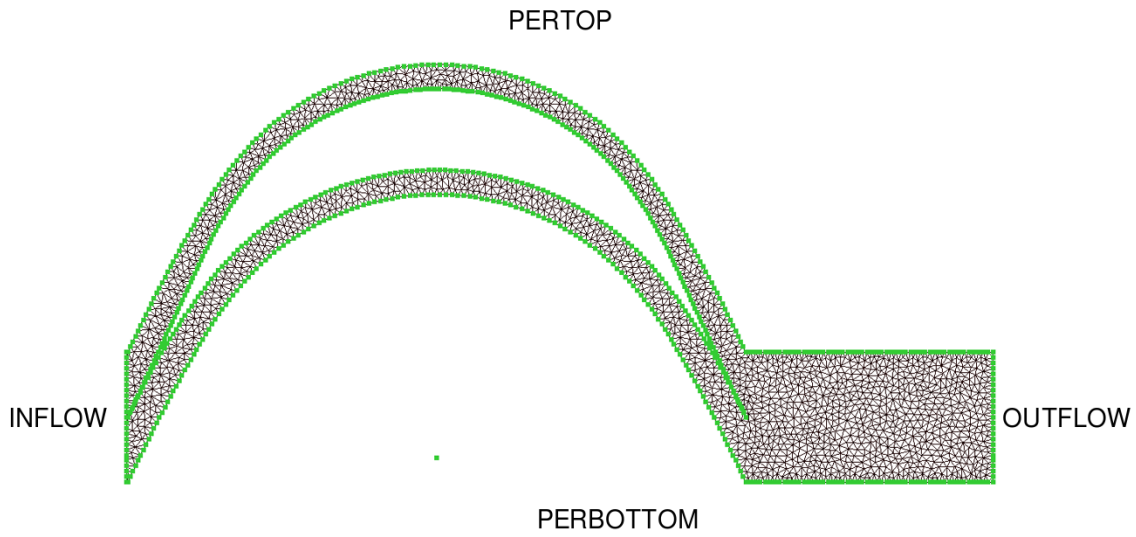

Figure 5.8: Unstructured mesh for supersonic rotor with body forces designed for air in the perfect gas region

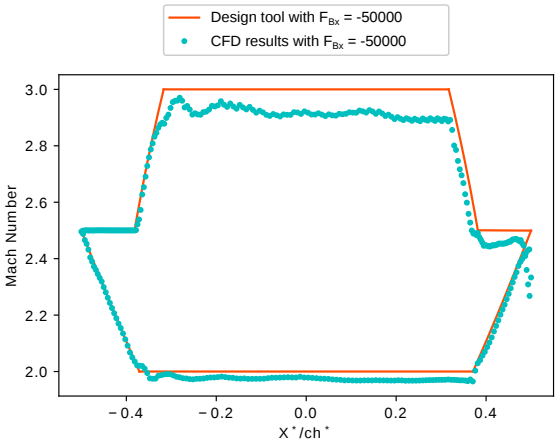

(a) Mach number distribution comparison between design tool & CFD results

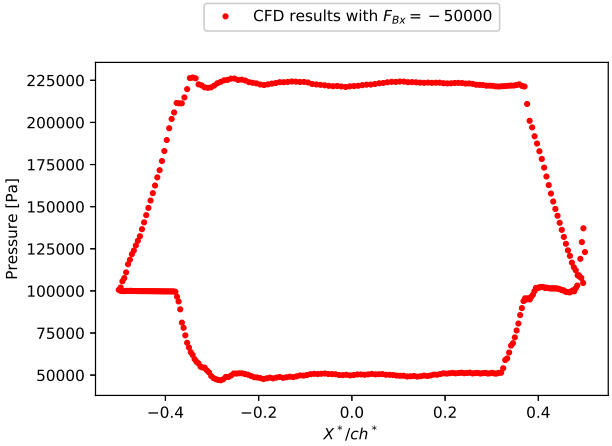

(b) Static pressure distribution by CFD results

Figure 5.9: Mach number & static pressure along the blade surface with body force yielded by CFD simulations for air

transition arcs. It should be recalled that the effect of body forces has not been incorporated in the design of circular arc section. Consequently, the result of force's non-inclusion can be noticed on the top & bottom horizontal lines in the figure 5.9(a) as there is an offset between the CFD results and the desired Mach numbers. Furthermore, the CFD Mach numbers at the outlet upper transition arc are following the desired trend qualitatively as there is a slight offset. However, the lower transition arc is properly overlapping the design tool predictions both at the inlet & the outlet. In the end, the straight outlet section has lower Mach numbers than the designed value. This can be explained based on the external forces increasing the pressure at the outlet section resulting in the drop of flow velocity. This is also seen in the outlet static pressures being around 3% higher than at the inlet in the figure 5.9(b). This validates the inclusion of body forces in the design criteria of transition arcs for air as working fluid. Now let us look at the CFD results of a blade designed with body force using toluene in the diluted gas region.

The working fluid is now changed to Toluene and the perfect gas inviscid CFD simulation is performed to compare the results with the design tool predictions to study the influence of constant body forces on the transition arcs. The boundary conditions prescribed at the inflow of the domain are listed out in the table 5.1. The rest of the boundaries are defined in a similar fashion as previous simulations.

Figure 5.10 shows the Mach contour plot for the case of Toluene working in perfect gas region with $-5 \times 10^4\ m/s^2$ constant body force. The resulting flow field is not satisfactory. The supersonic flow achieves the desired relative Mach number of 2.5 at the initial part of inlet straight line section, however, the suction & pressure side cannot attain their respective design Mach numbers. Furthermore, there is an oblique shock wave in the flow field at the trailing edge. The pressure gradient contour plot confirms this oblique shock as there is a strong pressure gradient at the outlet of the blade as shown in figure 5.11. This shock wave is then reflected off the outlet suction side which leads to very low Mach numbers at the outlet suction side. The presence of this oblique shock wave can be attributed to the change in flow angle imparted by the body force right at the outlet of the blade. The flow adjusts to this change in flow angle through an oblique shock wave. In addition, very high pressure gradients can be observed in the circular arc section of figure 5.11. These high pressure gradients are induced by the body force and the non-inclusion of body force effect in the design of circular arcs.

The figure 5.12(a) gives further insight in to the Mach numbers achieved in the simulation. At the blade's inlet straight line section, the Mach numbers are dropping in the flow direction due to the opposing force in negative x-direction. The flow can be seen accelerating almost half way on the inlet upper transition arc achieving a maximum Mach number of 2.67 only and then dropping further on the the transition arc. On the other hand, the Mach number trend on the lower transition arc seems to be

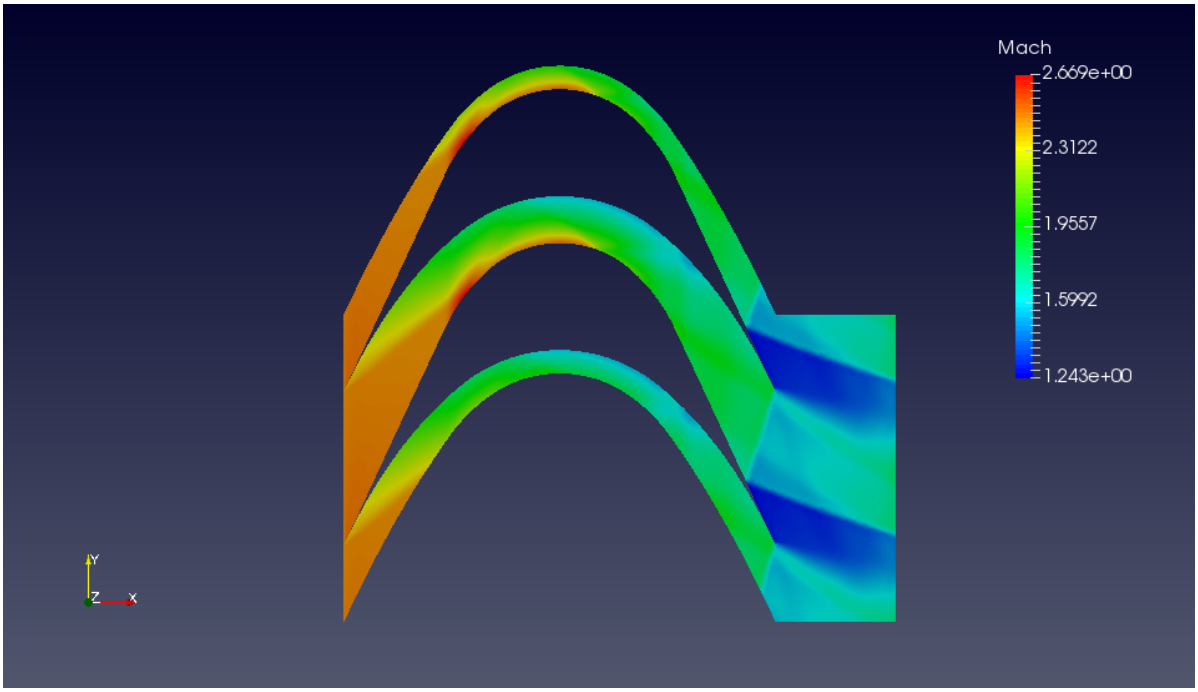

Figure 5.10: Mach contour plot for rotor with $F_{Bx} = -5 \times 10^4\ m/s^2$ for toluene in diluted gas region

uniformly deviating away from the design tool.

The static pressure on the pressure & suction side in the figure 5.12(b) is increasing along the circular arc under the influence of the body force. This explains why the Mach number drops. On comparing with the pressure distribution of no body force case 5.4(b), the pressure values along the pressure & suction side are generally higher despite the only change is the presence of external force in this case. In addition, the desired Mach distribution is attained in the case of air but not in the case of toluene. Therefore, the overall effect of the body force is found to be very strong in the case of Toluene. The true reason of this strange behaviour needs to be investigated further.

One of the possible reasoning for the mismatch in case of toluene could be the use of first-order discretization method during the calculation of transition arc in the COMOC tool. Perhaps, the Euler explicit method used to discretize equation (4.10) cannot capture the higher-order thermophysical relations of toluene. This reasoning could be corroborated by implementing the second-order accurate discretization schemes, such as Euler predictor-corrector in the determination of transition arcs.

Another possible reasoning could be the density effects being stronger for toluene than air and their interaction with the body force. The author suggests more investigation in this region to understand why the desired results could not be achieved even on the transition arcs adjusted for the body force in case of toluene.

To investigate further about the influence of the external force's magnitude on the supersonic flow field, different rotors are generated for various constant body forces ranging in between $-1 \times 10^4\ m/s^2$ to $-4 \times 10^4\ m/s^2$. All these blades are designed for the similar parameters of table 3.1 and simulated at the conditions 5.1. The consequence of increasing body force is observed in the figures 5.13(a) & 5.13(b). The higher opposing force leads to higher deviation on the inlet lower transition arc. Along the circular arc sections, the rate of decreasing Mach numbers rises with the increase in force. This is expected due to the non-inclusion of external force's impact on the circular arcs. The body force slows down the flow over these arcs. It was also observed that the oblique shock wave at the trailing edge moves in the upstream direction with the increasing body force leading to an earlier reflection off the outlet suction side.

CFD results for Dense Gas Rotor with Body Forces

In this subsection, the inviscid CFD simulation results of the blade designed in the dense gas region of toluene with body force are discussed. The rotor generated for conditions in table 3.2 with

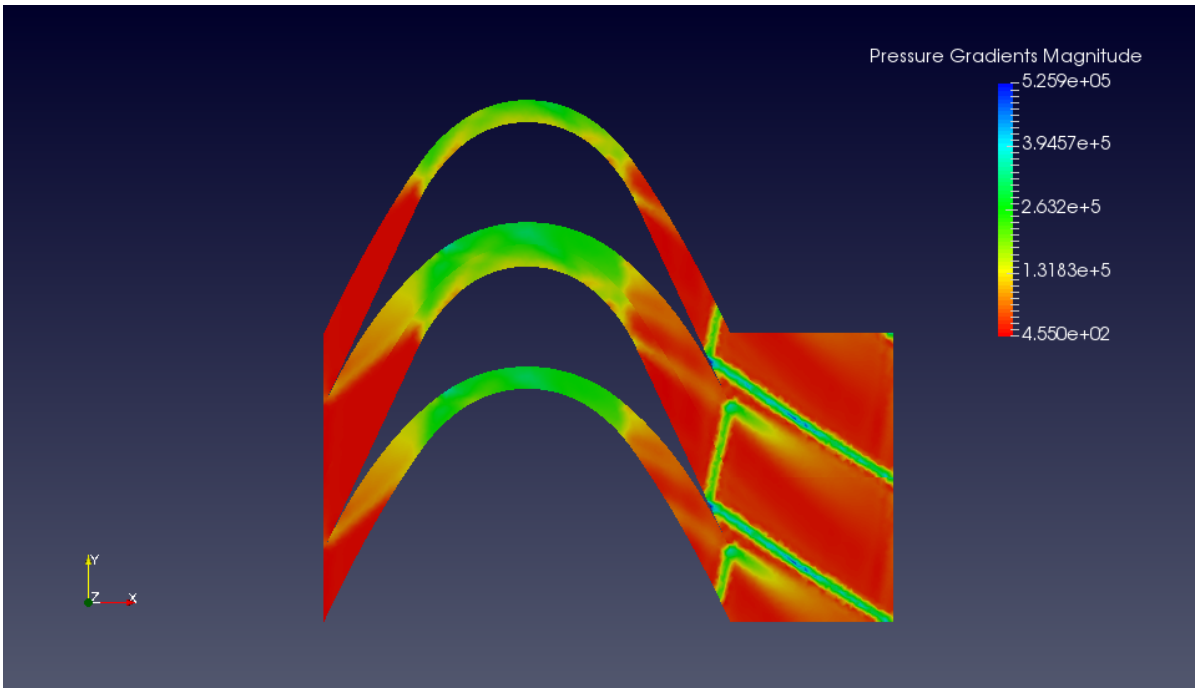

Figure 5.11: Pressure gradient contour plot for rotor designed for parameters in table 5.5 with $F_{Bx} = -50000\ m/s^2$ for toluene in the diluted gas region

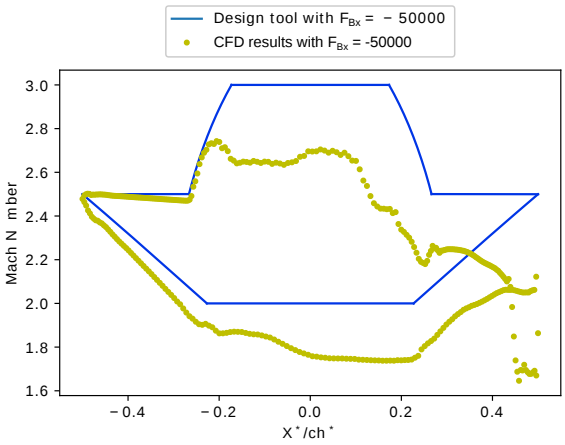

(a) Mach number distribution comparison between design tool & CFD results

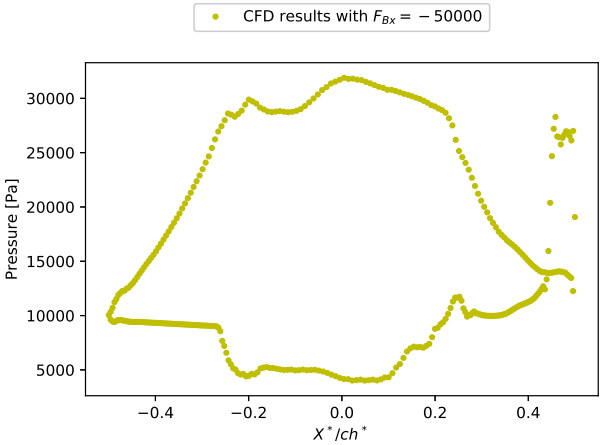

(b) Static pressure distribution by CFD results

Figure 5.12: Mach number & static pressure along the blade surface generated by CFD simulations with $F_{Bx} = -50000\ m/s^2$ for toluene in diluted gas region

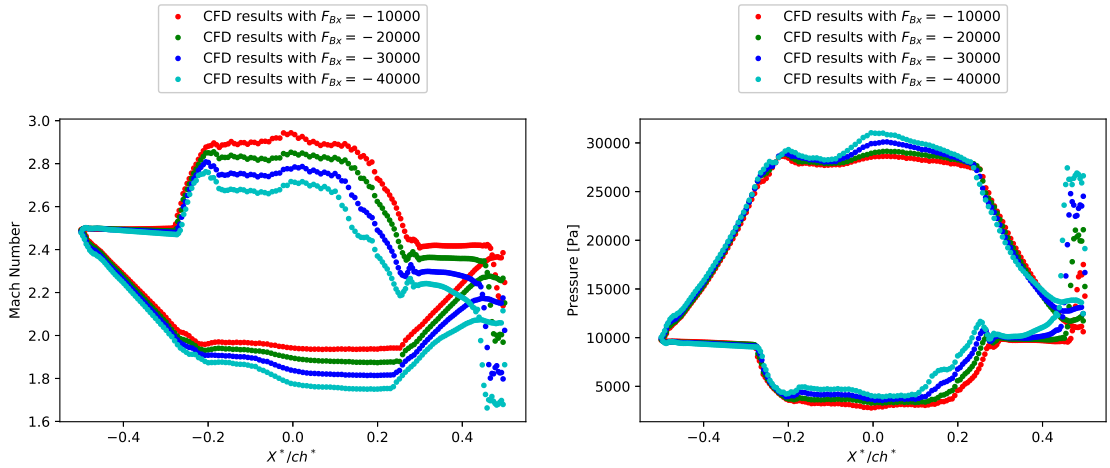

(a) Mach number distribution

(b) Static pressure distribution

Figure 5.13: Mach number & static pressure along the blade surface generated by CFD simulations with different body forces for toluene in diluted gas region

$F_{Bx} = -5 \times 10^4\ m/s^2$ gave the similar results as those elaborated in the last subsection. Therefore, to study the effects of a higher relative Mach number on a blade generated with the same body force, a different rotor geometry is designed for the parameters listed in the table 5.5. Keeping the same constant body force value, the design Mach numbers on the blade surface and inlet are increased.

The high design Mach numbers on the blade yielded a slightly better Mach number distribution as illustrated in figure 5.14. The highest Mach number reached on the upper transition arc gets pretty close to the design value of 4.0 as also depicted in the figure 5.16(a). This is due to the high relative inlet Mach number flow going against the same constant body force. In figure 5.15, the pressure gradients in the circular arc section are present but much lower in comparison with figure 5.11. Furthermore, the trailing edge shock wave is also shifted downstream in comparison with the one in figure 5.11 due to the high relative inlet Mach number. This leads to a shift of reflection point on the suction side closer to the blade's outlet.

Assuming that this trend continues, it suggests that high prescribed relative Mach numbers lead to a lower impact of body force on the Mach distribution. In addition to the effects of body force on the density of fluid, the effect of body force on the contraction ratio needs to be studied further to understand the behaviour of the flow field in the case of toluene.

Another possible explanation behind the observed results for Toluene could be the absence of body forces on the design of the circular arc section for two main reasons:

1. The design procedure of the transition arcs initiates by assuming the vortex flow theory to be valid even under the influence of external forces. This assumption can fundamentally affect the obtained curvature of the transition arcs thereby resulting in the deviation of results especially in the case of high molecular weight fluid.

2. The inlet-to-throat area ratio governs the Mach numbers in the supersonic passage and in this case the throat area is calculated based on the upper & lower circular arcs which do not take into account the body force effects.

Consequently, further research is paramount to check the hypotheses presented here. However, the author believe the design methodology & tools developed in this work are a promising step forward in the direction to realize a supersonic radial rotor design methodology.

$P_{o,r}$	$T_{0,r}$	Z	M_{lo}	M_{in}	M_{up}	β_{in}
1.05	1.05	0.57	3.0	3.5	4.0	65^o

Table 5.5: Rotor design parameters for Toluene in dense gas region

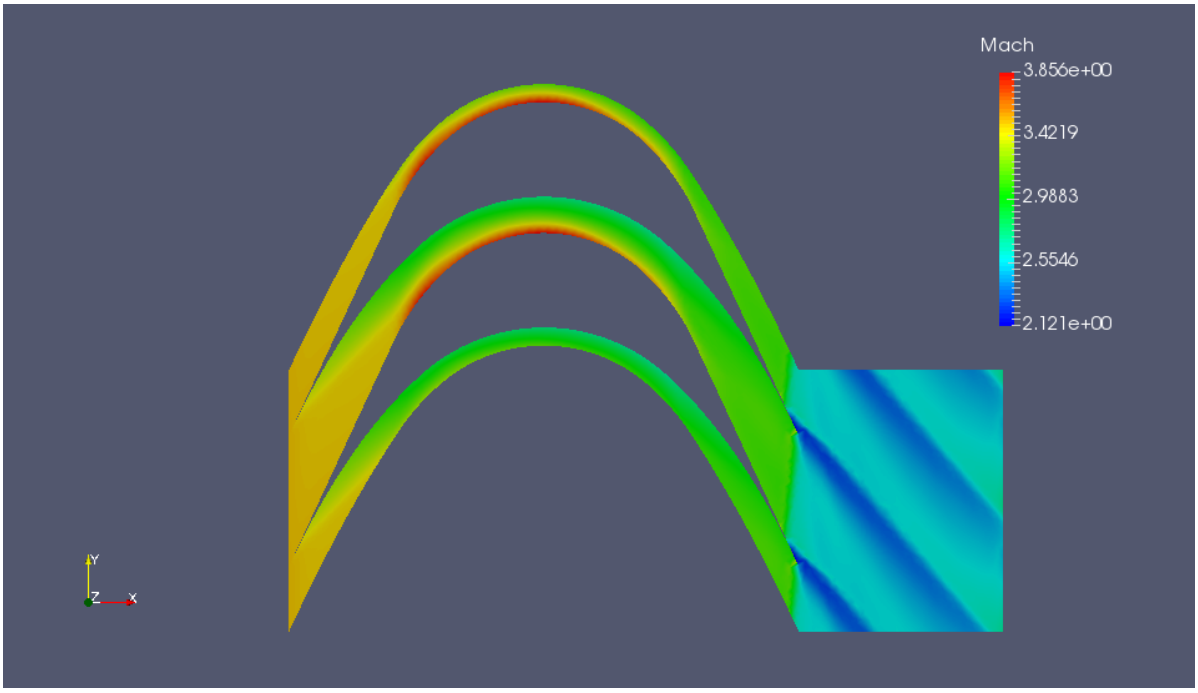

Figure 5.14: Mach number contour plot for rotor designed for parameters in table 5.5 with $F_{Bx} = -50000\ m/s^2$ for toluene in the dense gas region

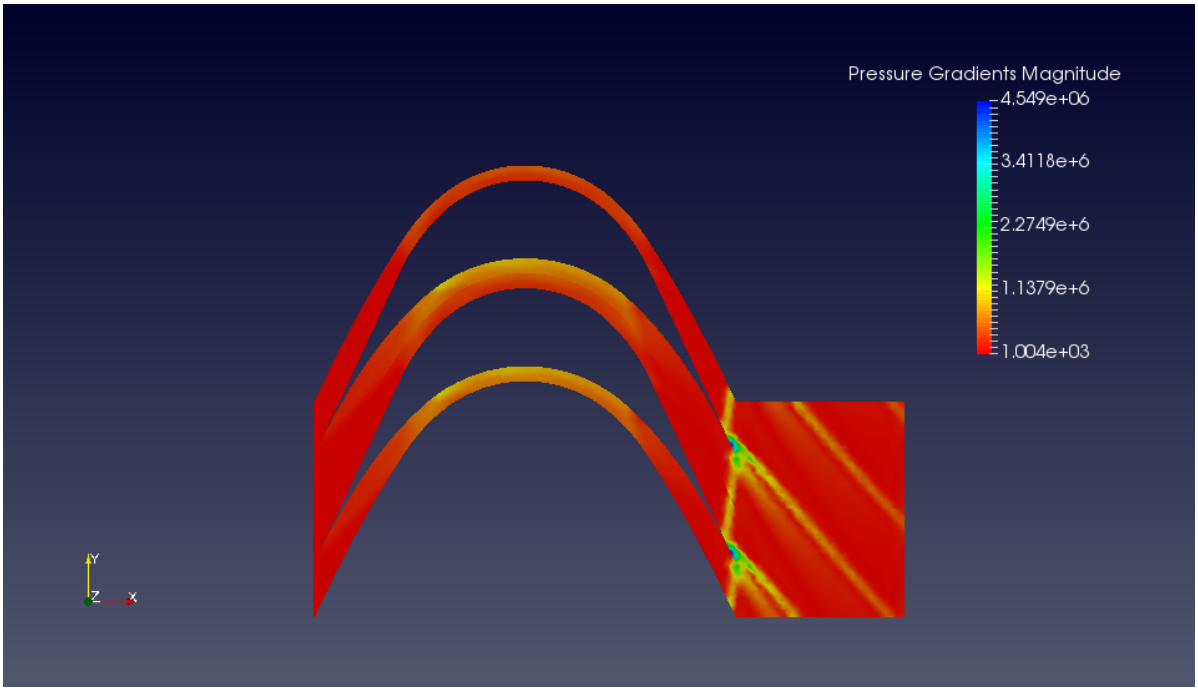

Figure 5.15: Pressure gradient contour plot for rotor designed for parameters in table 5.5 with $F_{Bx} = -50000\ m/s^2$ for toluene in the dense gas region

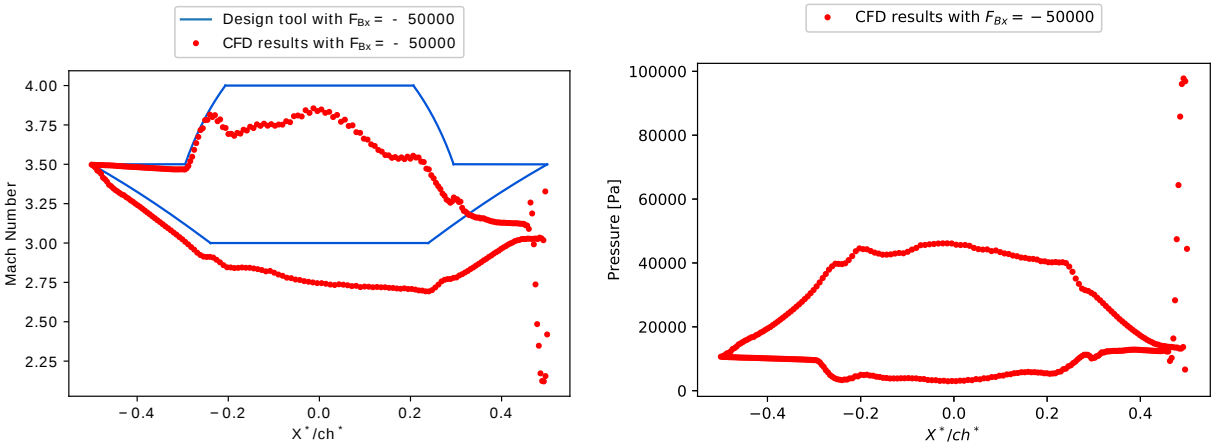

(a) Mach number distribution comparison with the design tool

(b) Static pressure distribution

Figure 5.16: Mach number & static pressure along the blade surface generated by CFD simulations with $F_{Bx} = -50000\ m/s^2$ for toluene in dense gas region

6

Conclusions & Recommendations

In this work, a novel design methodology is proposed for generating a supersonic radial rotor blades for the working fluids governed by both ideal gas laws and complex non-classical real gas behaviour. The suggested ideology extends the existing design procedure of a supersonic axial rotor. The inclusion of the effects of body forces, experienced by the flow in the rotating reference frame of a radial turbine, in the governing equations and the design procedure can generate a radial rotor blade.

In order to reach this goal, first the existing design methodology for supersonic axial rotors is introduced and discussed. This procedure is based on the Method of Characteristics (MOC) to design the transition arcs of axial rotors. The dependency of this methodology on Prandtl-Meyer angles limits its application only to perfect gas. A supersonic axial rotor design tool (Boxer tool) based on this methodology is developed in PYTHON. Another limitation posed by the use of Prandtl-Meyer angles in axial rotors includes no provision to consider the external body force effects on the rotor geometry. Therefore, a change in the methodology is suggested to avoid the usage of Prandtl-Meyer angles.

The modification involves the addition of body forces in the 2D steady Gas dynamics equation which is followed by deriving the characteristic & compatibility equations required to perform MOC. These equations are used to implement MOC to generate the transition arcs in which the body force's influence is included. A new design tool (COMOC tool) is also developed that gives more flexibility to the design methodology by incorporating the aforementioned process. This tool can be used to generate supersonic axial rotors and the rotor with body force effects on its transition arcs. In this work, the influence of body force is not included in the circular arc section as the underlying vortex-flow theory needs to be modified to account for the external force's effects. For the case of body force, only a constant force acting in x-direction is considered.

Both of the design tools are further enriched to generate supersonic rotor geometries that properly consider the non-classical behaviour of high molecular weight fluids operating in the dense gas region. With this capability incorporated, the Boxer tool is called Boxer-Bufi tool and the COMOC tool's name remains unchanged. The thermo-physical properties from the highly accurate CoolProp library are used to take into account the peculiar behaviour of dense gases in the determination of rotor shapes.

In the end, a validation exercise is performed to assess the reliability of the two design tools by comparing the resulting rotor geometries with steady inviscid CFD simulations using a commercial CFD package, SU2. The CFD results for supersonic axial rotor geometries without any body force give the satisfactory Mach number distribution over its surface for both perfect & dense gas region. Thereby, validating the design tools for the blades without body force. To validate the presence of body force on the transition arcs, a simple case of constant horizontal body force is simulated in CFD. Expected results are obtained for air used as working fluid. However, the CFD results obtained for the rotors with body force using toluene in both perfect & dense gas region seem to deviate from the design conditions. The explanation for these observations could be attributed to the body force influencing the density of the working fluid. However, a proper reasoning for these behaviours in case toluene needs to be investigated further. The author recommends potential directions to take this project further in the next section.

6.1. Future Work

This project takes the first step towards proposing a new design methodology for the design of supersonic rotors for radial turbines. Therefore, following recommendations are important for the continuation of the project to realize a supersonic radial rotor blade.

1. The revaluation of the vortex-flow theory under the influence of external force is required to ensure the body force's influence is considered also on the circular arc section. This can also be done by gradually changing the constant flow passage area between two concentric circles such that flow expansion can take place and the Mach number at their surfaces is kept constant at the expense of pressure. In this way the opposing effect of the body force is counteracted by flow expansion and a shock-free turning of the supersonic flow is still achieved.
2. The effects of body force on the rotor geometry generated for an organic fluid should be studied properly in both perfect & dense gas region. One of the possible directions is to understand the density variations in the presence of body force. This effect should be included in the design tool.
3. The accuracy of the numerical procedure used to discretize the modified compatibility equation can be improved by applying Euler predictor & corrector method or higher-order accurate numerical scheme.
4. Design the blade with body force and compare the CFD results of different Organic working fluids to establish the density effects on the results.
5. The next complexity in the blade design can be added by putting a constant body force in the direction perpendicular to the fluid flow to replicate the Coriolis force which is always perpendicular to the velocity direction. Followed by the validation of the resulting blade with the CFD simulations.
6. Since a bug was detected in SU2 for the cases of body force in the negative direction, a different CFD package can be used to verify the blade geometry with body force.
7. The rotor geometry generated for linearly varying force obtained from the tool should also be validated first with the CFD simulations before putting in the centrifugal forces in the design tool. Similarly the linearly varying Coriolis force can also be added in the design tool and validated. The distance between the major characteristic lines and the transition arcs should be kept in mind while implementing the linearly varying force or the centrifugal forces in the blade design.
8. The leading & trailing edges should be rounded off to give the blade more strength at the ends. However, this will require the considerations of started rotor & the unique incidence problem, which is a characteristic of supersonic axial rotor blades. These phenomenon should be studied under the influence of external body forces.
9. The viscous CFD simulations will give more realistic outlook on the performance of the radial rotor blades. This will require the need to consider the boundary layer phenomenon in the early stages of the design as the boundary layers reduce the effective flow passage area which may lead to lower than expected performance if not accounted for in the design stage.

Bibliography

[1] Y. Dai, J. Wang, and L. Gao, *Parametric optimization and comparative study of organic rankine cycle (orc) for low grade waste heat recovery,* Energy Conversion and Management **50**, 576 (2009).

[2] N. Anand, *Supersonic turbine design using method of characteristics,* (2016).

[3] M. R. P. G. S. D. Marc Linares, Alessandro Ciampitti, *Team 18: Design optimization of a supersonic nozzle,* (2015) 2015.

[4] J. Wlodarski, J. R. Sterrett, and E. Boxer, *Application of supersonic vortex-flow theory to the design of supersonic impulse compressor-or turbine-blade sections,* (1952).

[5] H. Chen, D. Y. Goswami, and E. K. Stefanakos, *A review of thermodynamic cycles and working fluids for the conversion of low-grade heat,* Renewable and sustainable energy reviews **14**, 3059 (2010).

[6] P. Colonna, E. Casati, C. Trapp, T. Mathijssen, J. Larjola, T. Turunen-Saaresti, and A. Uusitalo, *Organic rankine cycle power systems: from the concept to current technology, applications, and an outlook to the future,* Journal of Engineering for Gas Turbines and Power **137**, 100801 (2015).

[7] M. Villarini, E. Bocci, M. Moneti, A. Di Carlo, and A. Micangeli, *State of art of small scale solar powered orc systems: a review of the different typologies and technology perspectives,* Energy Procedia **45**, 257 (2014).

[8] B. Dong, G. Xu, X. Luo, L. Zhuang, and Y. Quan, *Analysis of the supercritical organic rankine cycle and the radial turbine design for high temperature applications,* Applied Thermal Engineering **123**, 1523 (2017).

[9] J. Bao and L. Zhao, *A review of working fluid and expander selections for organic rankine cycle,* Renewable and sustainable energy reviews **24**, 325 (2013).

[10] P. A. Thompson, *A fundamental derivative in gasdynamics,* The Physics of Fluids **14**, 1843 (1971).

[11] H. A. Bethe, *On the theory of shock waves for an arbitrary equation of state,* in *Classic papers in shock compression science* (Springer, 1998) pp. 421–495.

[12] P. Duhem, *On the propagation of shock waves in fluids,* Z. Phys. Chem **69**, 169 (1909).

[13] P. Colonna, A. Guardone, and N. Nannan, *Siloxanes: a new class of candidate bethe-zel'dovich-thompson fluids,* Physics of Fluids **19**, 086102 (2007).

[14] I. H. Bell, J. Wronski, S. Quoilin, and V. Lemort, *Pure and pseudo-pure fluid thermophysical property evaluation and the open-source thermophysical property library coolprop,* Industrial & Engineering Chemistry Research **53**, 2498 (2014), http://pubs.acs.org/doi/pdf/10.1021/ie4033999 .

[15] M. White, *The design and analysis of radial inflow turbines implemented within low temperature organic Rankine cycles*, Ph.D. thesis, City University London (2015).

[16] S. Declaye, S. Quoilin, L. Guillaume, and V. Lemort, *Experimental study on an open-drive scroll expander integrated into an orc (organic rankine cycle) system with r245fa as working fluid,* Energy **55**, 173 (2013).

[17] A. P. Wheeler and J. Ong, *The role of dense gas dynamics on organic rankine cycle turbine performance,* Journal of Engineering for Gas Turbines and Power **135**, 102603 (2013).

[18] D. VanZante, E. Envia, and M. G. Turner, *The attenuation of a detonation wave by an aircraft engine axial turbine stage,* (2007).

[19] G. Paniagua, M. Iorio, N. Vinha, and J. Sousa, *Design and analysis of pioneering high supersonic axial turbines,* International Journal of Mechanical Sciences **89**, 65 (2014).

[20] C. Colclough, *Design of turbine blades suitable for supersonic relative inlet velocities and the investigation of their performance in cascades: Part ii-experiments, results and discussion,* Journal of mechanical engineering science **8**, 185 (1966).

[21] A. Aldo and B. Argrow, *Dense gas flow in minimum length nozzles,* Journal of fluids engineering **117**, 270 (1995).

[22] A. Guardone, A. Spinelli, and V. Dossena, *Influence of molecular complexity on nozzle design for an organic vapor wind tunnel,* Journal of engineering for gas turbines and power **135**, 042307 (2013).

[23] E. A. Bufi, B. Obert, P. Cinnella, and C. F. ENERTIME, *Fast design methodology for supersonic rotor blades with dense gas effects,* in *3rd International Seminar on ORC Power Systems* (2015).

[24] A. P. Weiß, T. Popp, J. Müller, J. Hauer, D. Brüggemann, and M. Preißinger, *Experimental characterization and comparison of an axial and a cantilever micro-turbine for small-scale organic rankine cycle,* Applied Thermal Engineering **140**, 235 (2018).

[25] L. Da Lio, G. Manente, and A. Lazzaretto, *A mean-line model to predict the design efficiency of radial inflow turbines in organic rankine cycle (orc) systems,* Applied Energy **205**, 187 (2017).

[26] D. Fiaschi, G. Innocenti, G. Manfrida, and F. Maraschiello, *Design of micro radial turboexpanders for orc power cycles: From 0d to 3d,* Applied Thermal Engineering **99**, 402 (2016).

[27] K. Rahbar, S. Mahmoud, R. K. Al-Dadah, and N. Moazami, *Parametric analysis and optimization of a small-scale radial turbine for organic rankine cycle,* Energy **83**, 696 (2015).

[28] M. Pini, G. Persico, E. Casati, and V. Dossena, *Preliminary design of a centrifugal turbine for organic rankine cycle applications,* Journal of Engineering for Gas turbines and power **135**, 042312 (2013).

[29] J. D. Anderson, *Modern compressible flow: with historical perspective*, Vol. 12 (McGraw-Hill New York, 1990).

[30] M. Zucrow and J. Hoffman, *Gas dynamics, vols. i and ii,* Wi ley & Sons , 297 (1976).

[31] L. J. Goldman and V. J. Scullin, *Analytical investigation of supersonic turbomachinery blading. 1-computer program for blading design,* (1968).

[32] L. J. Goldman, *Analytical investigation of supersonic turbomachinery blading. 2-analysis of impulse turbine-blade sections,* (1968).

[33] A. H. Shapiro, *The Dynamics and Thermodynamics of Compressible Fluid Flow in Two Volumes* (New York, Ronald Press Company, 1953).

[34] H. Peter Goossens, *Rotating reference frame: Centrifugal and coriolis forces,* (2007).

[35] *Su2: Open-source cfd code,* (2012).

[36] F. Palacios, J. Alonso, K. Duraisamy, M. Colonno, J. Hicken, A. Aranake, A. Campos, S. Copeland, T. Economon, A. Lonkar, *et al.*, *Stanford university unstructured (su 2): an open-source integrated computational environment for multi-physics simulation and design,* in *51st AIAA Aerospace Sciences Meeting including the New Horizons Forum and Aerospace Exposition* (2013) p. 287.